The Effects of Confinement in Active Matter: the Casimir Effect, Partitioning, and Hindered Diffusion

Thesis by
Camilla Maria Kjeldbjerg

In Partial Fulfillment of the Requirements for the
Degree of
Doctor of Philosophy in Chemical Engineering

CALIFORNIA INSTITUTE OF TECHNOLOGY
Pasadena, California

2022
Defended July 9th 2021

Camilla Maria Kjeldbjerg
ORCID: 0000-0003-2224-0534

ACKNOWLEDGEMENTS

First and foremost, I would like to thank my advisor, Prof. John F. Brady. His continuous support, physical and mathematical insights, and great intuition guided me through my years as a graduate student. I am grateful for the opportunity to work with and learn from him. I am most grateful for the opportunity he provided for me to present at the American Physical Society March Meeting in Boston, and for his encouragement of my independence as a researcher.

I would like to thank Prof. Zhen-Gang Wang, Prof. Mikhail Shapiro, and Prof. John Seinfeld for serving on my thesis committee. A special thanks to Professor Zhen-Gang Wang for his service as my committee chair, his great support of me as a researcher, and enthusiasm towards my research. Zhen-Gang is one of the best teachers I have encountered in my academic career, and his lectures in Chemical Thermodynamics, Statistical Mechanics, and Polymer Physics are extremely clear. I was a teaching assistant for Chemical Thermodynamics twice, and sincerely enjoyed sitting in on the lectures again. Furthermore, I appreciate the trust and opportunity he gave me by letting me teach a few of the classes while he was traveling. I want to thank Professor John Seinfeld and Professor Mikhail Shapiro for their service on the committee, and for helping me consider the experimental context of my work.

The Chemical Engineering staff have made my time at Caltech profoundly easier. Thanks go to Allison Kinard, Kathy Bubash, Sohee Lee, Martha Hepworth, and Suresh Guptha. A special thanks to Allison Kinard for always being kind, welcoming, and helpful. I truly enjoyed coming by your office to chat, and hosting prospective student visit weekends with you. Thank you to Suresh Guptha for helping me with numerous computer issues throughout my time as a graduate student.

I would like to thank past and present Brady group members and visitors for a great community, sharing their knowledge, and our research discussions: Sho Takatori, Kevin Marshall, Eric Burkholder, Wen Yan, Mu Wang, Charlie Slominski, Austin Dulaney, Zhiwei Peng, Hyeongjoo Row, Stewart Mallory, Edmond Zhou, Alec Glisman, Tyler Ross, Mario Sandoval, and Karol Makuch. Thank you to the members of the Wang group for contributing to the great first floor community in Spalding and to research discussions: Ahmad Omar, Chris Balzer, and Kevin Shen.

A special note of thanks to my undergrad research advisor Professor Anne Ladegaard Skov at DTU for her mentoring, teaching me the fundamentals of doing research,

and for the opportunity to present my undergraduate thesis at a conference. The experience elevated my interest for pursuing research, and helped me learn how to succeed as a researcher. Additionally, I would like to thank Professor Klaus Bragaard Møller at DTU for encouraging me to pursue a term as an exchange student at Caltech during my undergrad.

Lastly, I would like to thank my friends and family for their continuous support and encouragement to pursue my own ideas and interests.

ABSTRACT

Active matter describes a class of materials for which constituent "particles" convert chemical energy into mechanical motion leading to self-propulsion (swimming). The origins of this swimming motion for both biological and synthetic constituents is a thriving area of research. However, here we focus on the physical properties and mechanics of the active matter systems. We model active particles using the active Brownian particle (ABP) model that is the simplest model that captures the essential physics, where a particle translates with a swim speed U_0 in a direction $\boldsymbol{q}$ for a characteristic reorientation time τ_R; the average length they move between each reorientation is called the run, or persistence, length $\ell = U_0\tau_R$. Owing to this persistent swimming, the ABPs distribute non-homogenously near surfaces, accumulating at no-flux boundaries leading to a concentration boundary layer near solid surfaces. Active particles often have an effective size—their run length—which can be much larger than their geometric size such that they experience confinement in geometries whose size is on the order of the run length. Active systems are inherently far from equilibrium, and we cannot appeal to properties of equilibrium thermodynamic such as the chemical potential to predict the partitioning. Fortunately, active particles are still subject to the laws of mechanics, and in this work, we present a simple macroscopic balance that allows one to predict behavior without detailed calculations. We predict the attractive force between two parallel plates in a reservoir (also called the Casimir effect) and find that the average concentration between the plates equals that in the bulk reservoir independent of the degree of confinement (ratio of run length to the spacing between the plates). We then examine the confinement effects in a channel geometry, where the behavior is fundamentally different, and the average concentration grows linearly with the degree of confinement. The understanding of these fundamental geometries motivated us to look into more complex geometries such as porous media. Based on dimensional analysis and our predictive model, we explain the transient behavior and steady-state partitioning of active particles between a fluid reservoir and a porous medium. Lastly, we discuss the hindered diffusion in periodic porous media and how the diffusion depends not only on the porosity of the medium but also on the degree of confinement. We believe that utilizing the insights in effects of confinement for these fundamental geometries and the porous media will be valuable in designing optimal structures for enhancing or isolating active particles.

PUBLISHED CONTENT AND CONTRIBUTIONS

[1] C. M. Kjeldbjerg and J. F. Brady, "Partitioning of active particles into porous media", Soft Matter **18**, DOI: 10.1039/d1sm01752g, 2757–2766 (2022),

C.M.K. participated in the conception of the project, performed the calculations, analyzed the data, performed the simulations, and participated in the writing of the manuscript.

[2] C. M. Kjeldbjerg and J. F. Brady, "Theory for the casimir effect and the partitioning of active matter", Soft Matter **17**, DOI: 10.1039/d0sm01797c, 523–530 (2021),

C.M.K. participated in the conception of the project, performed the calculations, analyzed the data, performed the simulations, and participated in the writing of the manuscript.

TABLE OF CONTENTS

LIST OF ILLUSTRATIONS

Chapter 1

INTRODUCTION

This thesis consists of independent chapters that are presented in a form suitable for publication, with Chapter 2 already published. This introductory chapter provides an overview of the fundamental features of active matter systems, implications of confinement, questions which motivated this work, and relevant applications. In Chapter 2, we lay out the groundwork for understanding the Casimir effect and partitioning in active matter for fundamental geometries through a mechanical balance perspective. In Chapter 3, we expand this theoretical framework to a more complex porous media system to predict the partitioning of active particles within this type of confinement. Lastly, in Chapter 4, we explore the effects of porous media on the hindered diffusion of active particles.

This introductory chapter includes content from our previously published article:

[1] C. M. Kjeldbjerg and J. F. Brady, "Theory for the casimir effect and the partitioning of active matter", Soft Matter **17**, DOI: 10.1039/d0sm01797c, 523–530 (2021),

1.1 Active Matter

The concept of active matter can describe many natural systems: the flocking of birds, humans walking in a crowded area, the movement of bacteria, Janus particles in suspension, etc. [1–3]. In this thesis, we focus on active matter at the micron or colloidal scale. Active matter systems consist of self-propulsive particles which convert (often) chemical energy into mechanical motion; this leads to random self-propulsion [4]. These movements generate internal stresses and can thereby drive systems far from thermodynamic equilibrium [5]. Active matter systems can have very interesting behaviors such as moving collectively under an external field [6, 7], spontaneous and controlled self-assembly [8–15], spontaneous phase separation into dilute and dense phases [16–25], accumulation at surfaces [26–28], and converting chemical energy into mechanical work through the rotation of micro-gears [29, 30].

1.2 Dynamics of active matter

Active matter systems are inherently non-equilibrium, and one cannot rely on thermodynamics for a description. However, active matter still obeys the fundamental laws of physics, and we therefore turn to the conservation of mass and momentum to describe the systems. The motion of active particles is significantly different from those of passive Brownian particles. Passive particle motion arises from thermal energy, whereas active particle motion comes from the combination of thermal energy and their inherent activity.

The simplest model that captures the essential physics is the active Brownian particle (ABP) model, where each particle translates with a swim speed U_0 in a direction $\boldsymbol{q}$ for a characteristic reorientation time τ_R; the average length they move between each reorientation is called the run, or persistence, length $\ell = U_0\tau_R$ [31]. This model is illustrated in Fig. 1.1. Active particles will persistently swim in one direction until they reorient and swim in the new direction. This swimming can be described as a stochastic process with a rotational diffusivity, $D_R = \tau_R^{-1}$; this rotation does not need to be thermal in nature. For example, it could originate from a bacteria bundling and unbundling their flagella [32]. At times shorter than the reorientation time, the motion of the particles will be ballistic in nature [33]. For times longer than the reorientation time, the motion will form a random walk and be diffusive with a swim diffusivity, $D^{swim} = U_0^2\tau_R/(d(d-1))$, where d is the number of rotational dimensions [4, 6, 22, 26]. Similarly to the Stokes-Einstein-Sutherland relationship for Brownian particles, we define an active energy scale such that $D^{swim} = \zeta k_s T_s$,

where ζ is the Stokes drag. The ratio of this active energy to the thermal energy becomes a measure of the activity of the system, $k_s T_s / k_B T$ [34].

Langevin equations

A system of active Brownian particles can be described by the overdamped Langevin equations. ABPs are in the Stokes regime where the Reynolds number is low. Therefore, viscous forces dominate in the equations of motion, and inertia can be neglected. This leads to motion being both force-free and torque-free; $\sum \boldsymbol{F} = \mathbf{0}$ and $\sum \boldsymbol{L} = \mathbf{0}$. The drag force, $F = \zeta \boldsymbol{U}$, is balanced by the other forces acting on the particle such that

$$\mathbf{0} = -\boldsymbol{F}^{drag} + \boldsymbol{F}_\alpha^{Swim} + \boldsymbol{F}_\alpha^{B} + \boldsymbol{F}_\alpha^{W}, \tag{1.1}$$

$$\mathbf{0} = -\boldsymbol{L}^{drag} + \boldsymbol{L}_\alpha^{R}, \tag{1.2}$$

where $\boldsymbol{F}_\alpha^{Swim}$ is the swim force defined as $\boldsymbol{F}_\alpha^{Swim} \equiv \zeta U_0 \boldsymbol{q}_\alpha$. $\boldsymbol{F}_\alpha^{B}$ is the random Brownian force with the properties $\overline{\boldsymbol{F}_\alpha^{B}} = \mathbf{0}$ and the $\overline{\boldsymbol{F}_\alpha^{B}(0)\boldsymbol{F}_\alpha^{B}(t)} = 2k_B T \zeta \delta(t) \boldsymbol{I}$, where $\boldsymbol{I}$ is the identity tensor and $\delta(t)$ is the delta-function. $\boldsymbol{L}^R$ is the random reorientation torque, where $\overline{\boldsymbol{L}^R} = \mathbf{0}$ and $\overline{\boldsymbol{L}^R(0)\boldsymbol{L}^R(t)} = 2\zeta_R^2 \delta(t) \boldsymbol{I} / \tau_R$. Note that it is

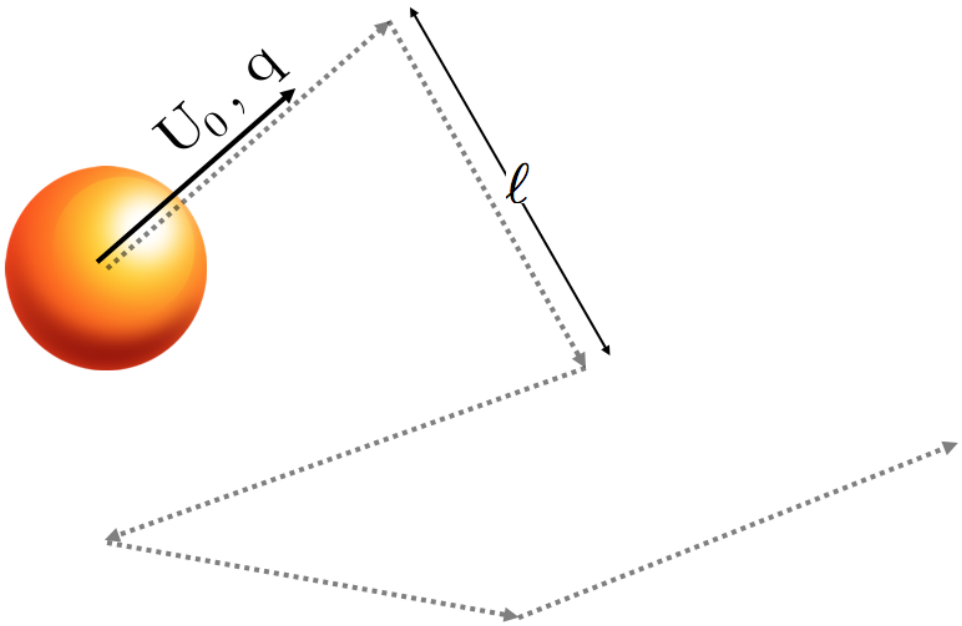

Figure 1.1: Example of an ABP's random movement with swim speed $\mathbf{U}_0$ in an orientation $\mathbf{q}$. The length the ABP travels between reorientations is the run length ℓ, and the reorientation time is τ_R $(= \ell / U_0)$.

not necessary to assume that the translational and rotational diffusivities are both thermal, i.e., D_R need not be proportional to k_BT. The Langevin equations provide a per particle perspective balance, however, we can also describe the active Brownian particles from a probability perspective.

Smoluchowski equation

For a dilute suspension of APBs, the particle distribution is governed by the Smoluchowski equation for the probability density $P(\boldsymbol{x}, \boldsymbol{q}, t)$ for finding a particle at position $\boldsymbol{x}$ with orientation $\boldsymbol{q}$ at time t [35–37]:

$$\frac{\partial P(\boldsymbol{x}, \boldsymbol{q}, t)}{\partial t} + \nabla \cdot \boldsymbol{j}^T + \nabla_R \cdot \boldsymbol{j}^R = 0, \tag{1.3}$$

where the translational and rotational fluxes are $\boldsymbol{j}^T = U_0 \boldsymbol{q} P - D_T \nabla P$ and $\boldsymbol{j}^R = -D_R \nabla_R P$, respectively. Here, D_T and D_R are the translational and rotational diffusivities; the reorientation time $\tau_R = 1/D_R$. The orientational gradient operator is $\nabla_R = \boldsymbol{q} \times \nabla \boldsymbol{q}$. While the system's behavior is fully determined from the Smoluchowski equation (1.3), finding its solution is a daunting task. To make progress and capture the essential features of the distribution of ABPs, one can expand the Smoluchowski equation in the first few orientational moments: the zeroeth moment is the concentration $n(\boldsymbol{x}, t) = \int P(\boldsymbol{x}, \boldsymbol{q}, t) d\boldsymbol{q}$, the first moment is the polar order $\boldsymbol{m}(\boldsymbol{x}, t) = \int \boldsymbol{q} P(\boldsymbol{x}, \boldsymbol{q}, t) d\boldsymbol{q}$, etc. For two dimensions, the orientational moments satisfy a hierarchy of equations [35]:

$$\frac{\partial n}{\partial t} + \nabla \cdot \boldsymbol{j}_n = 0, \tag{1.4}$$

$$\frac{\partial \boldsymbol{m}}{\partial t} + \nabla \cdot \boldsymbol{j}_m + D_R \boldsymbol{m} = 0, \tag{1.5}$$

where the fluxes are

$$\boldsymbol{j}_n = U_0 \boldsymbol{m} - D_T \nabla n, \tag{1.6}$$

$$\boldsymbol{j}_m = U_0 \boldsymbol{Q} + \frac{1}{2} U_0 n \boldsymbol{I} - D_T \nabla m. \tag{1.7}$$

Here, n is the number density, $\boldsymbol{m}$ is the polar order, and $\boldsymbol{Q}$ is the nematic order, $\boldsymbol{Q}(\boldsymbol{x}, t) = \int (\boldsymbol{q}\boldsymbol{q} - \frac{1}{2}\boldsymbol{I}) P(\boldsymbol{x}, \boldsymbol{q}, t) d\boldsymbol{q}$, with $\boldsymbol{I}$ the isotropic tensor. The system is often closed by assuming that the nematic order is isotropic $\boldsymbol{Q} = \boldsymbol{0}$, and even then finding the solution can be daunting for systems of two or more dimensions.

1.3 Boundary accumulation of active particles

Owing to active particles' persistent swimming, ABPs distribute non-homogenously near surfaces and will accumulate at no-flux boundaries leading to a concentration

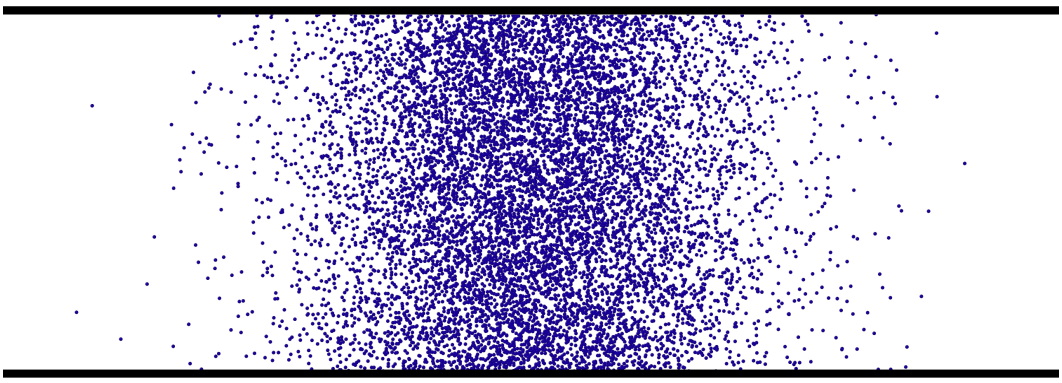

Figure 1.2: Passive particles released from a line source in the center between two parallel walls. The particles diffuse out due to thermal diffusion and distribute with a homogeneous concentration between the two walls.

boundary layer near solid surfaces [4, 26, 27]. If the active particle run length is large compared to its size, the effective size of a particle can be much larger than its geometric size. Therefore, ABPs often experience confinement in geometries on the order of their run length [24, 26, 38, 39]. This exciting phenomenon is the motivation for this thesis. We focus on understanding how confinement influences the distribution of active matter and how we can predict it using a mechanical balance perspective. We only consider particles on the colloidal scale, where inertia is negligible. Therefore, we are in the Stokes regime, and the motion of particles is force– and torque-free [40, 41]. The mechanical balance, therefore, consists of a momentum balance and utilization of the pressures of the system. The pressures in the system will be the osmotic pressure from thermal motion and the swim pressure.

To illustrate the stark difference between the passive and the active Brownian particles, we consider passive particles being released from a line source between two parallel walls. The particles will diffuse outwards from the line source, and their concentration will be homogeneous between the two walls. Fig. 1.2 illustrates this, where we observe that the passive Brownian particles are not accumulating at the walls. The pressure on a single wall, Π^W, will be given by the osmotic pressure such that

$$\Pi^W = n^W k_B T = n^0 k_B T, \tag{1.8}$$

where n^w is the concentration on the wall, n^0 is the center concentration, and $k_B T$ is the thermal energy. Thus, when particles are passive, there is no wall accumulation, and the concentration at the wall is equal to the one in the bulk, $n^W = n^0$. However,

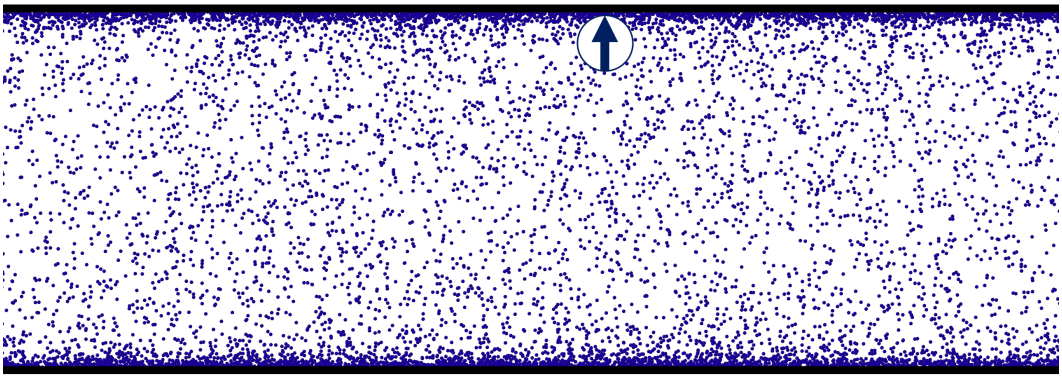

Figure 1.3: Active particles released from a line source in the center between two parallel walls after 5 τ_R. The active particles diffuse out due to thermal diffusion and swimming. They accumulate at the two boundaries, additionally most of the particles at the wall are oriented into the wall as the arrow demonstrates. Here, the activity $k_sT_s/k_BT = 50$, $\ell/H = 1$, and $L/H = 3$.

for active particles, we observe an inherently different behavior. The particles still diffuse out, but we also notice the accumulation at boundaries. This is illustrated for active Brownian particles diffusing from a line source between two walls in Fig. 1.3, where $k_sT_s/k_BT = 50$, $\ell/H = 1$, and $L/H = 3$. The pressure on the wall is the osmotic pressure, $\Pi^{osm} = n^W k_BT$, but the wall concentration is no longer equal to the bulk concentration.

Analogous to the osmotic pressure, $\Pi^{osm} = nk_BT$, the swim pressure can be written as $\Pi^{swim} = nk_sT_s$, where $k_sT_s = \zeta U_0^2\tau_R/2$ in two dimensions [22, 42]. The pressure on a single wall in a bath of active particles is

$$\Pi^W = n^W k_BT = n^\infty(k_BT + k_sT_s), \tag{1.9}$$

where n^W is the number density at the wall and n^∞ is the number density in the bulk. From the Smoluchowski equations, Yan and Brady showed that for ABPs close to a wall, the concentration decays exponentially from the wall out into the bulk, [26]:

$$n(z) = n^\infty\left(1 + \frac{1}{2}(\ell/\delta)^2\exp\left(-z\sqrt{1 + \frac{1}{2}(\ell/\delta)^2}/\delta\right)\right), \tag{1.10}$$

where z is the distance from the wall, and $\delta = \sqrt{D_T/D_R}$ is the diffusive step size with the thermal diffusivity, D_T. Fig. 1.4 shows the accumulation boundary layer near a single wall in a bath of active particles. A particle colliding with the wall will

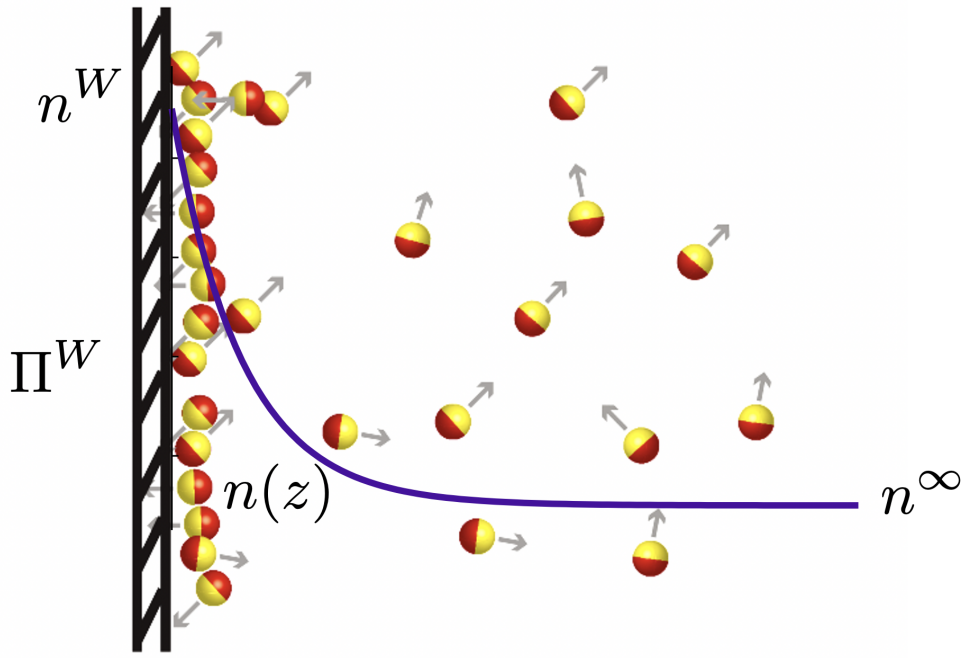

Figure 1.4: The accumulation boundary layer of ABPs near a single wall in an active bath with wall concentration $\Pi^W = n^\infty(k_s T_s + k_B T)$, where n^∞ is the bulk concentration of ABPs and the analytical form of $n(z)$ is given in (1.10).
This illustration is adapted from [4].

keep pushing in its orientational direction until it reorients and moves away from the boundary layer. Therefore, almost all the particles within the boundary layer are oriented towards the wall, and this leads to a polar order near the wall. In the bulk of the bath, there is no polar order as particles are randomly oriented.

The accumulation of particles at a single wall is one of the most fundamental and straightforward confinement problems in active matter, and the exact solution is known analytically. Here, we define confinement as any surface or boundary that abrupt the particle movement, leading to its run length being cut off. Similar to the single wall, other pseudo-one dimensional problems' analytical solutions are known, such as between two parallel walls, and in– and outside a sphere [26]. On the other hand, solutions to multi-dimensional problems can be challenging to obtain due to the nature of the Smoluchowski equations; the orientation of the particles contributes to one or two dimensions in addition to the spatial dimensions. The focus of this thesis is to understand some of these fundamental two– and three-dimensional problems. In the next section, we describe some interesting

experimental observations of active particles under confinement.

1.4 Effects of confinement

Active particles will experience confinement when their run, or persistence, length is being obstructed, and they are no longer able to move as they would in free space [4, 26]. Particle accumulation at a single surface is an interesting phenomenon on its own and well understood from the perspective of swim pressure and persistent motion. We focus on confinement in multiple dimensions that give rise to fascinating phenomena that are vastly different from the behavior of passive Brownian particles in the same geometries [26, 43–45]. The recent interest in active matter has led to an increasing number of experiments with active particles, such as bacteria, under confinement [46–58].

Active particles interacting with asymmetrical objects can lead to spontaneous directed motion and partitioning [59–63]. Galajda et al. [55] showed that placing *E. coli* in a square container divided by Chevron-shaped barriers (shown in Fig. 1.5) would concentrate the bacteria on one side of the container. This behavior is profoundly different from purely *passive* Brownian particles, which would homogeneously fill a volume independent of the geometric shape. The partitioning of *E. coli* is a direct result of the bacteria having a persistent motion with a run length much larger than both their size and the size of the funnel-shaped openings. Di Giacomo et al. [58] have utilized this persistent motion to sequester motile bacteria by deploying three-dimensional micro-traps. Experimental studies of *Chlamydomonas Reinhardtii* show that the diffusion of bacteria is obstructed by arrays of pillars

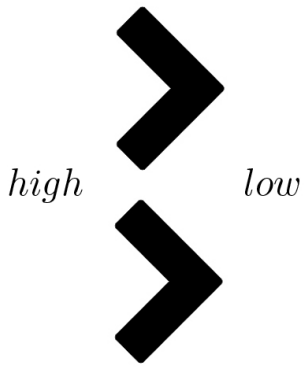

Figure 1.5: Chevron-shaped barriers adapted from [55] where *high* and *low* denotes the concentration.

and becomes lower than it would be in the free space [57]. Additionally, in highly crowded environments, *E. coli* has been observed to display an interesting hopping-trapping behavior; *E. coli* is trapped in pockets of space between densely packed obstacles, and then hops through highly confined channels into other pockets of space [64, 65].

One application of active matter in confined environments is in agricultural practices. Probiotic treatment, such as using *Rhizosphere Pseudomonas*, improves crop health by colonizing plant roots, which provides increased protection against pathogen attacks, improved growth potential, and increased tolerance towards stress from water, salts, and heavy metals in the soil. All of which lead to improved yield and quality of crops [66–71]. For optimal production, the bacteria need to be efficiently transported through a complex, confined soil environment to reach the plant roots.

1.5 Contributions

In this thesis, we aim to provide an understanding of how confinement influences the behavior of active matter. The main focus is on how confinement affects pressure, concentration distributions, and diffusion in fundamental two– and three-dimensional systems. Active systems are inherently far from equilibrium, and we cannot appeal to equilibrium thermodynamic properties such as the chemical potential to predict the partitioning. Fortunately, active particles are still subject to the laws of mechanics, and we formulate a simple macroscopic balance that allows one to predict behavior without detailed calculations. We compare our predictive model to solutions of the governing equations for active Brownian particles. The results of our analytical prediction are in excellent agreement with simulation results for simple systems, such as parallel plates in an active bath and a channel in a wall. Therefore, we extend the model to predict the partitioning in a more complex system consisting of porous media connected to a reservoir. Lastly, we discuss how porous media leads to a hindered diffusion of active particles.

The following chapters are organized as follows:

In Chapter 2, we introduce the foundation for the macroscopic momentum balance that allows us to predict the behavior of active particles under confinement. First, we consider the attraction between two parallel plates (also called the Casimir effect [72]) and show that the average concentration between the plates equals that in the bulk reservoir independent of the degree of confinement. This leads to a simple analytical expression for the attractive force. We then study the partitioning

in a channel geometry and show that the behavior is fundamentally different, with the average concentration growing linearly with the ratio of the run length to the channel spacing. Finally, we extend our analysis to a periodic array of plates in contact with an infinite reservoir. We show that as the thickness of the plates increases, the partitioning transitions from the parallel plate result to those of the channel.

Chapter 3 covers the transient behavior and steady-state partitioning of active particles between a fluid reservoir and a porous medium (i.e., arrays of spherical obstacles). Based on dimensional analysis, we determine that the partitioning is set by the ratio of the run length to the obstacle size, the active step size relative to the diffusive step, and the area fraction of obstacles in the porous medium. Additionally, we explain fascinating initial oscillations in the concentration in the bulk of the porous medium in two dimensions. Then, based on the simple macroscopic balance introduced in Chapter 2, we derive a theory for the long-time partitioning between the porous medium and reservoir in two and three dimensions utilizing the concentration distribution outside a single obstacle. This prediction provides a means to understanding particle behavior for different activity levels and at different porosity levels.

In Chapter 4, we explore the motion of active particles in a periodic porous medium. The hindered diffusion of Passive Brownian particles in porous media only depends on the area fraction of obstacles in the media *only*. However, this is not always the case for active particles whose effective diffusivity is sensitive to the interplay between run length, the media's pore size and geometry. The ABPs' effective diffusivity exhibits a complex non-monotonic behavior with increasing obstacle size for a fixed porosity. Through dimensional analysis, we determine that three non-dimensional parameters govern the behavior: 1) the activity, 2) the volume (or area) fraction of obstacles, and 3) the degree of confinement (ratio of run length to obstacle size). Additionally, we develop an analytical theory for dilute porous media that offers scaling predictions for dense porous media.

References

[1] E. Lauga and T. R. Powers, "The hydrodynamics of swimming microorganisms", Reports on Progress in Physics **72**, 096601 (2009).

[2] S. Granick, S. Jiang, and Q. Chen, "Janus particles", Physics Today **62**, 68–69 (2009).

[3] F. Wurm and A. F. M. Kilbinger, "Polymeric Janus particles", Angewandte Chemie-international Edition **48**, 8412–8421 (2009).

[4] S. C. Takatori and J. F. Brady, "Forces, stresses and the (thermo?) dynamics of active matter", Current Opinion in Colloid and Interface Science **21**, 24–33 (2016).

[5] S. Ramaswamy, "The mechanics and statistics of active matter", Annual Review of Condensed Matter Physics **1**, 323–345 (2010).

[6] S. C. Takatori and J. F. Brady, "Swim stress, motion, and deformation of active matter: effect of an external field", Soft Matter **10**, 9433–9445 (2014).

[7] G. Gompper, C. Bechinger, S. Herminghaus, R. Isele-Holder, U. B. Kaupp, H. Loewen, H. Stark, and R. G. Winkler, "Microswimmers – from single particle motion to collective behavior", European Physical Journal-special Topics **225**, 2061–2064 (2016).

[8] S. Ebbens, R. A. Jones, A. J. Ryan, R. Golestanian, and J. R. Howse, "Self-assembled autonomous runners and tumblers", Physical Review E - Statistical, Nonlinear, and Soft Matter Physics **82**, 6–9 (2010).

[9] V. Prymidis, H. Sielcken, and L. Filion, "Self-assembly of active attractive spheres", Soft Matter **11**, 4158–4166 (2015).

[10] S. A. Mallory and A. Cacciuto, "Activity-assisted self-assembly of colloidal particles", Physical Review E **94**, 10.1103/PhysRevE.94.022607 (2016).

[11] G. S. Redner, C. G. Wagner, A. Baskaran, and M. F. Hagan, "Classical nucleation theory description of active colloid assembly", Physical Review Letters **117**, 1–7 (2016).

[12] S. A. Mallory, C. Valeriani, and A. Cacciuto, "An active approach to colloidal self-assembly", Annual Review of Physical Chemistry **69**, 59–79 (2018).

[13] S. A. Mallory and A. Cacciuto, "Activity-enhanced self-assembly of a colloidal Kagome lattice", Journal of the American Chemical Society, 10.1021/jacs.8b12165 (2019).

[14] T. D. Ross, H. J. Lee, Z. Qu, R. A. Banks, R. Phillips, and M. Thomson, "Controlling organization and forces in active matter through optically defined boundaries", Nature **572**, 224–229 (2019).

[15] A. K. Omar, Y. Wu, Z. G. Wang, and J. F. Brady, "Swimming to stability: Structural and dynamical control via active doping", ACS Nano **13**, 560–572 (2019).

[16] A. Wysocki, R. G. Winkler, and G. Gompper, "Cooperative motion of active brownian spheres in three-dimensional dense suspensions", EPL **105**, 48004 (2014).

[17] J. Palacci, S. Sacanna, A. P. Steinberg, D. J. Pine, and P. M. Chaikin, "Living crystals of light-activated colloidal surfers", Science **339**, 936–940 (2013).

[18] J. Stenhammar, D. Marenduzzo, R. J. Allen, and M. E. Cates, "Phase behavior of active Brownian particles: The role of dimensionality", Soft Matter **10**, 1489–1499 (2014).

[19] I. Buttinoni, J. Bialke, F. Kuemmel, H. Loewen, C. Bechinger, and T. Speck, "Dynamical clustering and phase separation in suspensions of self-propelled colloidal particles", Physical Review Letters **110**, 238301 (2013).

[20] M. E. Cates, D. Marenduzzo, I. Pagonabarraga, and J. Tailleur, "Arrested phase separation in reproducing bacteria creates a generic route to pattern formation", Proceedings of the National Academy of Sciences of the United States of America **107**, 11715–11720 (2010).

[21] Y. Fily and C. Marchetti, "Athermal phase separation of self-propelled particles with no alignment", Physical Review Letters **108**, 235702 (2012).

[22] S. C. Takatori, W. Yan, and J. F. Brady, "Swim pressure: Stress generation in active matter", Physical Review Letters **113**, 028103 (2014).

[23] S. C. Takatori and J. F. Brady, "A theory for the phase behavior of mixtures of active particles", Soft Matter **11**, 7920–7931 (2015).

[24] X. Yang, L. Manning, and C. Marchetti, "Aggregation and segregation of confined active particles", Soft Matter **10**, 6477–6484 (2014).

[25] J. Stenhammar, A. Tiribocchi, R. J. Allen, D. Marenduzzo, and M. E. Cates, "Continuum theory of phase separation kinetics for active Brownian particles", Physical Review Letters **111**, 145702 (2013).

[26] W. Yan and J. F. Brady, "The force on a boundary in active matter", Journal of Fluid Mechanics **785**, R1 (2015).

[27] W. Yan and J. F. Brady, "The curved kinetic boundary layer of active matter", Soft Matter **14**, 279–290 (2018).

[28] A. K. Omar, Z. G. Wang, and J. F. Brady, "Microscopic origins of the swim pressure and the anomalous surface tension of active matter", Physical Review E **101** (2020).

[29] C. Maggi, J. Simmchen, F. Saglimbeni, J. Katuri, M. Dipalo, F. De Angelis, S. Sanchez, and R. Di Leonardo, "Self-assembly of micromachining systems powered by Janus micromotors", Small **12**, 446–451 (2016).

[30] C. Bechinger, R. Di Leonardo, H. Löwen, C. Reichhardt, G. Volpe, and G. Volpe, "Active particles in complex and crowded environments", Reviews of Modern Physics **88**, 045006 (2016).

[31] D. A. Beard and T. Schlick, "Unbiased rotational moves for rigid-body dynamics", Biophysical Journal **85**, 2973–2976 (2003).

[32] H. C. Berg and R. A. Anderson, "Bacteria swim by rotating their flagellar filaments", Nature **245**, 380–382 (1973).

[33] A. R. Dulaney and J. F. Brady, "Waves in active matter: the transition from ballistic to diffusive behavior", Physical Review E **101**, 052609 (2020).

[34] S. C. Takatori and J. F. Brady, "Towards a thermodynamics of active matter", Physical Review E – Statistical, Nonlinear, and Soft Matter Physics **91**, 1–7 (2015).

[35] W. Yan and J. F. Brady, "The swim force as a body force", Soft Matter **11**, 6235–6244 (2015).

[36] D. Saintillan and M. J. Shelley, "Active suspensions and their nonlinear models", Comptes Rendus Physique **14**, 497–517 (2013).

[37] J. F. Brady, "Particle motion driven by solute gradients with application to autonomous motion: Continuum and colloidal perspectives", Journal of Fluid Mechanics **667**, 216–259 (2011).

[38] W. M. Lai, D. Rubin, and E. Krempl, *Introduction to Continuum Mechanics, Revised Edition* (Pergamon, 1978), p. 324.

[39] B. Ezhilan, R. Alonso-Matilla, and D. Saintillan, "On the distribution and swim pressure of run-and-tumble particles in confinement", Journal of Fluid Mechanics **781**, R4 (2015).

[40] M. J. Lighthill, "On the squirming motion of nearly spherical deformable bodies through liquids at very small reynolds numbers", Communications on Pure and Applied Mathematics **5**, 109–118 (1952).

[41] G. Taylor, "Analysis of the swimming of microscopic organisms", Nelineinaya Dinamika **209**, 371–387 (1951).

[42] J. F. Brady, "Brownian-motion, hydrodynamics, and the osmotic-pressure", Journal of Chemical Physics **98**, 3335–3341 (1993).

[43] J. Elgeti, R. G. Winkler, and G. Gompper, "Physics of microswimmers - Single particle motion and collective behavior: A review", Reports on Progress in Physics **78** (2015).

[44] M. Paoluzzi, R. Di Leonardo, and L. Angelani, "Self-sustained density oscillations of swimming bacteria confined in microchambers", Physical Review Letters **115**, 1–5 (2015).

[45] C. M. Kjeldbjerg and J. F. Brady, "Theory for the casimir effect and the partitioning of active matter", Soft Matter **17**, DOI: 10.1039/d0sm01797c, 523–530 (2021),

[46] A. Sokolov, M. M. Apodaca, B. A. Grzybowski, and I. S. Aranson, "Swimming bacteria power microscopic gears", Proceedings of the National Academy of Sciences of the United States of America **107**, 969–974 (2010).

[47] A. Bricard, J. B. Caussin, N. Desreumaux, O. Dauchot, and D. Bartolo, "Emergence of macroscopic directed motion in populations of motile colloids", Nature **503**, 95–98 (2013).

[48] H. Wioland, F. G. Woodhouse, J. Dunkel, J. O. Kessler, and R. E. Goldstein, "Confinement stabilizes a bacterial suspension into a spiral vortex", Physical Review Letters **110**, 1–5 (2013).

[49] Y. Fily, A. Baskaran, and M. F. Hagan, "Dynamics of self-propelled particles under strong confinement", Soft Matter **10**, 5609–5617 (2014).

[50] E. Lushi, H. Wioland, and R. E. Goldstein, "Fluid flows created by swimming bacteria drive self-organization in confined suspensions", Proceedings of the National Academy of Sciences of the United States of America **111**, 9733–9738 (2014).

[51] H. Wioland, F. G. Woodhouse, J. Dunkel, and R. E. Goldstein, "Ferromagnetic and antiferromagnetic order in bacterial vortex lattices", Nature Physics **12**, 341–345 (2016).

[52] "Emergent vortices in populations of colloidal rollers", Nature Communications **6**, 1–8 (2015).

[53] I. D. Vladescu, E. J. Marsden, J. Schwarz-Linek, V. A. Martinez, J. Arlt, A. N. Morozov, D. Marenduzzo, M. E. Cates, and W. C. Poon, "Filling an emulsion drop with motile bacteria", Physical Review Letters **113**, 1–5 (2014).

[54] N. Kumar, H. Soni, S. Ramaswamy, and A. K. Sood, "Flocking at a distance in active granular matter", Nature Communications **5**, 10.1038/ncomms5688 (2014).

[55] P. Galajda, J. Keymer, P. Chaikin, and R. Austin, "A wall of funnels concentrates swimming bacteria", Journal of Bacteriology **189**, 8704–8707 (2007).

[56] S. C. Takatori, R. De Dier, J. Vermant, and J. F. Brady, "Acoustic trapping of active matter", Nature Communications **7**, 10694 (2016).

[57] M. Brun-Cosme-Bruny, E. Bertin, B. Coasne, P. Peyla, and S. Rafaï, "Effective diffusivity of microswimmers in a crowded environment", Journal of Chemical Physics **150**, 104901 (2019).

[58] R. Di Giacomo, S. Krödel, B. Maresca, P. Benzoni, R. Rusconi, R. Stocker, and C. Daraio, "Deployable micro-traps to sequester motile bacteria", Scientific Reports **7**, 1–8 (2017).

[59] C. Reichhardt and C. J. Reichhardt, "Active matter ratchets with an external drift", Physical Review E – Statistical, Nonlinear, and Soft Matter Physics **88**, 1–10 (2013).

[60] B. Lau, O. Kedem, J. Schwabacher, D. Kwasnieski, and E. A. Weiss, "An introduction to ratchets in chemistry and biology", Materials Horizons **4**, 310–318 (2017).

[61] C. J. Reichhardt and C. Reichhardt, "Ratchet effects in active matter systems", Annual Review of Condensed Matter Physics **8**, 51–75 (2017).

[62] J. Katuri, D. Caballero, R. Voituriez, J. Samitier, and S. Sanchez, "Directed flow of micromotors through alignment interactions with micropatterned ratchets", ACS Nano **12**, 7282–7291 (2018).

[63] W. R. DiLuzio, L. Turner, M. Mayer, P. Garstecki, D. B. Weibel, H. C. Berg, and G. M. Whitesides, "Escherichia coli swim on the right-hand side", Nature **435**, 1271–1274 (2005).

[64] Sujit S. Datta, "Confinement and activity regulate bacterial motion in porous media", Soft Matter **64**, 6545–6563 (2019).

[65] L. J. Perez, T. Bhattacharjee, S. S. Datta, R. Parashar, and N. L. Sund, "Impact of confined geometries on hopping and trapping of motile bacteria in porous media", Physical Review E **103**, 1–9 (2021).

[66] R. L. Berendsen, C. M. Pieterse, and P. A. Bakker, "The rhizosphere microbiome and plant health", Trends in Plant Science **17**, 478–486 (2012).

[67] M. N. Schroth and J. G. Hancock, "Disease-suppressive soil and root-colonizing bacteria", Science **216** (1982).

[68] Y. C. Kim and A. J. Anderson, "Rhizosphere pseudomonads as probiotics improving plant health", Molecular Plant Pathology **19**, 2349–2359 (2018).

[69] S. Timmusk, L. Behers, J. Muthoni, A. Muraya, and A. C. Aronsson, "Perspectives and challenges of microbial application for crop improvement", Frontiers in Plant Science **8**, 1–10 (2017).

[70] I. Young, J. Crawford, N. Nunan, W. Otten, and A. Spiers, *Microbial Distribution in Soils: Physics and Scaling* (*Academic Press*, 2008), pp. 81–121.

[71] M. Vos, A. B. Wolf, S. J. Jennings, and G. A. Kowalchuk, "Micro-scale determinants of bacterial diversity in soil", FEMS Microbiology Reviews **37**, 936–954 (2013).

[72] D. Ray, C. Reichhardt, and C. J. O. Reichhardt, "Casimir effect in active matter systems", Physical Review E **90**, 013019 (2014).

Chapter 2

THEORY FOR THE CASIMIR EFFECT AND THE PARTITIONING OF ACTIVE MATTER

Active Brownian Particles (ABPs) distribute non-homogeneously near surfaces, and understanding how this depends on system properties—size, shape, activity level, etc.—is essential for predicting and exploiting the behavior of active matter systems. Active particles accumulate at no-flux surfaces owing to their persistent swimming, which depends on their intrinsic swim speed and reorientation time, and are subject to confinement effects when their run or persistence length is comparable to the characteristic size of the confining geometry. It has been observed in simulations that two parallel plates experience a "Casimir effect" and attract each other when placed in a dilute bath of ABPs. In this work, we provide a theoretical model based on the Smoluchowski equation and a macroscopic mechanical momentum balance to analytically predict this attractive force. We extend this method to describe the concentration partitioning of active particles between a confining channel and a reservoir, showing that the ratio of the concentration in the channel to that in the bulk increases as either run length increases or channel height decreases. The theoretical results agree well with Brownian dynamics simulations and finite element calculations.

This chapter includes content from our previously published article:

[1] C. M. Kjeldbjerg and J. F. Brady, "Theory for the casimir effect and the partitioning of active matter", Soft Matter **17**, DOI: 10.1039/d0sm01797c, 523–530 (2021),

2.1 Introduction

Many natural systems can be described as active matter: the flocking of birds, humans walking in crowded areas, the movement of bacteria, Janus particles in suspension, etc. [1–3]. Active matter systems consist of "particles" that convert chemical energy into mechanical energy leading to self-propulsion [4]. These movements generate internal stresses and can drive systems far from thermodynamic equilibrium [5]. Active matter systems exhibit interesting phenomena such as particle accumulation near surfaces and self-assembly due to their persistent motion. For instance, Janus particles can accumulate at the corners of a micro-gear causing it to rotate and generate mechanical work [6–8].

Active Brownian Particles (ABPs) are a model active matter system: ABPs move with a swim speed U_0 in a direction $\boldsymbol{q}$ for a characteristic reorientation time τ_R; the average length they move between reorientations is called the run, or persistence, length $\ell = U_0\tau_R$ [9]. This model is illustrated in Fig. 2.1. Some of the interesting properties of active particles are due to the fact that they often have an effective size—their run length—which can be much larger than their geometric size such that they experience confinement in geometries whose size is on the order of the run length [10–14]. Galajda et al. [15] showed that placing *E. coli* in a square container divided by Chevron-shaped barriers (shown in Fig. 2.1(b)) would concentrate the bacteria on one side of the container. This behavior is profoundly different from purely *passive* Brownian particles, which would homogeneously fill a volume independent of the geometric shape. The partitioning of *E. coli* is a direct result of the bacteria having a persistent motion with a run length much larger than both their size and the size of the funnel-shaped openings. Di Giacomo et al. [16] have utilized this persistent motion to sequester motile bacteria by deploying 3-dimensional micro-traps.

Our aim in this work is to describe how active particles partition in simple geometries such as a channel of size H when placed in contact with an infinite reservoir of ABPs as depicted in Fig. 2.5. What is the ratio of the average concentration in the channel to that in the infinite reservoir? Active systems are inherently far from equilibrium, and we cannot appeal to equilibrium thermodynamic properties such as the chemical potential to predict the partitioning. Fortunately, active particles are still subject to the laws of mechanics, and we show that a simple macroscopic balance allows one to predict behavior without detailed calculations.

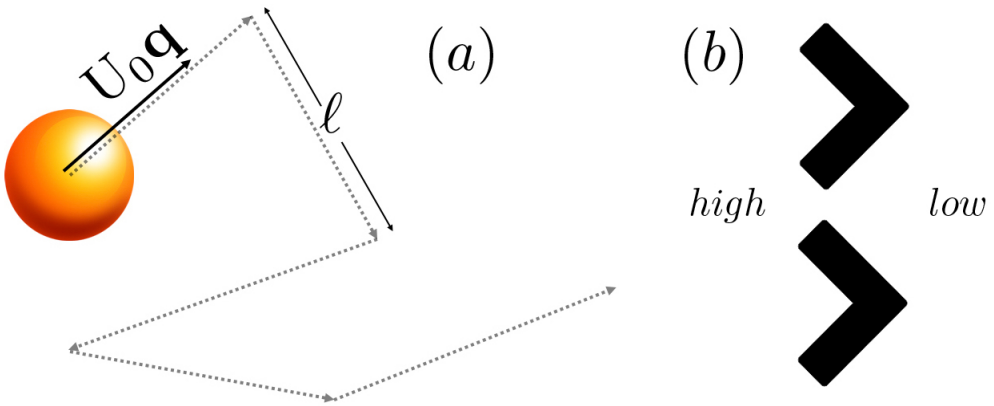

Figure 2.1: Example of (a) an ABP's random movement with swim speed U_0 in a direction $\boldsymbol{q}$, reorientation time τ_R, and run length $\ell = U_0\tau_R$. (b) Chevron-shaped barriers (from [15]).

To illustrate our approach, we first consider the attraction between two parallel plates (also called the Casimir effect [17]) and show that the average concentration between the plates equals that in the bulk reservoir independent of the degree of confinement. This leads to a simple analytical expression for the attractive force. We then study the partitioning in the previously mentioned channel geometry of Fig. 2.5, and show that the behavior is fundamentally different, with the average concentration growing linearly with the ratio of the run length to the channel spacing. The analysis is then extended to a periodic array of plates in contact with an infinite reservoir where we show how the parallel plate results transition to those of the channel when the thickness of the plates exceeds 6 times the run length.

2.2 Attraction between parallel plates: The Casimir effect

One of the simplest examples of confinement is two parallel plates separated by a gap distance H immersed in an infinite bath of particles as shown in Fig. 2.2. For passive systems, the parallel plates will experience an attractive force towards each other when the gap spacing is on the order of the particle diameter, $H \sim 2a$. This attraction is often referred to result from the disjoining pressure [18, 19] or the Casimir effect in quantum mechanics [20, 21], and in colloid science it is known as depletion flocculation [22]. For active systems, Yan & Brady [13] and Ray et al. [17] showed, in independent studies, that for infinitely long walls the pressure on the interior walls depends on the gap spacing, and as the gap spacing decreases the pressure decreases as well. Additionally, Ray et al.'s simulation study showed that

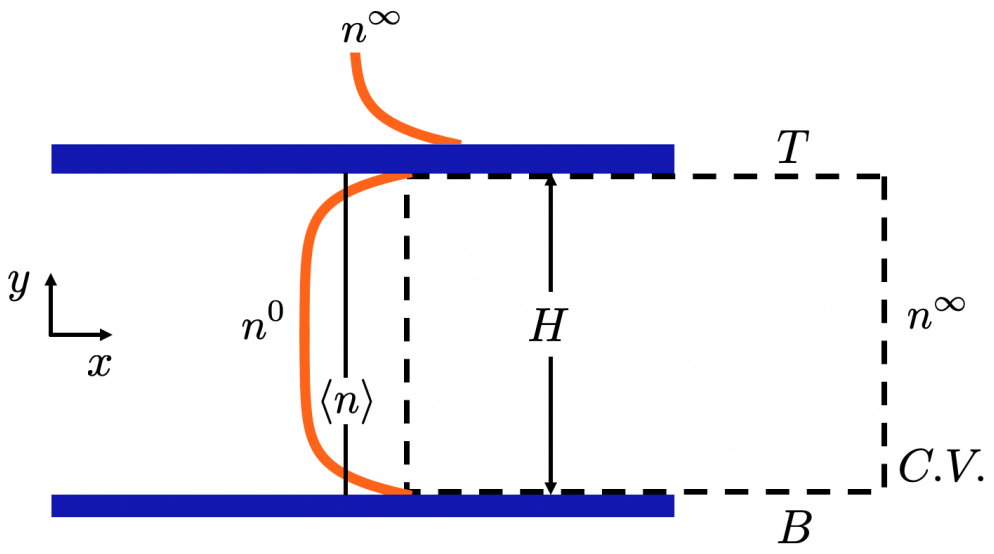

Figure 2.2: Illustration of two parallel plates in an active bath. The plates are separated by a distance H. C.V. denotes the control volume for the mechanical balance.

there is an attraction between parallel plates immersed in a bath of active particles.

The attraction arises from the difference in the forces exerted by the active particles on the interior and exterior plate surfaces. We quantify this force difference with $\Delta\Pi/\Pi^{\mathrm{W}}_{out}$, where $\Delta\Pi = \Pi^{\mathrm{W}}_{out} - \Pi^{\mathrm{W}}_{in}$, and Π^W is the force/unit area, or pressure, exerted by the ABPs on the plate surfaces.

An inherent property of active matter is that the particles accumulate at walls (and more generally at no-flux surfaces) due to their persistent motion. Yan & Brady [13] showed that the pressure on a single isolated wall is given by

$$\Pi^W_{out} = n^\infty (k_B T + k_s T_s), \tag{2.1}$$

where n^∞ is the number density far from the wall, $k_B T$ is the thermal energy, and $k_s T_s = \zeta U_0 \ell/2$ is the active energy, which is a measure of the activity level of the ABPs. Here, ζ is the Stokes drag coefficient of an ABP, and we are considering two-dimensional reorientation processes giving rise to the factor 2 in (2.1).

As shown by Yan & Brady [13], the expression for the pressure on the inner wall for two infinitely long plates is the same as (2.1), but with the centerline concentration

n^0 replacing n^∞. Thus, the net attractive force is given by the simple relation

$$\frac{\Delta\Pi}{\Pi^{\mathrm{W}}_{out}} = 1 - \frac{n^0}{n^\infty}. \tag{2.2}$$

The above expression holds when the accumulation boundary layers at each wall do not overlap, which is true for moderate to high activity ($k_s T_s / k_B T > 50$) and when the run length is comparable to the gap spacing. To complete the description, however, we need a relation between n^0 and n^∞; that is, we need to know how the APBs partition between the parallel plates and the surrounding reservoir.

For a thermodynamic system, such as charged plates in an ionic solution, the partitioning is determined by equating the chemical potentials inside and outside, $\mu_{in} = \mu_{out}$. The electrostatic system shares similarities with the active system: ions accumulate (or deplete) near the charged plates and display a non-homogeneous distribution between the plates [23]. However, since the ionic system is at equilibrium, the flux of each ion is zero at each and every point between the plates and in the reservoir. Thus, the centerline concentration of each ion is related to the reservoir concentration via its chemical potential: $n_i^0 = n_i^\infty \exp\left(-z_i e \phi^0 / k_B T\right)$, where n_i^∞ is the reservoir concentration of ion i, z_i is its valency, e is the elementary charge, and ϕ^0 is the potential at the centerline (relative to a zero level in the reservoir), which depends on the surface charge density on the plates. The attraction between the plates is then determined by a force balance and can be shown to be given by the ion osmotic pressure difference between the inside and the outside.

Active particles systems are inherently out of equilibrium and we cannot appeal to the chemical potential nor to a point-wise vanishing flux. For a dilute suspension of APBs, the particle distribution is governed by the Smoluchowski equation for the probability density $P(\boldsymbol{x}, \boldsymbol{q}, t)$ for finding a particle at position $\boldsymbol{x}$ with orientation $\boldsymbol{q}$ at time t:

$$\frac{\partial P(\boldsymbol{x}, \boldsymbol{q}, t)}{\partial t} + \nabla \cdot \boldsymbol{j}^T + \nabla_R \cdot \boldsymbol{j}^R = 0, \tag{2.3}$$

where the translational and rotational fluxes are $\boldsymbol{j}^T = U_0 \boldsymbol{q} P - D_T \nabla P$ and $\boldsymbol{j}^R = -D_R \nabla_R P$, respectively. Here, D_T and D_R are the translational and rotational diffusivities; the reorientation time $\tau_R = 1/D_R$. The orientational gradient operator is $\nabla_R = \boldsymbol{q} \times \nabla_{\boldsymbol{q}}$.

To make progress and capture the essential features of the distribution of ABPs, we expand the Smoluchowski equation in the first few orientational moments: the zeroeth moment is the concentration $n(\boldsymbol{x}, t) = \int P(\boldsymbol{x}, \boldsymbol{q}, t) d\boldsymbol{q}$, the first moment is

the polar order $\boldsymbol{m}(\boldsymbol{x},t) = \int \boldsymbol{q}P(\boldsymbol{x},\boldsymbol{q},t)d\boldsymbol{q}$, etc. For 2D, the orientational moments satisfy a hierarchy of equations [24]:

$$\frac{\partial n}{\partial t} + \nabla \cdot \boldsymbol{j}_n = 0, \tag{2.4}$$

$$\frac{\partial \boldsymbol{m}}{\partial t} + \nabla \cdot \boldsymbol{j}_m + D_R \boldsymbol{m} = 0, \tag{2.5}$$

where the fluxes are

$$\boldsymbol{j}_n = U_0 \boldsymbol{m} - D_T \nabla n, \tag{2.6}$$

$$\boldsymbol{j}_m = U_0 \boldsymbol{Q} + \frac{1}{2} U_0 n \boldsymbol{I} - D_T \nabla m. \tag{2.7}$$

Here, n is the number density, $\boldsymbol{m}$ is the polar order, and $\boldsymbol{Q}$ is the nematic order, $\boldsymbol{Q}(\boldsymbol{x},t) = \int (\boldsymbol{qq} - \frac{1}{2}\boldsymbol{I})P(\boldsymbol{x},\boldsymbol{q},t)d\boldsymbol{q}$, with $\boldsymbol{I}$ the isotropic tensor. The boundary conditions we impose are a constant number density in the reservoir far from the plates n^∞, and no polar or nematic order, $\boldsymbol{m}^\infty = 0$, $\boldsymbol{Q}^\infty = 0$, etc. The plates are hard no-flux walls, such that $\boldsymbol{n} \cdot \boldsymbol{j}^T = 0$ on the plates, where $\boldsymbol{n}$ is the surface normal, and the angular reorientation is unaffected by the plates.

While the system's behavior is fully determined from the Smoluchowski eqn (2.3), its solution, or that of the moment eqns (2.4) and (2.5), for any but the simplest geometries is a daunting task. Dimensional analysis shows that the distribution of particles between the plates depends on four lengths: the length of the plates L, the plates' separation H, the run length $\ell = U_0\tau_R$, and the microscopic diffusive step length $\delta = \sqrt{D_T\tau_R}$. The ratio of the run length ℓ to the microscopic length δ is also a measure of the active energy compared to the thermal energy $k_sT_s/k_BT = (\ell/\delta)^2/2$.

We are interested in large plates where $L \gg H$ and $L \gg \ell$, and high activity $\ell/\delta \gg 1$. In this limit, the force or pressure on the plates scales as the active pressure $n^\infty(k_BT + k_sT_s)$ and depends only on the confinement ℓ/H. Furthermore, to determine the attractive force between the plates, we only need an estimate of the centerline concentration—the partitioning between the reservoir and the plates. To accomplish this, we can appeal to a mechanical momentum balance.

At the microscopic level, the particles evolve according to the over-damped Langevin equation [24]:

$$0 = -\zeta \boldsymbol{U}_\alpha + \zeta U_0 \boldsymbol{q}_\alpha + \boldsymbol{F}^B_\alpha, \tag{2.8}$$

where ζ is the Stokes drag coefficient, $\boldsymbol{U}_\alpha$ is the velocity of particle α, and $\boldsymbol{q}_\alpha$ is its orientation. Each particle is also subject to random thermal forces $\boldsymbol{F}^B_\alpha$ that give

rise to translational Brownian motion, and which are characterized by $\overline{\boldsymbol{F}^B} = 0$ and $\overline{\boldsymbol{F}^B(0)\boldsymbol{F}^B(t)} = 2k_BT\zeta\delta(t)\boldsymbol{I}$, where the overline denotes averaging over the thermal fluctuations of magnitude k_BT and $\delta(t)$ is the Dirac delta function. The orientation vector $\boldsymbol{q}_\alpha$ undergoes a random reorientation process giving rise to rotary Brownian motion as detailed in s Section 2.6. (The Smoluchowski eqn (2.3) is the Fokker-Planck equation corresponding to the microscopic dynamics (2.8).)

From the microscopic dynamics (2.8), we can write a corresponding linear momentum or force balance [24]:

$$0 = -\zeta \boldsymbol{j}_n + \zeta U_0 \boldsymbol{m} + \nabla \cdot \boldsymbol{\sigma}^{osmo}\,, \tag{2.9}$$

where the flux is given by $\boldsymbol{j}_n \equiv n\frac{1}{N}\sum_{\alpha=1}^{N}\boldsymbol{U}_\alpha$, the polar order is $\boldsymbol{m} \equiv n\frac{1}{N}\sum_{\alpha=1}^{N}\boldsymbol{q}_\alpha$, and $\boldsymbol{\sigma}^{osmo} = -nk_BT\boldsymbol{I}$ is the osmotic pressure. In the force balance (2.9), $-\zeta\boldsymbol{j}_n$ is the average drag force from the suspending medium (which is assumed to be stationary), $\zeta U_0\boldsymbol{m}$ is the average propulsive or swim force, and since the average of the Brownian force is zero, its effect appears as the divergence of a stress $\nabla\cdot\boldsymbol{\sigma}^{osmo}$.

The similarity between the momentum balance (2.9) and the number density flux (2.6) is no coincidence—the flux is the mobility, $1/\zeta$, times the driving force, and the driving forces are the average swim force, $\zeta U_0\boldsymbol{m}$, and the stress gradient from Brownian motion, $\nabla\cdot\boldsymbol{\sigma}^{osmo}$. (The Stokes-Einstein-Sutherland relation connects the translational diffusivity to the drag, $D_T = k_BT/\zeta$.)

We now apply this momentum balance to the control volume (C.V.) illustrated in Fig. 2.2. Integrating the x-component over the C.V. gives

$$\langle n\rangle k_BT - n^\infty k_BT = \frac{1}{H}\int_{C.V.}\left(\zeta U_0 m_x - \zeta j_x^n\right)dxdy\,, \tag{2.10}$$

where $\langle n\rangle = \frac{1}{H}\int ndy$ is the average concentration between the plates as illustrated in Fig. 2.2. Eqn (2.10) is just a statement that the net body force in the C.V. is balanced by the osmotic pressure difference.

From (2.5) at steady state, the polar is $\boldsymbol{m} = -\tau_R\nabla\cdot\boldsymbol{j}_m$, and thus with (2.7) for the flux (2.10) becomes

$$\begin{aligned}(\langle n\rangle - n^\infty)(k_BT + k_sT_s) = &-2k_sT_s\langle Q_{xx}\rangle \\ &+ \frac{2}{H}\int_T\left(k_sT_sQ_{xy} - D_T\frac{\partial m_x}{\partial y}\right)dx \\ &- \frac{1}{H}\int_{C.V.}\zeta j_x^n dxdy\,,\end{aligned} \tag{2.11}$$

where the activity $k_sT_s = \zeta U_0^2 \tau_R/2$ and the integral in the second line is over the 'top' T in Fig. 2.2. Along the plate, $\boldsymbol{n} \cdot \boldsymbol{j}_m = 0$ and the integral over B is the same as over T; hence, the factor of 2. In obtaining (2.11), we have used the fact that far from the exit of the plates, both between the plates and into the reservoir, there is no variation with respect to x. We note that the balance is now with the active pressure—the sum of the osmotic pressure and the swim pressure [24, 25].

The first term on the RHS of (2.11) is the average nematic order at the left boundary of the C.V. far from the ends of the plates. Because $\boldsymbol{Q}$ is traceless, $\langle Q_{xx} \rangle = -\langle Q_{zz} \rangle$, and we can estimate $\langle Q_{xx} \rangle$ from the infinite parallel plate solution of Yan & Brady [13], which shows that this term is negligible ($|\langle Q_{xx} \rangle| < 0.005 \langle n \rangle$ for $\ell/\delta = 45$ and $\ell/H \in [0, 3]$).

The integrals on the RHS of (2.11) are only nonzero at the edges of the plates. In the reservoir, j_x^n is zero, as it is between the plates far from the edge. Fig. 2.10 shows that the magnitude of $\partial m_x/\partial y$ is small and localized in a very small region right at the exit of the plates. Thus, the mechanical balance predicts that $\langle n \rangle \approx n^\infty$. This balance has a very simple physical interpretation: the force per unit area of the left boundary of the C.V., which is the active pressure between the plates times the height $\langle n \rangle (k_BT + k_sT_s)H$, is equal to the force per unit area on the right boundary of the C.V., which is the active pressure in the reservoir times the height $n^\infty(k_BT + k_sT_s)H$.

The value of $\langle n \rangle / n^\infty$ measured from Brownian dynamics simulation is shown in the inset of Fig. 2.3 as a function of confinement ℓ/H with a plate length of $L/\ell = 10$; as expected, the connection is exact for passive particles $\ell/H \to 0$ and saturates to a constant as ℓ/H increases. For large ℓ/H, the average concentration between the plates is roughly 20% higher than the concentration in the bulk, which we believe to be caused by the finite thickness of the plates (in simulation) that adds an additional surface where particles accumulate and generate polar order which effects the macroscopic mechanical momentum balance. This is confirmed in Section 2.4 on periodic plates, where partitioning is determined as a function plate thickness, d, and reaches equal partitioning when $d/\ell \to 0$.

Finally, we need to relate the centerline concentration n^0 to $\langle n \rangle$. For this, we use the exact solution for the distribution between two parallel walls (assuming isotropic nematic order, which is a good approximation for simple systems) of Yan & Brady [13]:

$$\frac{n(y)}{n^0} = 1 + \frac{1}{2}\left(\frac{\ell}{\delta}\right)^2 \frac{\sinh(\lambda y) + \sinh(\lambda(H-y))}{\sinh(\lambda H)}, \tag{2.12}$$

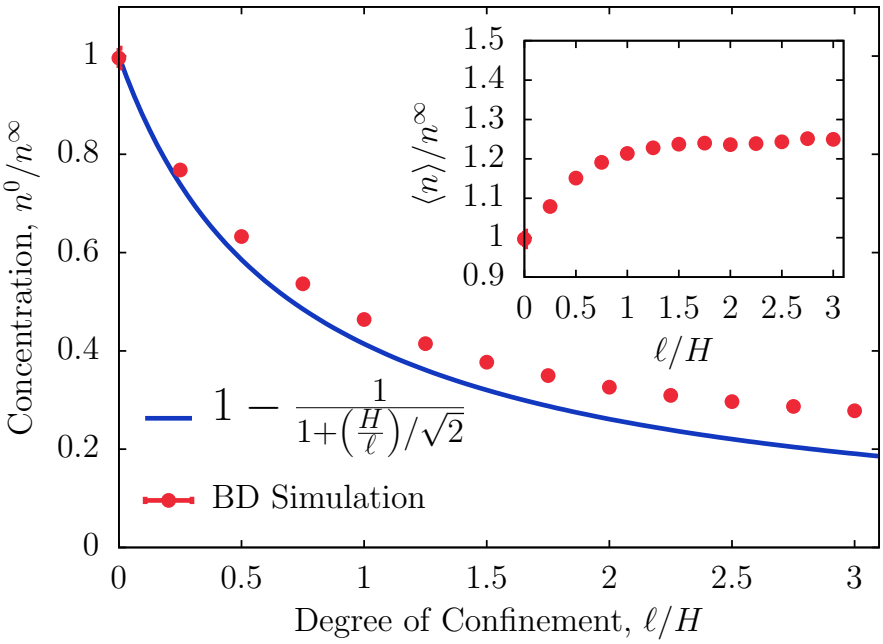

Figure 2.3: Centerline concentration, n^0/n^∞, as a function of the confinement, ℓ/H, for parallel walls. The relation $1 - 1/(1 + (H/\ell)/\sqrt{2})$ is derived from a simple mechanical balance. The inset shows the average concentration as a function of the degree of confinement.

where λ is the inverse thickness of the accumulation boundary layer, or the inverse screening length, $\lambda = \sqrt{1 + (\ell/\delta)^2/2}/\delta$. A straightforward integration over y relates n^0 to $\langle n\rangle$. In the limit of high activity $\lambda H \gg 1$, which is the most interesting case, we have

$$\frac{n^0}{\langle n\rangle} = 1 - \frac{1}{1 + (H/\ell)/\sqrt{2}}. \tag{2.13}$$

Fig. 2.3 shows a comparison between the predicted centerline concentration, using the mechanical balance's estimate of $\langle n\rangle \approx n^\infty$, and results from Brownian dynamics (BD) simulations. (See Section 2.6 for a description of the BD simulations.) The simulations are for a highly active system with strong confinement such that the smallest length, H, is on the order of the run length, and the degree of confinement, ℓ/H, is varied by changing the distance between the plates. Edge effects are minimized, since the parallel plates are made much longer than the particles' run length and the channel height. (The data in Fig. 2.3 and 2.4 are for $L/\ell = 10$ and $k_s T_s/k_B T = 1012.5$.) There is good qualitative agreement between the predicted center concentration from (2.13) and the one observed in the BD simulations.

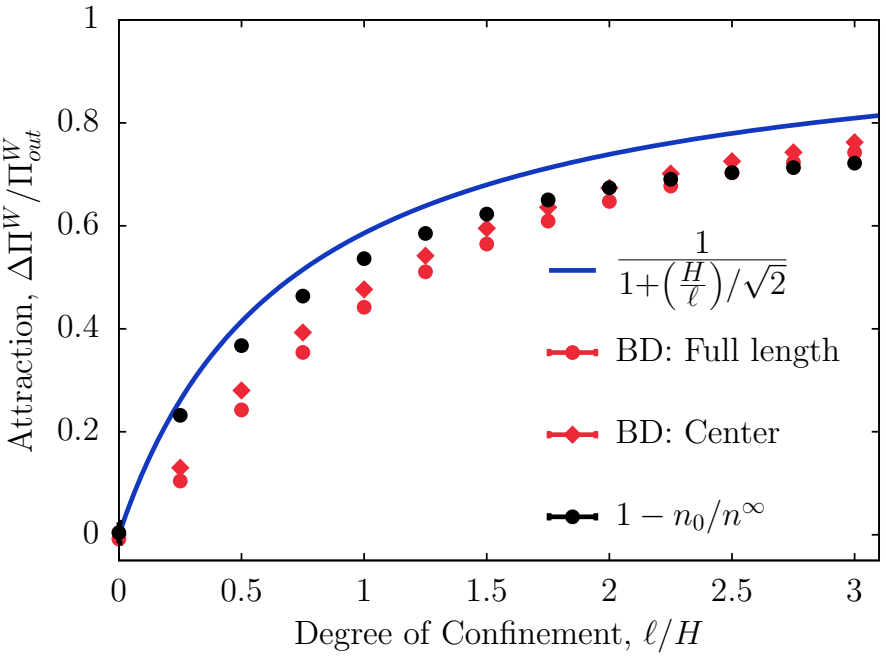

Figure 2.4: Attraction between parallel plates, $\Delta\Pi^W/\Pi^W_{out}$, as a function of the degree of confinement, ℓ/H. The relation $1/(1+(H/\ell)/\sqrt{2})$ is the predicted attraction from a simple mechanical balance, and $1-n^0/n^\infty$ is based on measuring concentration at the centerline *via* BD simulations.

From (2.2), the predicted attractive force is

$$\frac{\Delta\Pi}{\Pi^{\mathrm{W}}_{out}} = \frac{1}{1+(H/\ell)/\sqrt{2}}\,, \tag{2.14}$$

which is compared to BD simulations in Fig. 2.4. In the BD simulations, when a particle collides with a wall, it exerts a force on the wall, and the pressure is then the sum of individual particle contributions. In the simulations we used a potential-free algorithm [26–28] to model a hard-particle force (see Section 2.6). The prediction gives a good estimate for the attraction, both for that measured for the full length and the one measured only on the central portion $(1/3L)$ of the plates. As expected, the edge effects decrease the attractive force.

It should be appreciated that (2.14) is an *a priori* prediction with no adjustable parameters. All we needed to know was the behavior for two infinite parallel walls and then the macroscopic momentum balance for the partitioning into the parallel plates.

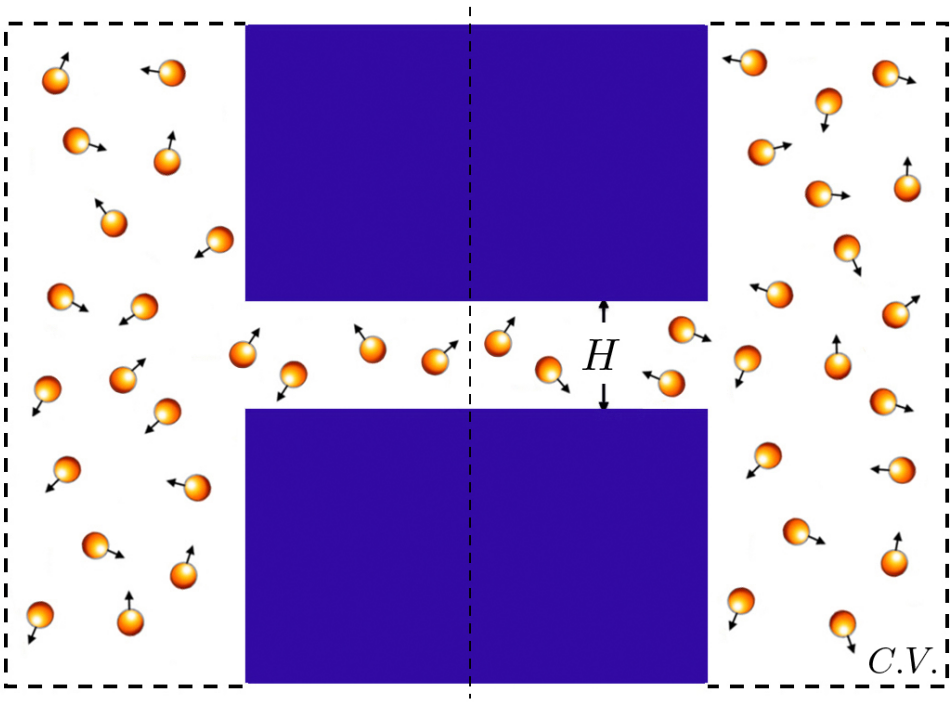

Figure 2.5: Illustration of two reservoirs connected by a channel of height H. The concentration of ABPs in the reservoir far from the channel is n^{∞}.

In the next section, we provide an example of a similar geometry that nevertheless exhibits a completely different behavior, but one that can also be predicted through an analogous macroscopic momentum balance.

2.3 Channel confinement

We now investigate the effect of confinement on ABPs in a channel of height H connected to a reservoir as shown in Fig. 2.5. This geometry is interesting because for passive Brownian particles, the partitioning between parallel plates and a channel is the same. This is also true for an ionic solution—the ion concentration in the channel or parallel plates is the same given by the equality of chemical potentials. As we shall see, for active particles the situation is profoundly different.

In Fig. 2.6, we show the average concentration in the channel far from the ends, $\langle n^{ch} \rangle / n^{\infty}$, as a function of confinement ℓ/H, along with the data for the parallel plates. The parallel plate results are for BD simulations with $\ell/\delta = 45$ and $L/\ell = 10$. For the channel geometry, we solved the full Smoluchowski eqn (2.3) numerically using a standard Galerkin P2-FEM method with adaptive mesh refinement. The finite

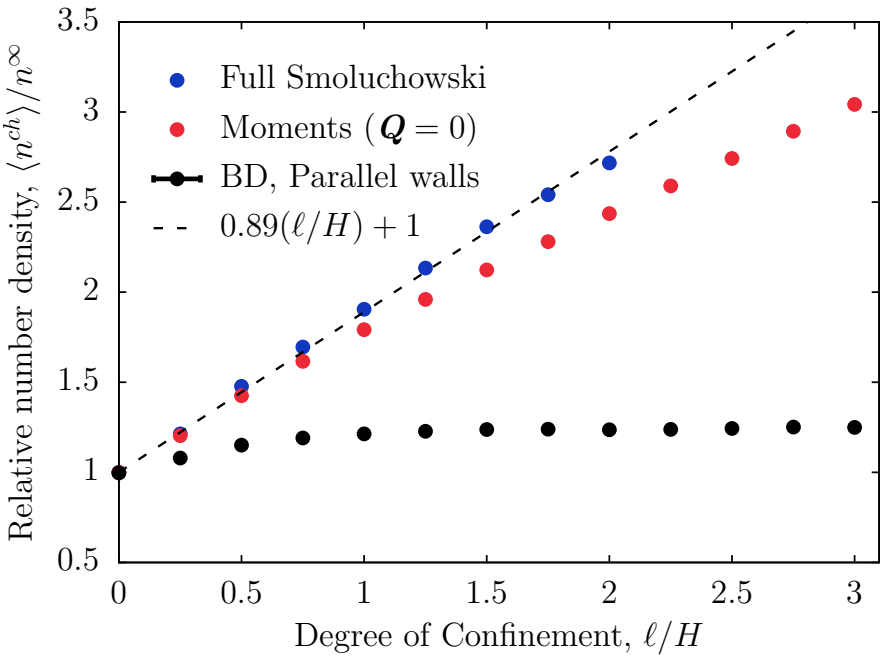

Figure 2.6: Numerical solution for the relative number density in a channel, $\langle n^{ch}\rangle/n^{\infty}$, as a function of degree of confinement, ℓ/H. The Brownian dynamics solution to the parallel plates geometry discussed earlier is also shown for comparison.

element method was carried out in *Freefem++* [29]. We also solved numerically the moment eqns (2.4)-(2.7) (with the $\boldsymbol{Q}=0$ closure) with *Freefem++*. (See *Appendix B* for details on the finite element calculations.) The dashed line in the figure is from BD simulations which have been fit to the linear relation: $\langle n^{ch}\rangle/n^{\infty} = 1+0.89(\ell/H)$. Rather than saturate to a value of approximately unity as for the parallel plates, in the channel geometry, the average concentration grows linearly with the degree of confinement! How can we explain this startling difference?

An explanation is provided by considering the behavior of the APBs at the channel opening and combining this with the mechanical momentum balance over a properly chosen control volume. In Fig. 2.7(a), ABPs slide along the solid wall resulting in a *uniform* concentration along the wall of magnitude $n^{W} = n^{\infty}(1+(\ell/\delta)^2/2) = n^{\infty}(1+k_sT_s/k_BT)$, where n^{∞} is the concentration far from the wall [13]. In Fig. 2.7(b), as particles slide along the wall from above and below the opening, they escape into the channel rather than continuing along the wall. This results in a deficit of particles just below and above the wall facing into the reservoir. This deficit is quantified in

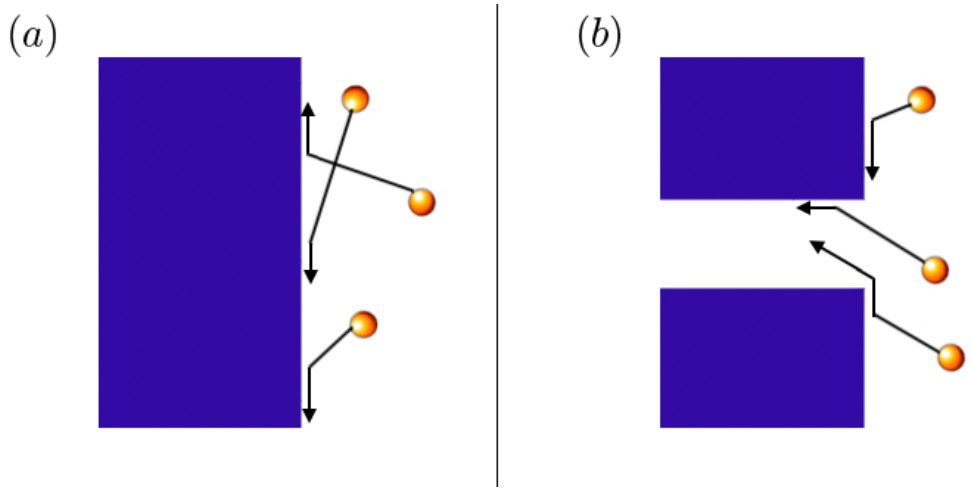

Figure 2.7: Illustration of (a) a wall with particles colliding and then sliding along it and (b) a wall with an opening where they also slide along it, but then move into the channel.

Fig. 2.8, and we see that it extends over a length $\Delta \approx 3\ell$ independent of both the degree of confinement, ℓ/H, and the level of activity, $k_sT_s/k_BT = (\ell/\delta)^2/2$.

As before, we integrate the x-momentum balance (2.9) over a C.V. that is the dashed lines in Fig. 2.1 making use of (2.7) as before:

$$\begin{aligned}(\langle n^{ch}\rangle - n^\infty)(k_BT + k_sT_s) = -2k_sT_s\langle Q_{xx}\rangle \\ - \frac{1}{H}\int_{C.V.} \zeta j_x^n dxdy \\ - \frac{2}{H}\int_0^\Delta (\Pi^W - \Pi^\infty)dy\,,\end{aligned} \tag{2.15}$$

where $\langle n^{ch}\rangle = \frac{1}{H}\int n(y)dy$, Π^W is the particle pressure on the wall facing the reservoir, and $\Pi^\infty = n^\infty(k_BT + k_sT_s)$ is the active pressure in the reservoir. The integral is over the concentration deficit at the wall. As for the parallel plates, the contributions from $\langle Q_{xx}\rangle$ and the integral of the flux are small. The result then has again a very simple physical interpretation: the total pressure on the left boundary of the C.V., $\langle n^{ch}\rangle(k_BT+k_sT_s)H+2\int_0^\Delta \Pi^W dy$, is equal to that on the right boundary, $n^\infty(k_BT + k_sT_s)(H + 2\Delta)$. Thus, the final expression for the partitioning is

$$\frac{\langle n^{ch}\rangle}{n^\infty} = 1 + \left(\frac{2}{H}\right)\frac{\int_0^\Delta [\Pi^\infty - \Pi^W(y)]dy}{\Pi^\infty}, \tag{2.16}$$

where $\Pi^W(y) = n^W(y)k_BT$ is the pressure on the wall at a distance y from the opening. Since the deficit is independent of confinement, ℓ/H, and activity, k_sT_s/k_BT,

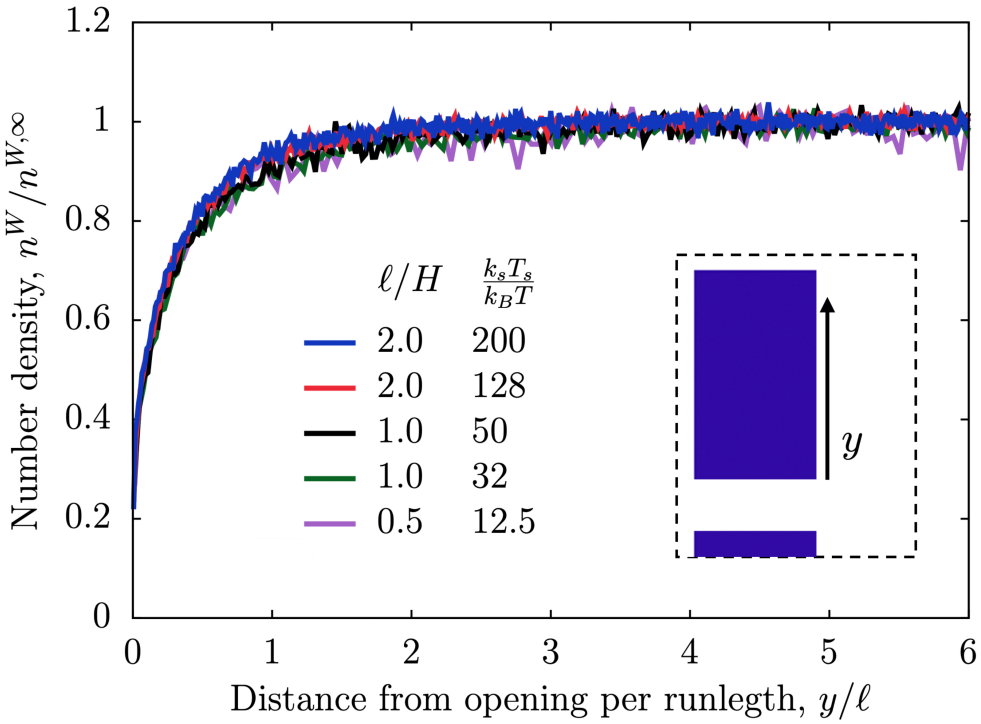

Figure 2.8: Number density at the wall normalized by the number density at the wall far from the opening as a function of distance from channel opening per run length measured from BD simulations. All the curves collapse onto one another independently of both degree of confinement and activity.

as shown in Fig. 2.8, we can compute the integral in (2.16) for one condition and use it to predict the partitioning for all conditions. We used the Π^W determined from BD simulations for $\ell/H = 2$ and $k_sT_s/k_BT = 10^3$. Fig. 2.9 shows excellent agreement between the predicted channel concentration from the macroscopic momentum balance and that from BD simulations and the solution of the full Smoluchowski equation.

Selection of the proper control volume is important in obtaining an accurate estimate of the partitioning. For example, for the channel geometry one could use a C.V. that is the same as for the parallel plates. If this C.V. were used, then instead of the integral over the pressure deficit along the wall facing the reservoir, one would have instead the integral along the 'top' as in (2.11): $+\frac{2}{H}\int_T \left(k_sT_sQ_{xy} - D_T\frac{\partial m_x}{\partial y}\right)dx$. (There is no integral on the top boundary in (2.15) because far from the channel exit, we have the behavior of a single isolated wall in contact with the reservoir.) Fig. 2.10 shows that the $\partial m_x/\partial y$ is much larger and longer ranged for the channel

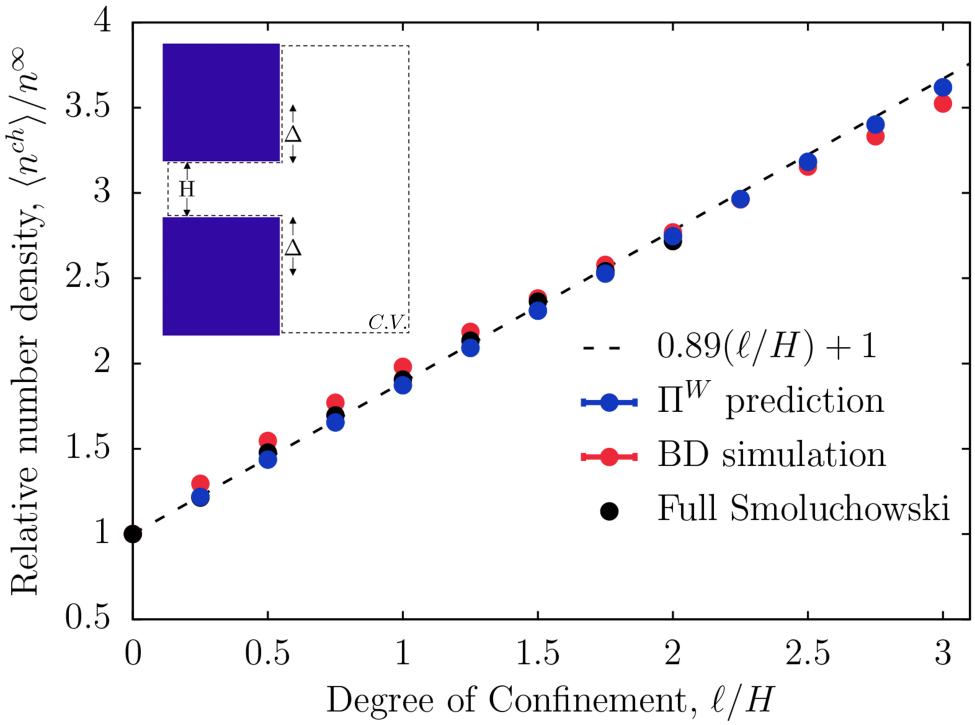

Figure 2.9: Relative number density in channel, $\langle n^{ch}\rangle/n^{\infty}$, as a function of the degree of confinement, ℓ/H. The inset shows the control area for the force balance. Δ is the length of the region at the wall experiencing a decreased pressure due to ABPs escaping into the channel.

geometry than the parallel plates, and thus, while this term's contribution is small for the parallel plates, it is not for the channel. The important point is that the C.V used in each geometry led to the very simple *physical* balance between the pressures on the two surfaces and thus to a reasonable estimate for the partitioning.

2.4 Periodic plates

As a last example, we consider the periodic plate geometry illustrated in the inset of Fig. 2.11. This geometry is intermediate between the parallel plates in an active bath and the channel connected to a reservoir. As the thickness of the plates, d, becomes very thin, one expects the partitioning to behave like the parallel plates shown earlier, but without the Casimir attraction since the plates are now placed periodically. In the other limit, when the plate thickness becomes very large, we expect the behavior to resemble the single channel geometry. Fig. 2.11 shows the relative number density between the periodic plates compared to that in the reservoir

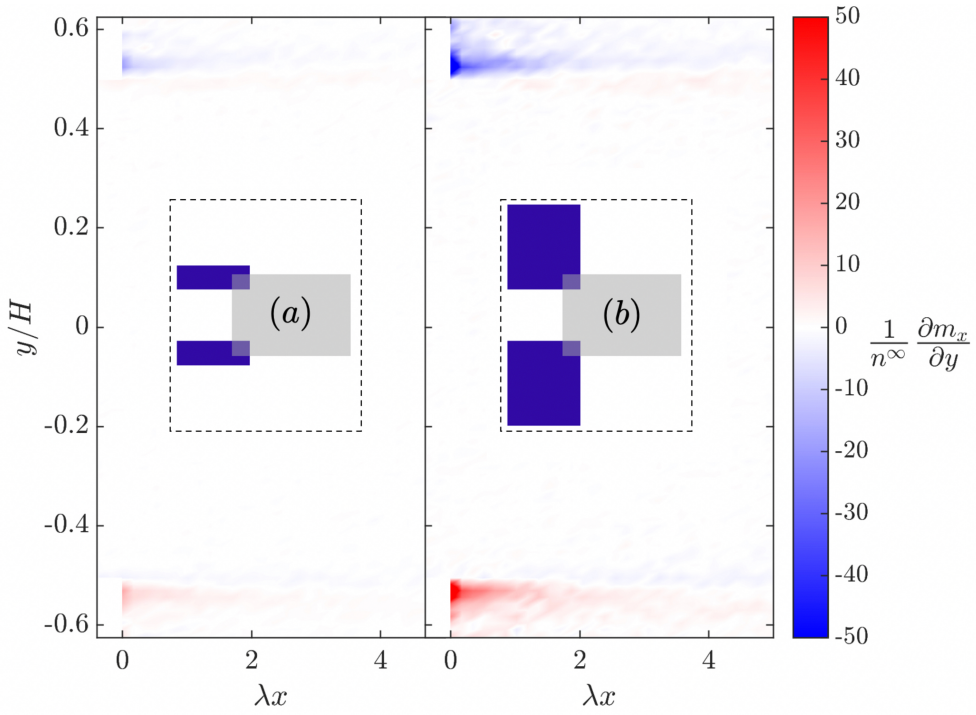

Figure 2.10: The change in polar order distribution in the y-direction, $(\mathrm{d}m_x/\mathrm{d}y)/n^\infty$, around the opening for (a) the parallel plates and (b) the channel geometry for $\ell/H = 3$ and $k_sT_s/k_BT \sim 3 \cdot 10^2$. The gray regions illustrate the area for which the change in polar order is shown.

for BD simulations with $k_sT_s/k_BT = 1012.5$ and $L/\ell = 10$. We recover the two limiting behaviors: as $d/\ell \to 0$, $\langle n\rangle/n^\infty \to 1$, and for large d/ℓ, the partitioning grows with ℓ/H.

The similarity of the curves in Fig. 2.11 suggest that they can be collapsed onto a single curve. We define a scaled concentration profile by first subtracting off the parallel plates result and then normalizing by the channel result for $d/\ell \gg 1$:

$$\frac{\overline{\Delta\langle n\rangle}}{n^\infty} = \frac{\langle n\rangle/n^\infty - 1}{\lim\limits_{d/\ell\to\infty}\left(\frac{\langle n\rangle}{n^\infty} - 1\right)}. \tag{2.17}$$

This collapse is shown in Fig. 2.12. Furthermore, the macroscopic momentum balance that led to (2.16) can be applied here by simply replacing Δ with $d/2$. Thus, from the momentum balance, we predict the scaled partitioning

$$\frac{\overline{\Delta\langle n\rangle}}{n^\infty} = \frac{\int_0^{d/2}\left[1 - \frac{\Pi^W(y)}{\Pi^\infty}\right]dy}{\int_0^{\Delta}\left[1 - \frac{\Pi^W(y)}{\Pi^\infty}\right]dy}. \tag{2.18}$$

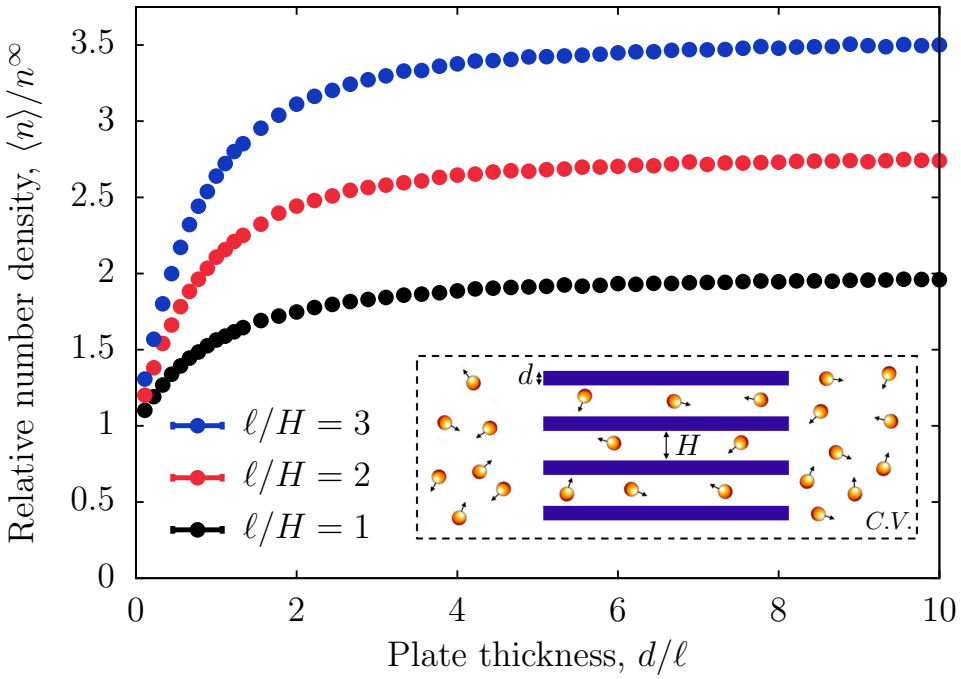

Figure 2.11: Normalized number density in the channels as a function of plate thickness for $k_s T_s / k_B T = 1012.5$ and $L/\ell = 10$. The inset shows the illustration of periodic plates, where d is the plate thickness and H is the separation between the plates.

And by assuming that the decrease in concentration (and thus pressure) near the corners has exactly the same functional form independent of the plate thickness, we can use the data for wall pressure obtained for the single channel. We applied the Π^W determined from BD simulations with $k_s T_s / k_B T = 128$, $L/H = 7.5$, and $\ell/H = 2$ in (2.4), and Fig. 2.12 shows excellent agreement between the prediction and the periodic plates simulations. This shows that the wall pressure follows the same functional form at the corners independent of plate thickness. Further, we see that the number density plateaus at a plate thickness of $d/\ell \approx 6$, which corresponds to twice the deficit distance. This is the smallest thickness needed to obtain the full concentration deficit near the plate corners and thereby obtain the maximum concentration between the plates. Adding additional thickness to the plates will have no effect on the partitioning between the channels and the reservoir.

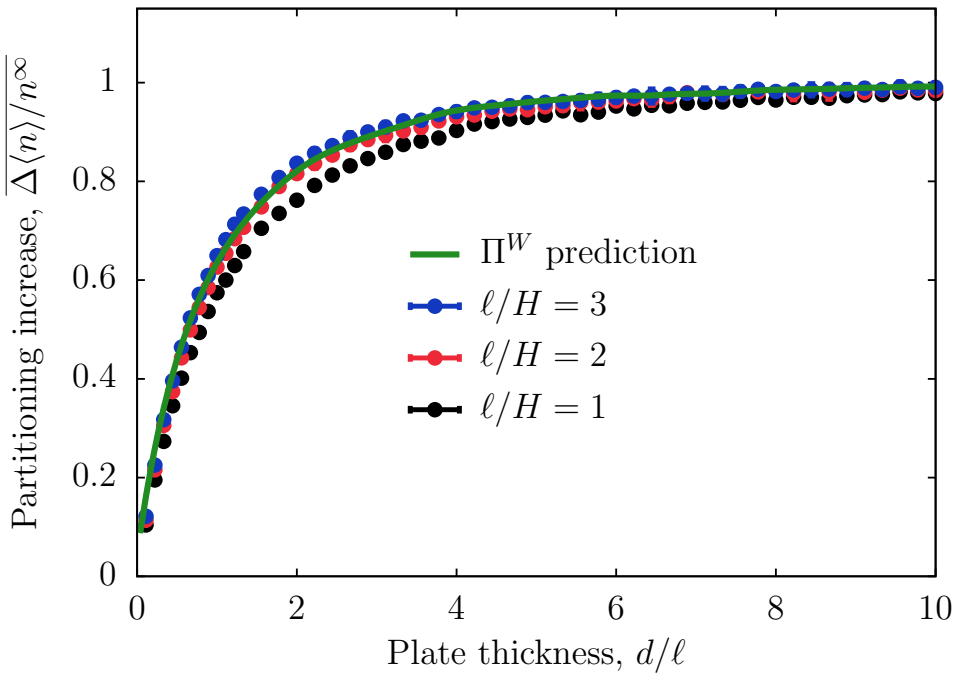

Figure 2.12: Partitioning increase as a function of the plate thickness (see eqn (2.17)) both for Brownian Dynamics simulation and that predicted from the momentum balance.

2.5 Conclusions

The attraction (Casimir effect) between parallel plates in a bath of active particles increases with the increasing degree of particle confinement (run length per plate spacing). Through a simple macroscopic mechanical momentum balance, we presented a method to predict the attraction that agrees well with BD simulations and the solution of the full Smoluchowski equation. The prediction has no adjustable parameters. This method was extended to the partitioning of ABPs between a channel and an infinite reservoir. In contrast to the parallel plates where the average concentration between the plates is the same as in the reservoir for all degrees of confinement, for the channel the average concentration in the channel grows linearly with the degree of confinement. It was shown that this results from a deficit of ABPs on walls of the reservoir near the channel opening. It is important to appreciate that the different behaviors in the two geometries results from the inherent nonequilibrium nature of the active particle dynamics; an equilibrium system would show no difference in the two geometries.

We hope that this simple approach of macroscopic momentum balances can be extended to other confinement problems and allow one to understand and predict behavior without having to perform computationally costly finite element calculations or Brownian dynamics simulations. Additionally, utilizing the insights in partitioning behavior for these fundamental geometries will be valuable in designing optimal structures for enhancing or isolating active particles.

Appendix

2.6 Brownian Dynamics simulations

The equations of motion implemented are the overdamped Langevin equations [24]:

$$\mathbf{0} = -\zeta \boldsymbol{u}_\alpha + \boldsymbol{F}_\alpha^{Swim} + \boldsymbol{F}_\alpha^{B} + \boldsymbol{F}_\alpha^{W}, \tag{2.19}$$

$$\mathbf{0} = -\zeta_R \boldsymbol{\Omega}_\alpha + \boldsymbol{L}_\alpha^{R}, \tag{2.20}$$

where $\boldsymbol{U}_\alpha$ is the translational velocity, $\boldsymbol{\Omega}_\alpha$ is the rotational velocity, ζ_R is the rotational Stokes drag coefficient, and $\boldsymbol{F}_\alpha^{Swim}$ is the swim force defined as $\boldsymbol{F}_\alpha^{Swim} \equiv \zeta U_0 \boldsymbol{q}_\alpha$. $\boldsymbol{F}_\alpha^{B}$ is the random Brownian force with the properties $\overline{\boldsymbol{F}_\alpha^{B}} = \mathbf{0}$ and the $\overline{\boldsymbol{F}_\alpha^{B}(0)\boldsymbol{F}_\alpha^{B}(t)} = 2k_B T\zeta\delta(t)\boldsymbol{I}$, where $\boldsymbol{I}$ is the identity tensor and $\delta(t)$ is the delta-function. $\boldsymbol{L}^R$ is the random reorientation torque, where $\overline{\boldsymbol{L}^R} = \mathbf{0}$ and $\overline{\boldsymbol{L}^R(0)\boldsymbol{L}^R(t)} = 2\zeta_R^2\delta(t)\boldsymbol{I}/\tau_R$. The simulations length scale is non-dimensionalized by the microscopic length $\delta = \sqrt{D_T/D_R}$ and the time steps are non-dimensionalized by the reorientation time τ_R, where $\tau_R = 1/D_R$ and $D_T = k_B T/\zeta$. Note that it is not necessary to assume that the translational and rotational diffusivities are both thermal, i.e. D_R need not be proportional to $k_B T$. Changes in orientation follow from $d\boldsymbol{q}/dt = \boldsymbol{\Omega} \times \boldsymbol{q}$, with $\boldsymbol{\Omega}$ from the particle angular momentum balance (2.20).

The particles are ideal and therefore only interact with the walls (no-flux boundaries) through the potential-free algorithm that models a hard-particle force [26–28]. This algorithm is implemented by placing a particle that overlaps with a wall back to the point of contact following along the boundaries normal vector until the system is free of overlaps.

We can determine the wall pressure from measuring the force on the wall per area, $\boldsymbol{F}^W/A$. The force exerted by an ABP on the wall is determined by measuring displacements at the wall. The force one ABP α exerts is

$$\boldsymbol{F}_\alpha^{W} = \zeta U_\alpha^{overlap} \boldsymbol{n} = \zeta \frac{\Delta x^{overlap}}{\Delta t} \boldsymbol{n}, \tag{2.21}$$

where $\Delta x^{overlap}$ is the overlap measured normal to the wall before the collision is resolved and Δt is the size of the time step. From the force exerted by the individual particles, the pressure at position z is given by

$$\Pi^W(z) = \sum_i^N \frac{\zeta U_i^{overlap}}{\Delta z}. \tag{2.22}$$

References

[1] E. Lauga and T. R. Powers, "The hydrodynamics of swimming microorganisms", Reports on Progress in Physics **72**, 096601 (2009).

[2] S. Granick, S. Jiang, and Q. Chen, "Janus particles", Physics Today **62**, 68–69 (2009).

[3] F. Wurm and A. F. M. Kilbinger, "Polymeric Janus particles", Angewandte Chemie-international Edition **48**, 8412–8421 (2009).

[4] S. C. Takatori and J. F. Brady, "Forces, stresses and the (thermo?) dynamics of active matter", Current Opinion in Colloid and Interface Science **21**, 24–33 (2016).

[5] S. Ramaswamy, "The mechanics and statistics of active matter", Annual Review of Condensed Matter Physics **1**, 323–345 (2010).

[6] S. A. Mallory, C. Valeriani, and A. Cacciuto, "An active approach to colloidal self-assembly", Annual Review of Physical Chemistry **69**, 59–79 (2018).

[7] C. Maggi, J. Simmchen, F. Saglimbeni, J. Katuri, M. Dipalo, F. De Angelis, S. Sanchez, and R. Di Leonardo, "Self-assembly of micromachining systems powered by Janus micromotors", Small **12**, 446–451 (2016).

[8] C. Bechinger, R. Di Leonardo, H. Löwen, C. Reichhardt, G. Volpe, and G. Volpe, "Active particles in complex and crowded environments", Reviews of Modern Physics **88**, 045006 (2016).

[9] D. A. Beard and T. Schlick, "Unbiased rotational moves for rigid-body dynamics", Biophysical Journal **85**, 2973–2976 (2003).

[10] S. C. Takatori, R. De Dier, J. Vermant, and J. F. Brady, "Acoustic trapping of active matter", Nature Communications **7**, 10694 (2016).

[11] W. M. Lai, D. Rubin, and E. Krempl, *Introduction to Continuum Mechanics, Revised Edition* (Pergamon, 1978), p. 324.

[12] B. Ezhilan, R. Alonso-Matilla, and D. Saintillan, "On the distribution and swim pressure of run-and-tumble particles in confinement", Journal of Fluid Mechanics **781**, R4 (2015).

[13] W. Yan and J. F. Brady, "The force on a boundary in active matter", Journal of Fluid Mechanics **785**, R1 (2015).

[14] X. Yang, L. Manning, and C. Marchetti, "Aggregation and segregation of confined active particles", Soft Matter **10**, 6477–6484 (2014).

[15] P. Galajda, J. Keymer, P. Chaikin, and R. Austin, "A wall of funnels concentrates swimming bacteria", Journal of Bacteriology **189**, 8704–8707 (2007).

[16] R. Di Giacomo, S. Krödel, B. Maresca, P. Benzoni, R. Rusconi, R. Stocker, and C. Daraio, "Deployable micro-traps to sequester motile bacteria", Scientific Reports **7**, 1–8 (2017).

[17] D. Ray, C. Reichhardt, and C. J. O. Reichhardt, "Casimir effect in active matter systems", Physical Review E **90**, 013019 (2014).

[18] B. V. Derjaguin, Y. I. Rabinovich, and N. V. Churaev, "Direct measurement of molecular forces", Nature **272**, 313–318 (1978).

[19] T. Franosch, S. Lang, and R. Schilling, "Fluids in extreme confinement", Physical Review Letters **109**, 1–5 (2012).

[20] G. Bressi, G. Carugno, R. Onofrio, G. Ruoso, R. Onofrio, and G. Ruoso, "Measurement of the Casimir force between parallel metallic surfaces", Physical Review Letters **88**, 4 (2002).

[21] S. K. Lamoreaux, "The Casimir force: Background, experiments, and applications", Reports on Progress in Physics **68**, 201–236 (2005).

[22] P. Jenkins and M. Snowden, "Depletion flocculation in colloidal dispersions", Advances in Colloid and Interface Science **68**, 57–96 (1996).

[23] R. A. Robinson and R. H. Stokes, *Electrolyte Solutions: The Measurement and Interpretation of Conductance, Chemical Potential, and Diffusion in Solutions of Simple Electrolytes* (Academic Press, 1959), p. 76.

[24] W. Yan and J. F. Brady, "The swim force as a body force", Soft Matter **11**, 6235–6244 (2015).

[25] S. C. Takatori, W. Yan, and J. F. Brady, "Swim pressure: Stress generation in active matter", Physical Review Letters **113**, 028103 (2014).

[26] D. M. Heyes and J. R. Melrose, "Brownian dynamics simulations of model hard-sphere suspensions", Journal of Non-Newtonian Fluid Mechanics **46**, 1–28 (1993).

[27] W. Schaertl and H. Sillescu, "Brownian dynamics simulations of colloidal hard spheres. Effects of sample dimensionality on self-diffusion", Journal of Statistical Physics **74**, 687–703 (1994).

[28] D. R. Foss and J. F. Brady, "Brownian dynamics simulation of hard-sphere colloidal dispersions", Journal of Rheology **44**, 629–651 (2000).

[29] F. Hecht, "New development in freefem++", Journal of Numerical Mathematics **20**, 251–265 (2012).

Chapter 3

PARTITIONING OF ACTIVE PARTICLES INTO POROUS MEDIA

Passive Brownian particles partition homogeneously between a porous medium and an adjacent fluid reservoir. In contrast, active particles accumulate near boundaries and can therefore preferentially partition into the porous medium. Understanding how active particles interact with and partition into such an environment is important for optimizing particle transport. In this work, both the initial transient and steady behavior as active swimmers partition into a porous medium from a bulk fluid reservoir are investigated. At short times, the particle number density in the porous medium exhibits an oscillatory behavior due to the particles' ballistic motion when time $t < \tau_R$, where τ_R is the reorientation time of the active particles. At longer times, $t > L^2/D^{swim}$, the particles diffuse from the reservoir into the porous medium, leading to a steady state concentration partitioning. Here, L is the characteristic length scale of the porous medium and $D^{swim} = U_0\ell/d(d-1)$, where U_0 is the intrinsic swim speed of the particles, $\ell = U_0\tau_R$ is the particles' run, or persistence, length, and d is the dimension of the reorientation process. An analytical prediction is developed for this partitioning for spherical obstacles connected to a fluid reservoir in both two and three dimensions based on the Smoluchowski equation and a macroscopic mechanical momentum balance. The analytical prediction agrees well with Brownian dynamics simulations.

This chapter includes content from our previously published article:

[1] C. M. Kjeldbjerg and J. F. Brady, "Partitioning of active particles into porous media", Soft Matter **18**, DOI: 10.1039/d1sm01752g, 2757–2766 (2022),

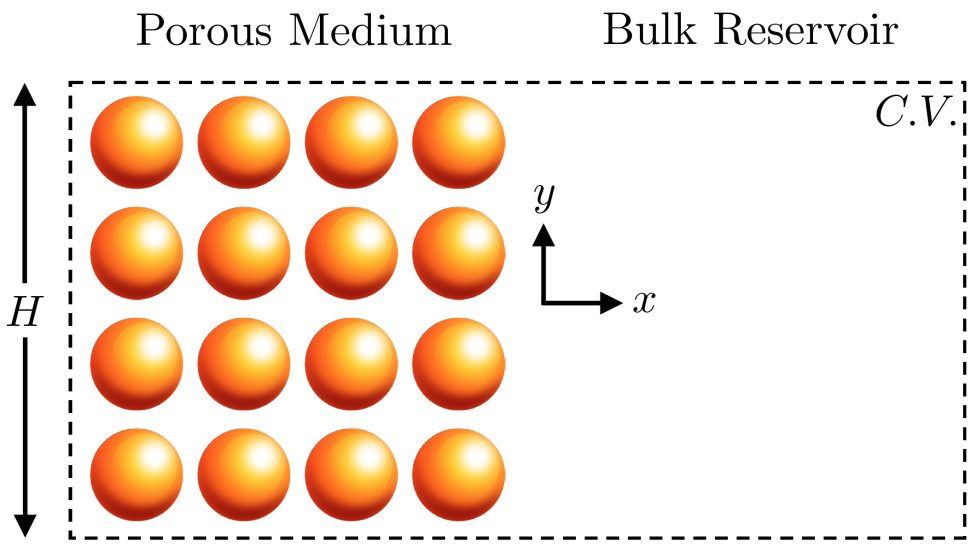

Figure 3.1: Illustration of the porous medium model (i.e., an array of spheres connected to a reservoir). The obstacles are fixed, and active particles can move freely around them; further, the system is periodic in the y-direction.

3.1 Introduction

Active matter systems span a large range of length scales from bacteria and micromotors to schools of fish and humans moving in a crowded area [1–3]. The activity arises from particles self-propulsion by converting chemical energy to persistent mechanical motion [4]. This motion leads to interesting phenomena such as self-assembly, accumulation at boundaries, and the conversion of chemical energy into mechanical work through 'micro-gears' [5–7]. The utilization of new developments, such as active particle microrobots for drug therapy [8] and bacterial sequestering technologies [9], will depend on understanding not only the behavior of active particles in bulk but also in confined spaces and crowded environments such as porous media. How active particles partition into porous media and how to predict this behavior is the focus of this paper.

The simplest model that captures the essential physics of active particles is the active Brownian particle (ABP) model, wherein each particle translates with a swim speed U_0 in a direction $\boldsymbol{q}$ for a characteristic reorientation time τ_R; the average length they move between each reorientation is called the run, or persistence, length $\ell = U_0\tau_R$ [10]. Owing to this persistent swimming, the ABPs distribute non-homogenously near surfaces, accumulating at no-flux boundaries leading to a concentration boundary layer near solid surfaces [4, 11, 12].

In free space, the random reorientation of ABPs result in diffusive motion with $D^{swim} = U_0\ell/d(d-1)$, where d is the dimension of the reorientation process. The active swim diffusivity can be much larger than the thermal diffusivity of "passive" Brownian particles. Solid boundaries and other obstacles change the free space available to these particles and can dramatically shorten the mean-free path; this cuts off their run length, reduces the diffusivity, and causes accumulation at boundaries [11, 13]. Alonso-Matilla *et al.* studied Taylor dispersion in circular arrays and observed, even without flow, a decrease in diffusivity for low activity particles resembling the behavior observed for passive particles [14]. Experimental studies of *Chlamydomonas Reinhardtii* show that the diffusion of algae is obstructed by arrays of pillars and becomes lower than it would be in the free space [15]. It has been shown experimentally that bacteria in a microfluidic crystal lattice (porous media) exhibit Taylor-Aris dispersion. [16] Additionally, in highly crowded environments, *E. coli* has been observed to display an interesting hopping-trapping behavior; *E. coli* is trapped in pockets of space between densely packed obstacles and then hops through highly confined channels into other pockets of pore space [17]. Chamolly *et al.* studied how activity impacts particle trajectories around a periodic lattice. [18] Further, porous media significantly impacts the chemotactic migration of bacteria as confinement strongly influences the directed motion and can cause active particles to move with the same orientation over great lengths. [19, 20] Reichhardt and Reichhardt have conducted multiple studies of the effect of confinement on motility induced phase separation in dense solutions of active particles. [21, 22]

Partitioning is a standard concept from thermodynamics, where Henry's law governs the concentration between two phases such that $C_A^I = K \cdot C_A^{II}$. [23, 24] The partition coefficient, K, for a thermodynamic system would be determined from equality of chemical potential in the two regions, $\mu_A^I = \mu_A^{II}$. In the simplest case of hard-sphere interactions for equilibrium Brownian systems the concentration in the pore space is equal to that in the reservoir.

Even though one cannot apply the concept of a chemical potential for active matter systems, concentration distributions (or partitioning) are well understood for fundamental confining geometries such as in-, and outside a single sphere, around parallel plates in a reservoir, and channels in a wall [11, 25]. However, there is a lack of knowledge regarding the partitioning of active particles for more complex environments.

This work explores both the transient and steady-state partitioning of active particles between a fluid reservoir and a porous medium (i.e., arrays of spherical obstacles).

The particles interact with the obstacles through excluded volume interactions *only*. Utilizing scaling arguments relating to particle properties and geometric parameters, we explain the initial oscillations in the concentration in the bulk of the porous medium in two dimensions. We then derive a theory for the long-time partitioning between the porous medium and the reservoir in two and three dimensions based on a mechanical balance and the concentration distribution outside a single obstacle. At high activity the theory predicts

$$\frac{\langle n_{pore} \rangle}{n^{\infty}} = 1 + \frac{\sqrt{d}/(d-1)\ \ell/R}{1 + 1/\sqrt{d}\ \ell/R}\ \frac{\phi}{1-\phi}, \tag{3.1}$$

where $\langle n_{pore} \rangle$ is the average concentration in the pore volume of the porous medium, n^{∞} is the bulk concentration in the fluid reservoir, ϕ is the volume (or area) fraction of obstacles of size R in the porous medium, and ℓ is the run length. The analytical prediction agrees well with Brownian dynamics simulations. The theory and simulations suggest that a mixture of bacteria having different run lengths can be separated by contacting the solution with a porous medium whose geometric structure has a length scale $R \sim \ell$.

3.2 Transient evolution

We model a porous medium as an array of fixed disks (2D) on a lattice in contact with a fluid reservoir as illustrated in Fig. 3.1. The active particles can move in both the reservoir and in the free pore space of the porous medium. They cannot penetrate the obstacles and collide with them via excluded volume interactions. In the next section, we predict the steady-state behavior using a mechanical balance, but first we investigate the transient behavior. As previously mentioned, active particles accumulate at boundaries, and the simplest example of boundary accumulation is that of a single flat wall. Yan & Brady [11] determined that the number density n as a function of distance from the wall z at steady state is given by

$$n(z) = n^{\infty}\left(1 + \frac{k_s T_s}{k_B T}\exp\left(-\lambda z\right)\right), \tag{3.2}$$

where $k_B T$ is the thermal energy, $k_s T_s = \zeta U_0 \ell/d(d-1)$ is the analogous active energy scale, and n^{∞} is the concentration far from the wall. Here ζ is the drag coefficient of an ABP (see Appendix 3.5). The accumulation layer decays exponentially with distance from the wall with screening length, $\lambda^{-1} = \delta/\sqrt{1 + (\ell/\delta)^2/2}$, where $\delta = \sqrt{D_T \tau_R}$ is the microscopic diffusive length and D_T is the thermal diffusivity. The ratio of the active energy scale to the thermal one can be expressed as the ratio

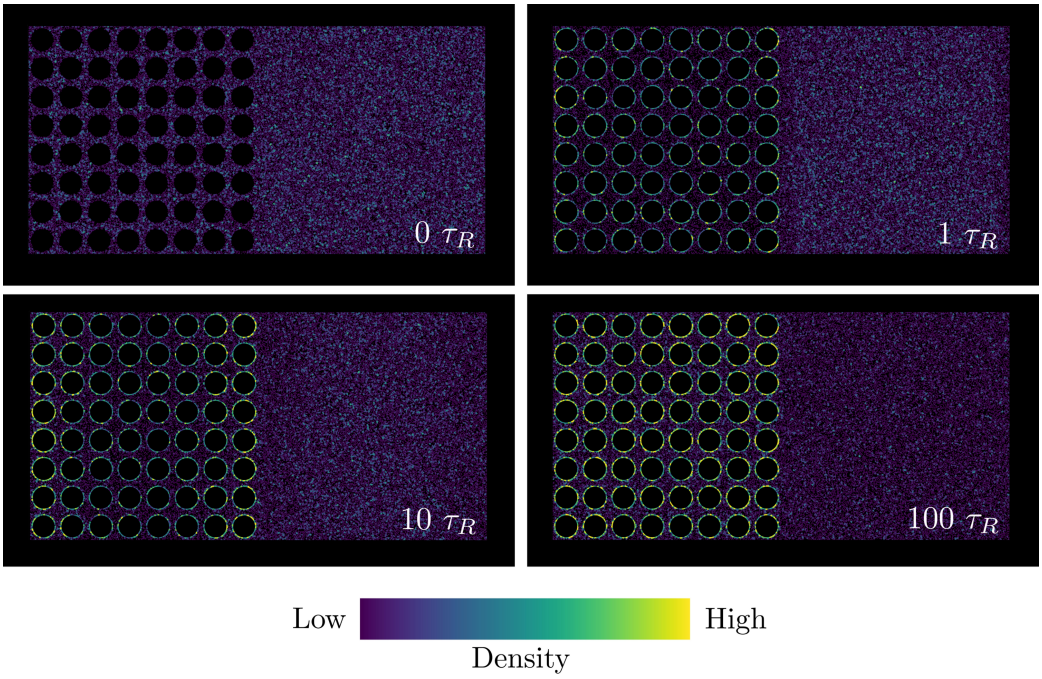

Figure 3.2: Brownian dynamics simulation snapshots of particle density in the system for $k_sT_s/k_BT = 800$, $\phi = 0.5$, $\ell/R = 0.5$, and times $0\tau_R$, $1\tau_R$, $10\tau_R$, and $100\tau_R$. The circular obstacles are shown as black disks for clarity. The system is periodic in that there is an equivalent reservoir region to the left of the porous medium. Initially, the active particles are distributed homogeneously throughout the pore space and the reservoir such that the density is the same everywhere. The density within the pore space is based only on the free space available (see eq. 3.3). At $1\tau_R$, particles in the porous region accumulate at the obstacle surfaces, causing the concentration in the pore space to become lower than in the reservoir. At $10\tau_R$, the reservoir particles have had time to diffuse into the outer parts of the medium. Thus, the outer obstacles have a larger surface concentration than the inner obstacles, while the reservoir concentration decreases. At longer times, $100\tau_R$, the particles from the reservoir have had time to diffuse through the entire medium, and the system is near steady state.

of run length to diffusive step: $k_sT_s/k_BT = (\ell/\delta)^2/2$ in 2D [4, 11].

In the porous medium, the amount of boundary available depends on the area (or volume) fraction of obstacles, $\phi = N\pi R^2/A$, where N is the number of obstacles in the total area of the porous region, A, and R is the radius of an obstacle. (The ABPs have no size. One can give them a size from the Stokes drag $\zeta = 6\pi\eta a$, where η is the fluid viscosity. In this work, the obstacle size R includes the ABP radius 'a' in

its definition.) The total average number density of ABPs in the medium is defined as,

$$\langle n_{pore} \rangle = \frac{N_{ABP}}{A_f} = \frac{N_{ABP}}{A(1-\phi)}, \tag{3.3}$$

where N_{ABP} is the number of ABPs in the free pore space, $A_f = A(1-\phi)$. We also define the number density outside the accumulation boundary layer as $n^0_{pore} = N^*_{ABP}/A^*_f$, where A^*_f is the adjusted free space available excluding the area within a distance of 10 screening lengths from obstacle surfaces and N^*_{ABP} is the number of particles in A^*_f, such that only particles in the bulk pore space are included in this quantity. The inset of Fig. 3.8 shows the adjusted free space over which n^0_{pore} is measured. The number density of swimmers in the reservoir is n^∞.

Both the initial and long time behavior will be set by the activity and the geometry. The inset of Fig. 3.4 illustrates the characteristic length scales. From dimensional analysis there are three dimensionless groups: ℓ/δ, ℓ/R, and R/L. The ratio of ℓ/δ describes the activity, ℓ/R is the ratio of particle run length to the size of an obstacle, and R/L relates to the porosity of the medium, which is also expressed as $\phi = \pi R^2/L^2$, where L is the length of one lattice unit cell. Thus, the transient evolution will be governed by these three dimensionless groups.

The evolution of the number density for the two-dimensional system is shown in Fig. 3.2 at four times: 0 τ_R, 1 τ_R, 10 τ_R, and 100 τ_R. These results are from dilute Brownian dynamics (BD) simulations for $k_s T_s/k_B T = 800$, $\phi = 0.5$, $\ell/R = 0.5$ and 10^7 ABPs. The particles interact with obstacles through a hard-particle force, which is implemented via a potential-free algorithm [26–28]. (See Appendix 3.5 for a description of the BD simulations.) Obstacles are shown as black disks, and each active particle is color-coated with its surrounding density such that purple is low density and yellow is high density. Initially, at 0 τ_R, the particles are distributed homogeneously throughout the pore space of the porous medium and the reservoir. At 1 τ_R, the particles can move one run length, and, as expected, particles accumulate at the obstacle surfaces leading to a lower concentration in the pore space of the porous medium compared to that in the reservoir. In Fig. 3.2, this is observable through the pore space of the porous medium being dark purple, while the reservoir concentration is a lighter blue. We go into more detail surrounding this lower concentration in the next section.

At 10 τ_R, the particles from the reservoir have had time to diffuse into the outer edge of the porous region, where we observe a higher concentration of ABPs at the outer obstacles' surfaces, while simultaneously observing a lower concentration

in the reservoir. Last, at 100 τ_R, the active particles from the reservoir have had time to diffuse through the entire porous region. There are high-density boundary layers around all obstacles, while a significantly lower reservoir concentration than initially. Hence, we observe a partitioning in concentration at steady state.
In summary, two phenomena dominate the transient changes in particle concentration: 1) the persistent motion of the particles within the porous medium and 2) particles diffusing from the reservoir into the porous medium. The following sections describe these phenomena in more detail.

Initial oscillations in concentration

Changes in concentration in the porous medium and the reservoir are interdependent, but initially, we can consider concentration changes in the porous medium without accounting for the effects coming from the reservoir. Particles from the reservoir require time to diffuse into the porous region, and until then the average number density in the porous medium, $\langle n_{pore} \rangle$, will be constant.
The evolution in the pore space of the porous medium, n^0_{pore} from 0 to 20 τ_R is shown in Fig. 3.3. Interestingly, we initially see oscillations in the bulk number density, then a temporary constant concentration until around $5 - 10\ \tau_R$. After this, the bulk number density increases again as the reservoir particles have had time to diffuse into the porous medium. ABPs exhibit ballistic behavior at short times [29], which leads to this short-time oscillatory behavior.

We can predict when the minimum in bulk number density will occur using knowledge of this ballistic behavior. Initially, particles can move their run length and leave the pore space when they collide with an obstacle. A particle will not reenter the pore space until it reorients, which leads to a minimum in the pore space concentration. The time it takes to reach the first minimum depends on the run length of the particle compared to the length available before colliding with an obstacle, expressed through ϕ. For a given activity, a more dense system will reach the minimum faster, and this is apparent in Fig. 3.3. To obtain a scaling for the minimum, we use the average length a particle moves before colliding with an obstacle. At close packing or strong confinement, we expect the length to be $L/2$ on average, while for low packing fraction, we would expect that particles can move the full length, L. Thus, we estimate the minimum by the time it takes an ABP to travel the length $L = 2R + h$, where h is the shortest distance between obstacles (as illustrated in the

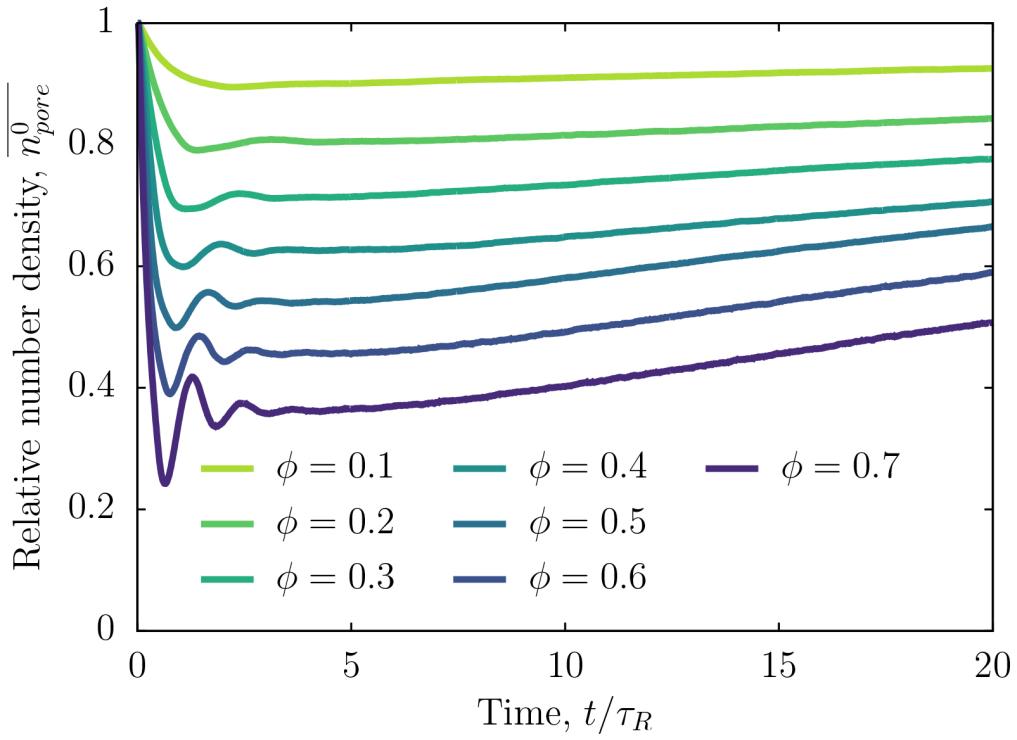

Figure 3.3: Normalized number density in the pore space of the porous medium, $\overline{n^0_{pore}} = n^0_{pore}/n^0_{pore}(t = 0)$ as a function of time for $\ell/R = 0.5$, $k_s T_s/k_B T = 800$, and $\phi = 0.1 - 0.7$. The measured densities oscillate initially due to the accumulation at boundaries, when particles leave the pore space, due to their short-time ballistic nature, and then reach a temporary constant state until around a time of $5\tau_R$, after which the particles from the reservoir are diffusing into the medium and the density again increases.

inset of Fig. 3.4);

$$\frac{t_{\min}}{\tau_R} \sim \frac{L}{\ell} \sim \sqrt{\frac{\pi}{\phi}} \cdot \frac{R}{\ell} \tag{3.4}$$

where $t_{\min}$ is the time to reach the minimum, τ_R is the reorientation time, and L is the length of the lattice unit cell. As mentioned, we expect the average length a particle will move before colliding to be between $L/2$ and L. Thus, we choose a scaling fit in-between the two ($3/4$ L/R). We compare this scaling prediction with $t_{\min}$ measured from BD simulations. The result is shown for $t_{\min}$ scaled with ℓ/R in Fig. 3.4, such that one can compare results for different degrees of confinement, $R/\ell = 1$, $1/2$, and $1/4$. The gold shaded area marks the interval of average travel distance between $L/2$ (lower bound) and L (upper bound). We obtain good agreement between our scaling prediction and the simulation results. As expected, near close

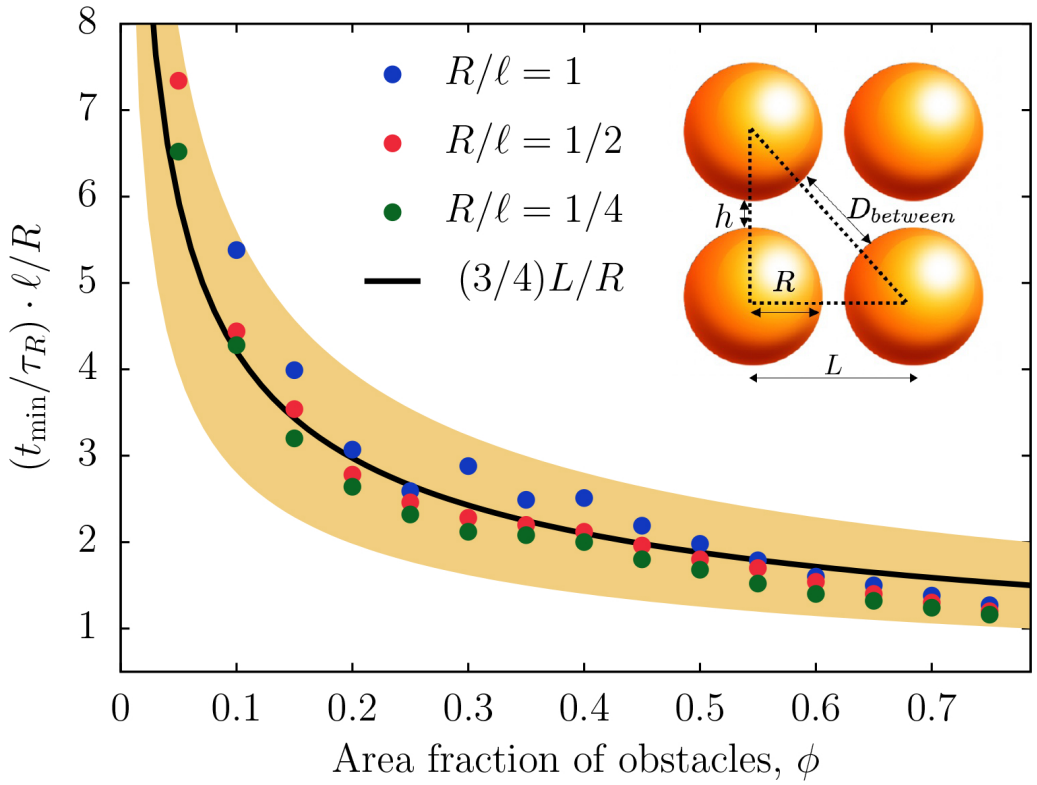

Figure 3.4: Time to reach the initial local minimum in pore space concentration scaled by ℓ/R as a function of area fraction of obstacles, ϕ for $k_s T_s/k_B T = 800$ and $R/\ell = 1$, $1/2$, and $1/4$. The inset illustrates the four characteristic dimensions in the porous medium; h, R, $D_{between}$, and L. The black line corresponds to (3.4) with a scaling coefficient of 3/4. The gold shaded area is the interval of time between traveling an average length of $L/2$ (lower bound) and L (upper bound). At higher area fractions, the particles experience more confinement and travel a shorter distance before colliding with an obstacle than for lower area fractions.

packing or highly confined, the characteristic length to reach minimum is closer to $L/2$, while for lower confinement, the particles on average move L before reaching the minimum concentration.

Now that we have obtained a prediction for the $t_{\min}$, we can explore the number density at minimum. This will be related to the area fraction of obstacles in the medium. The larger the area fraction, the closer packed the obstacles will be and more particles will be at the boundary compared to the bulk. We propose a simple linear scaling: $n^0_{pore}(t_{\min})/n^0_{pore}(t = 0) = 1 - \alpha \cdot \phi$, where α is a constant. This leads to the behavior shown in Fig 3.5, where the dashed lines are linear regressions for $n^0_{pore}(t_{\min})$ computed on ϕ between 0 and 0.6. We observe linear dependence

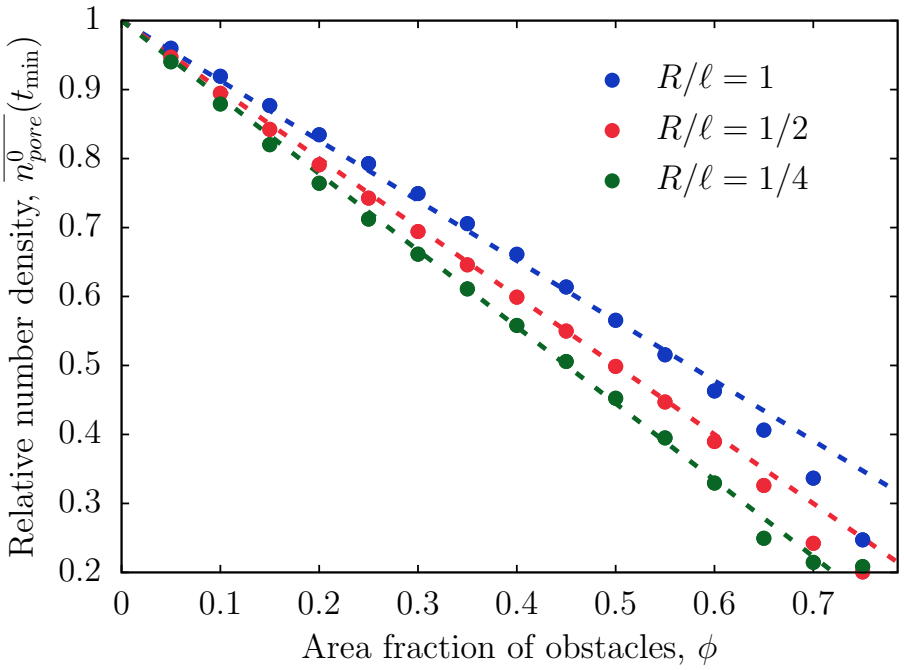

Figure 3.5: The porous medium pore space number density at the initial local minimum, $\overline{n^0_{pore}(t_{\min})} = n^0_{pore}(t_{\min})/n^0_{pore}(t = 0)$, as a function of area fraction of obstacles, ϕ, for $k_s T_s/k_B T = 800$ and $R/\ell = 1$, $1/2$, and $1/4$. The decrease in concentration with increased obstacle fraction is linear until near close packing. The dashed lines are linear fit to $\overline{n^0_{pore}} = 1 - \alpha\phi$ with $\alpha = 0.87$, 1 and 1.11 for $R/\ell = 1$, $1/2$ and $1/4$, respectively.

on volume fraction until near close packing.

Porous media as a sponge

The concentration in the center of the reservoir initially remains constant until 5 τ_R, after which it rapidly decreases before reaching a steady value. The changes in reservoir concentration, n^∞, scaled by the initial concentration, $n^\infty(t = 0)$, are shown in Fig. 3.6. The steady-state concentration in the reservoir depends on the volume fraction of the porous medium. The higher the volume fraction, the lower the reservoir concentration, even though there is less pore space in the denser porous medium! The porous medium acts as a sponge and soaks up the ABPs.

This emptying of the reservoir poses exciting opportunities for application design. Imagine a bath of active particles, such as bacteria, and wanting to remove them. One could temporarily insert a porous medium and utilize this mechanism to rapidly

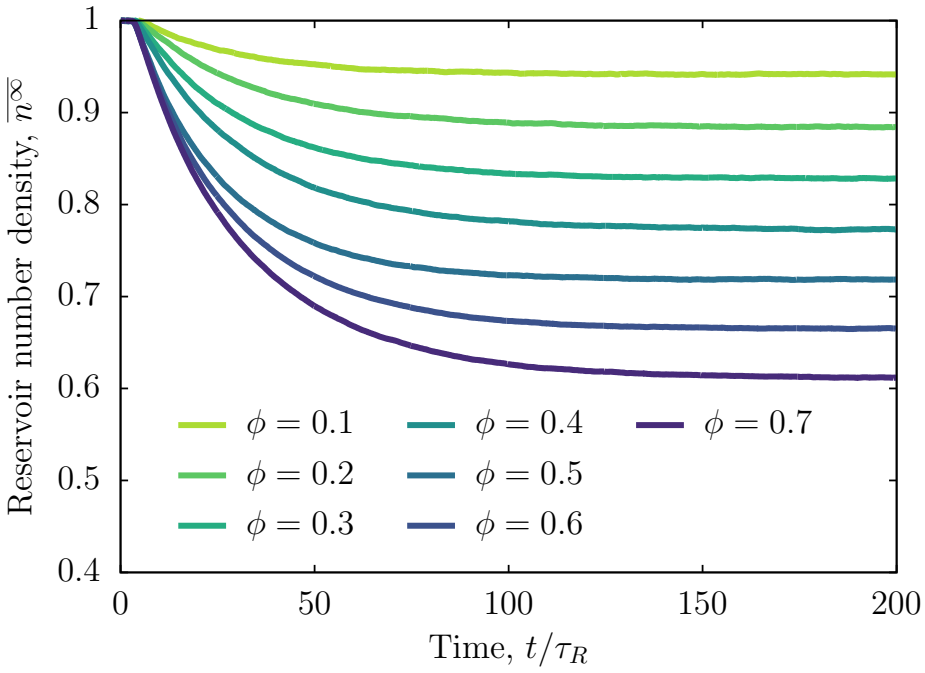

Figure 3.6: Number density in the reservoir, $\overline{n^\infty} = n^\infty/n^\infty(t = 0)$, as a function of time for $R/\ell = 0.5$, $k_s T_s/k_B T = 800$, and $\phi = 0.1 - 0.7$. We observe that the concentration decreases exponentially as particles diffuse out of the reservoir and reaches a steady state reservoir concentration after $\sim 100\tau_R$. This time corresponds to the characteristic time it would take a particle to explore the entire reservoir, $t_{char} \sim A_{res}/U_0^2\tau_R$, where A_{res} is the size of the reservoir.

drain out the bacteria. With the knowledge of the area fraction dependence, one could either drain an optimal amount or achieve the maximum drainage effect by having a high area fraction of obstacles in the porous medium. One could also separate a mixture of bacteria if they had different run lengths. In the next section, we predict the long-time partitioning between the porous medium and the fluid reservoir.

3.3 Partitioning into a porous medium

Two dimensions

Fig. 3.7 shows the average number density in the porous medium, $\langle n_{pore}\rangle/n^\infty$, as a function of the area fraction of obstacles, ϕ. Passive particles distribute homogeneously independent of the system geometry. However, when the particles are active, there is an increased concentration in the porous medium compared to the reservoir at steady state. The partitioning depends on the three nondimensional parameters:

ℓ/δ, ℓ/R, and ϕ. We can determine how the partitioning scales with these parameters, and analytically predict the partitioning from the governing Smoluchowski equation. First, we relate the average concentration in the porous medium $\langle n_{pore} \rangle$ to the one in the bulk pore space n^0_{pore}. For high activities, we can assume that the accumulation boundary layers are thin such that they do not overlap, and each obstacle can be viewed as isolated and surrounded by a concentration of n^0_{pore}. From the analytical expression for ABP accumulation outside a single disk, we integrate over all N obstacles within the porous medium to obtain

$$\frac{\langle n_{pore} \rangle}{n^0_{pore}} = 1 + \frac{2\pi N}{A_f} \int_R^\infty \left(\frac{n(r)}{n^0_{pore}} - 1 \right) r \, \mathrm{d}r, \tag{3.5}$$

where $n(r)$ is the concentration profile outside a single disk in two-dimensions. The area fraction of obstacles is $\phi = \pi R^2 N/A$. The free space area is $A_f = A(1-\phi)$. At high activity, the boundary layer is thin, and by subtracting the bulk concentration, we know that $n(r)/n^0_{pore} - 1$ will be confined to the accumulation layer, and we have

$$\int_R^\infty \left(\frac{n(r)}{n^0_{pore}} - 1 \right) r \, \mathrm{d}r \sim (\ell/\delta)^2 R/\lambda. \tag{3.6}$$

Thus, the average concentration in the porous medium relative to that in the pore space is

$$\frac{\langle n_{pore} \rangle}{n^0_{pore}} = 1 + C_{2D} \frac{\phi}{1-\phi}, \tag{3.7}$$

where C_{2D} is a numerical factor from the 2D disk solution of Yan & Brady [11]:

$$C_{2D} = \frac{4}{\lambda R} \frac{(\ell/\delta)^2 \mathrm{K}_1(\lambda R)}{\mathrm{K}_0(\lambda R)[2 - (\ell/\delta)^2] + \mathrm{K}_2(\lambda R)[2 + (\ell/\delta)^2]}, \tag{3.8}$$

where K_0 and K_2 are Bessel-functions. (See Appendix 3.5 for details on the Smoluchowski equation and statistical moments' expansion.) The analysis leading to (3.7) requires the accumulation layer to be thin, $\lambda R \gg 1$, and in the high activity limit, $\ell/\delta \gg 1$, C_{2D} is independent of the microscopic length δ and takes the simple form

$$C_{2D} = \frac{\sqrt{2}\, \ell/R}{1 + \frac{1}{\sqrt{2}} \ell/R}, \tag{3.9}$$

when $\delta/R \ll 1$ and $\ell/\delta \gg 1$. Thus, with (3.7) and (3.9), we have a relation between $\langle n_{pore} \rangle$ and n^0_{pore}. To determine the partitioning between the porous medium and the reservoir, we still need to relate the uniform concentration in the pore space, n^0_{pore}, to the reservoir concentration n^∞.

As in our previous work for parallel plates [25], we apply a momentum balance to the control volume shown in Fig. 3.1, which, as discussed in Appendix 3.6, yields

$$n^0_{pore} = n^\infty [1 + 2\overline{Q}^{pore}_{xx}]^{-1}, \tag{3.10}$$

where $\overline{Q}^{pore}_{xx}$ is the nematic order density in the pore space. Assuming the nematic order is negligible, (3.10) reduces to

$$n^0_{pore} = n^\infty, \tag{3.11}$$

where n^∞ is the bulk concentration in the reservoir and n^0_{pore} is the pore space concentration in the porous medium. The pore space concentration in the porous medium only accounts for ABPs outside a distance of 10 screening lengths of the obstacle surfaces. The screening length is the characteristic thickness of accumulation boundary layer, λ^{-1}, and the bulk area is shown in gray in the inset of Fig. 3.8. We validate (3.11) through BD simulations, and Fig. 3.8 shows n^0_{pore}/n^∞ as a function of the area fraction of obstacles. When the area fraction is near close packing, our thin boundary layer approximation no longer holds, and the boundary layers overlap. However, for our range of area fractions, we observe $n^0_{pore}/n^\infty = 1$ within a 90% margin. This deviation is due to the edge effects of the porous medium and the neglect of the nematic order term in (3.10). The nematic order is negative at the edge of the boundary layer.

The combination (3.7), (3.9), and (3.11) form the analytical prediction for the partitioning confirm that the partitioning in the porous medium scales linearly as $\phi/(1-\phi)$. Fig. 3.9 shows the excellent comparison between our analytical prediction and the results from BD simulation. From the partitioning we can also obtain the steady state drop in reservoir concentration from the overall conservation of particle number.

Three dimensions

We predict the partitioning between a lattice of spheres in contact with a fluid reservoir in three dimensions (shown in the inset of Fig. 3.10) using arguments analogous to that for the two-dimensional geometry. Fig. 3.10 shows the value of n^0_{pore}/n^∞ as a function of the volume fraction of obstacles. As before, the prediction for the partitioning is

$$\frac{\langle n_{pore} \rangle}{n^0_{pore}} = 1 + \frac{4\pi N}{V_f} \int_R^\infty \left[\frac{n(r)}{n^0_{pore}} - 1 \right] r^2 \, \mathrm{d}r. \tag{3.12}$$

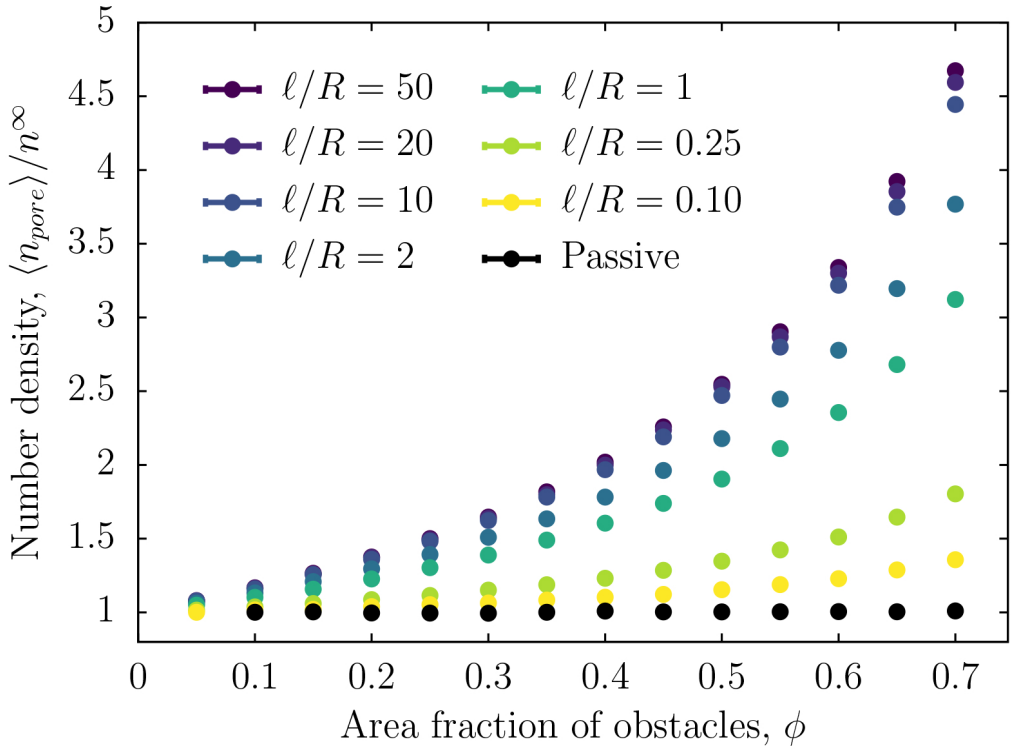

Figure 3.7: Average number density in the two-dimensional porous medium, $\langle n_{pore} \rangle / n^{\infty}$, as a function of the area fraction of obstacles, ϕ, for ratios of obstacle size to run length, $R/\ell \in [0.1, 50]$, at steady state with activity $k_s T_s \sim 5000 k_B T$.

In three dimensions, the volume fraction is $\phi = \frac{4}{3}\pi N R^3 / V$ and further reduced by $V_f = V(1-\phi)$. Equivalent to the two-dimensional case, we have

$$\frac{\langle n_{pore} \rangle}{n^0_{pore}} = 1 + C_{3D} \frac{\phi}{1-\phi}, \tag{3.13}$$

where C_{3D} is a numerical factor from the 3D sphere solution of Yan & Brady and is given by

$$C_{3D} = \frac{\frac{1}{2}(\ell/\delta)^2(\lambda R + 1)}{1 + (1+\lambda R)(\delta/R)^2} \frac{1}{(R\lambda)^2}. \tag{3.14}$$

As before, in the high activity limit where $\ell/\delta \gg 1$ and $\lambda R \gg 1$, the scaling factor becomes

$$C_{3D} = \frac{\frac{\sqrt{3}}{2}\frac{\ell}{R}}{1 + \frac{1}{\sqrt{3}}\frac{\ell}{R}}. \tag{3.15}$$

For high activity the scale factor depends only on the degree of confinement, ℓ/R. The combination of (3.13) and (3.14) with $n^0_{pore} = n^{\infty}$ gives the full analytical

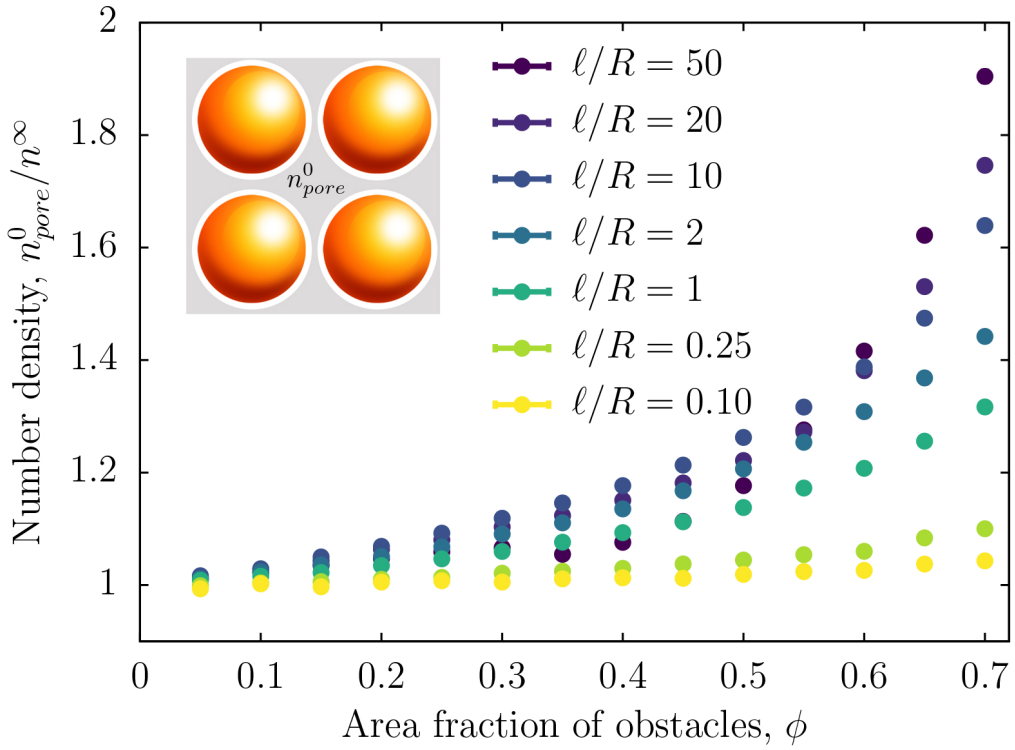

Figure 3.8: Average number density in the pore space of porous medium, n^0_{pore}, to that in the reservoir, n^∞ as a function of the area fraction of obstacles, ϕ, at steady state and $k_sT_s \sim 5000k_BT$. Inset shows the region (gray) for which n^0_{pore} is computed.

prediction of the partitioning between a reservoir and a porous medium in three dimensions and is compared to results from BD simulations in Fig. 3.11. Notice that having $k_sT_s \sim 250k_BT$ or $k_sT_s \sim 800k_BT$ leads to the same partitioning independent of the two activities when the degree of confinement, ℓ/R, is the same, thus validating (3.15). The scaling coefficient has the general form given in (3.1).

3.4 Conclusions

The transient evolution of the number density in porous media (i.e., two-dimensional arrays of circles) shows a fascinating initial oscillatory behavior. Through dimensional analysis, we argue that the behavior only depends on the activity, the degree of confinement (ratio of run length to obstacle size), and the area fraction of obstacles. We predict this behavior when the length scales in the medium are on the order of the particle run length. After the initial oscillations, the particles from the reservoir diffuse into the porous medium, which decreases the concentration in the reservoir,

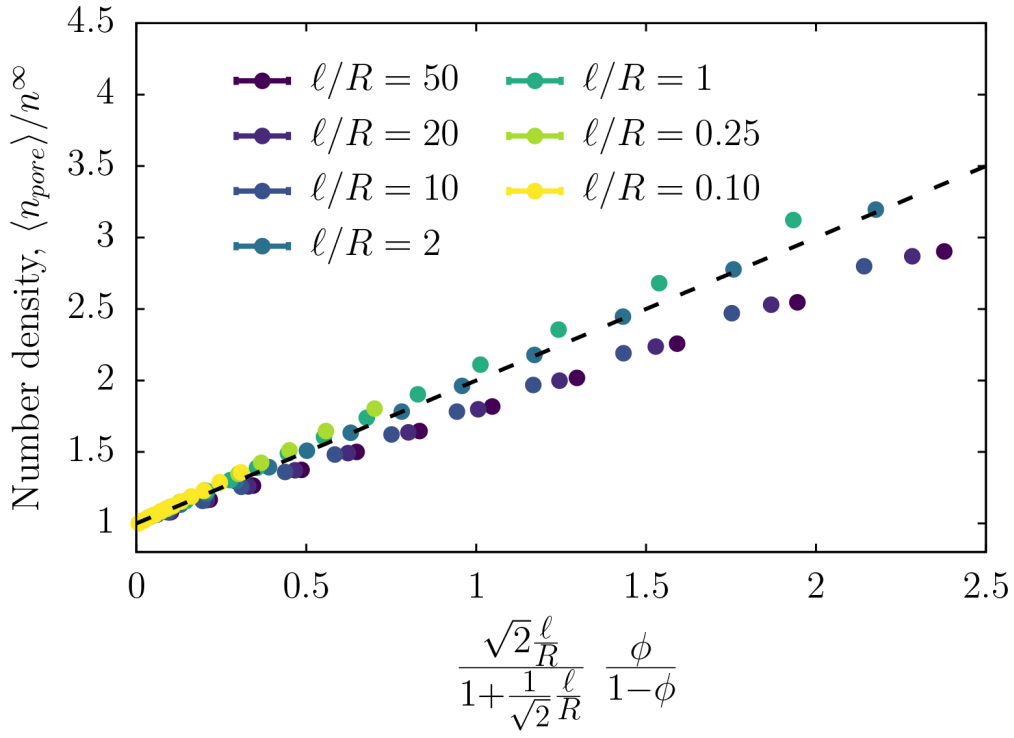

Figure 3.9: Relative number density in the porous medium, $\langle n_{pore}\rangle$, to that in the reservoir, n^{∞} as a function of a combination of degree of confinement, C_{2D}, and obstacle volume fraction $\phi/(1-\phi)$ leading to linear partitioning dependence at steady state in two dimensions and $k_s T_s \sim 5000 k_B T$. The dashed line show the analytical prediction in (3.7) combined with (3.11), where C_{2D} is given by (3.9).

while increasing the concentration in the porous medium, leading to a partitioning in concentration.

We presented a model for the concentration partitioning between a porous medium and external environments at steady-state, and predicted a linear dependence between the partitioning and a combination of degree of confinement and the area fraction of obstacles. The analytical prediction is determined by applying a mechanical momentum balance and utilizing the concentration profile outside a single disk/sphere (2D/3D). Our analytical prediction agrees well with results from Brownian dynamics simulation in both two and three dimensions. While the prediction is for a regular lattice porous medium, and many environments in nature are less structured, we expect that the general ideas and scaling should apply to disordered media. However, disordered media will create corners between obstacles, where active particles would get trapped leading to an increased partitioning. This work

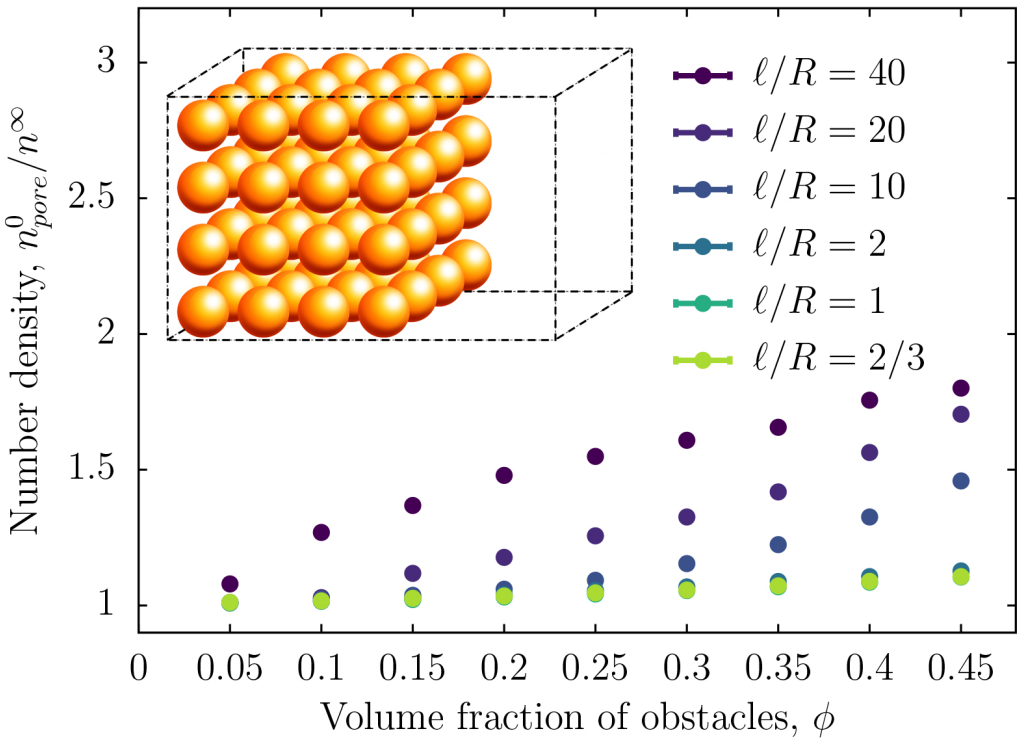

Figure 3.10: Average pore space number density in the porous medium, n^0_{pore}, to that in the reservoir, n^∞ as a function of the volume fraction of obstacles, ϕ, at steady state and $k_s T_s \sim 250 k_B T$. The inset illustrates the porous medium in three dimensions (i.e., spheres on a cubic lattice in contact with a fluid reservoir).

provides a foundation for understanding partitioning in more complex and confined environments. Additionally, our predictive model can be utilized for designing geometrical configurations of porous media that can capture a desired concentration of active particles.

3.5 Theoretical framework

This work depends on two methods for obtaining analytical predictions and results: conservation equations and Brownian dynamics simulations. The Smoluchowski equation governs the probability, P, for finding an active Brownian particle at a specific position $\boldsymbol{x}$ with orientation $\boldsymbol{q}$:

$$\frac{\partial P(\boldsymbol{x}, \boldsymbol{q}, t)}{\partial t} + \nabla \cdot \boldsymbol{j}^T + \nabla_R \cdot \boldsymbol{j}^R = 0, \tag{3.16}$$

where the translational and rotational fluxes are: $\boldsymbol{j}^T = U_0 \boldsymbol{q} P + \boldsymbol{F}^W P/\zeta - D_T \nabla P$ and $\boldsymbol{j}^R = -D_R \nabla_R P$. Here, $\nabla_R = \boldsymbol{q} \times \nabla_{\boldsymbol{q}}$ is the orientational gradient operator,

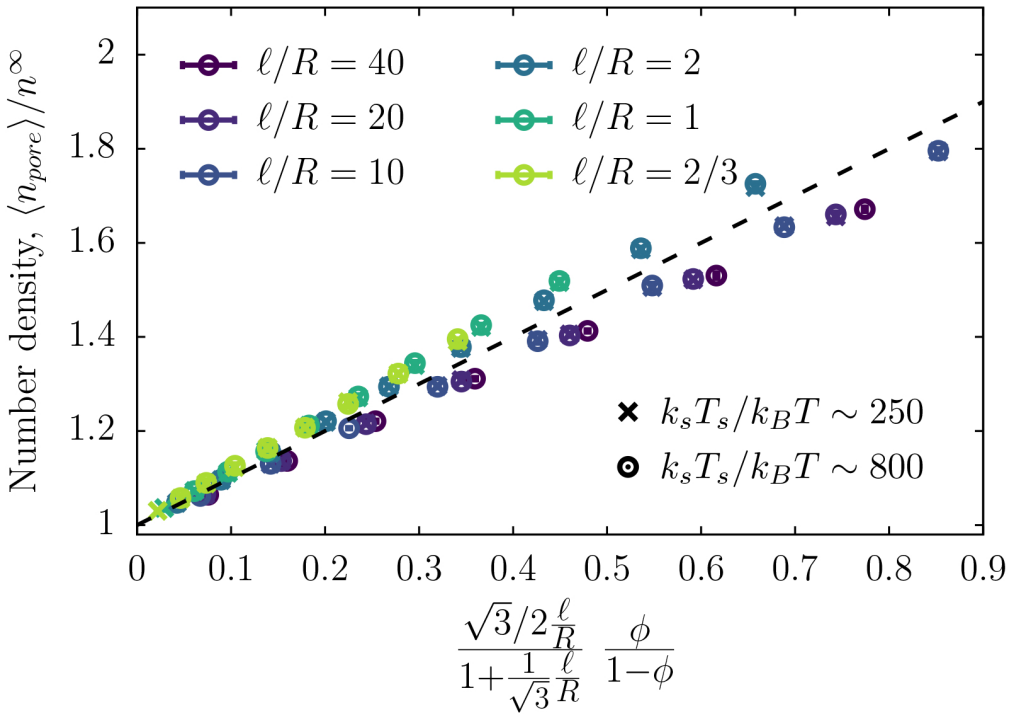

Figure 3.11: Relative number density in the porous medium, $\langle n_{pore}\rangle$, to that in the reservoir, n^{∞}, as a function of a combination of degree of confinement, C_{3D}, and obstacle volume fraction $\phi/(1-\phi)$ leading to linear partitioning dependence at steady state in three dimensions for $k_sT_s \sim 250k_BT$ and $k_sT_s \sim 800k_BT$. The dashed lines show the analytical prediction in (3.13), where C_{3D} is given by (3.15).

and D_T and D_R are the translational and rotational diffusivity, respectively. The number density is obtained by expanding the Smoluchowski equation in statistical moments [30], such that $n(\boldsymbol{x},t) = \int P(\boldsymbol{x},\boldsymbol{q},t)\mathrm{d}\boldsymbol{q}$, $\boldsymbol{m}(\boldsymbol{x},t) = \int \boldsymbol{q}P(\boldsymbol{x},\boldsymbol{q},t)\mathrm{d}\boldsymbol{q}$, which leads to the equations in 2D [30]:

$$\frac{\partial n}{\partial t} + \nabla\cdot\boldsymbol{j}_n = 0, \tag{3.17}$$

$$\frac{\partial \boldsymbol{m}}{\partial t} + \nabla\cdot\boldsymbol{j}_m + D_R\boldsymbol{m} = 0, \tag{3.18}$$

where the fluxes are given by

$$\boldsymbol{j}_n = U_0\boldsymbol{m} - D_T\nabla n, \tag{3.19}$$

$$\boldsymbol{j}_m = U_0\boldsymbol{Q} + \frac{1}{2}U_0 n\boldsymbol{I} - D_T\nabla m, \tag{3.20}$$

where n is the number density, $\boldsymbol{m}$ is the polar order, and $\boldsymbol{Q}(\boldsymbol{x},t) = \int(\boldsymbol{qq} - \boldsymbol{I}/2)P(\boldsymbol{x},\boldsymbol{q},t)\mathrm{d}\boldsymbol{q}$ is the nematic order. Assuming an isotropic nematic order, $\boldsymbol{Q} = 0$,

we can close the expansion. These equations can be solved for simple geometries to obtain analytical expressions for the concentration distribution. Yan & Brady solved these equations outside a disk in two-dimensions and a sphere in three-dimensions subject to no flux at $r = R$ [11]. Applying these analytical solutions of the Smoluchowki equations in combination with no net-force balances over specific control volumes in the porous medium (Appendix 3.6), we obtain analytical predictions for the behavior.

To verify the analytical predictions, we perform Brownian dynamic simulations. These simulations can be viewed as numerically solving the particles' equation of motion: The overdamped Langevin equations [30],

$$\mathbf{0} = -\zeta \boldsymbol{U} + \boldsymbol{F}^{Swim} + \boldsymbol{F}^{B}, \tag{3.21}$$

$$\mathbf{0} = -\zeta_R \boldsymbol{\Omega} + \boldsymbol{L}^{R}, \tag{3.22}$$

where $\boldsymbol{U}$ is the translational velocity, $\boldsymbol{\Omega}$ is the rotational velocity, ζ_R is the rotational Stokes drag, and $\boldsymbol{F}^{Swim}$ is the swim force defined to be $\boldsymbol{F}^{Swim} \equiv \zeta U_0 \boldsymbol{q}$. $\boldsymbol{F}^{B}$ is the random Brownian force with the properties $\overline{\boldsymbol{F}^{B}} = \mathbf{0}$ and $\overline{\boldsymbol{F}^{B}(0)\boldsymbol{F}^{B}(t)} = 2k_B T\zeta\delta(t)\boldsymbol{I}$, where $\boldsymbol{I}$ is the identity tensor and $\delta(t)$ is the delta-function. $\boldsymbol{L}^{R}$ is the random reorientation torque where $\overline{\boldsymbol{L}^{R}} = \mathbf{0}$ and $\overline{\boldsymbol{L}^{R}(0)\boldsymbol{L}^{R}(t)} = 2\zeta_R^2\delta(t)\boldsymbol{I}/\tau_R$. Length scales are non-dimensionalized by the microscopic length $\delta = \sqrt{D_T\tau_R}$ and the time steps are non-dimensionalized by the reorientation time, τ_R. The orientation of the translational motion $\boldsymbol{q}$ is related to the angular velocity $\boldsymbol{\Omega}$ via: $d\boldsymbol{q}/dt = \boldsymbol{\Omega} \times \boldsymbol{q}$. The particles interact with obstacles through a no flux condition, which is implemented via a potential-free algorithm [26–28] In order to obtain steady state and minimize the impact of fluctuations and errors, the simulations are computed with $\sim 10^6$ particles and a minimum of 10^4 τ_R. For the transient results, the simulations are computed with $\sim 10^7$ particles.

3.6 Momentum balance

From the macroscopic Langevin equations we can write the momentum balance

$$0 = -\zeta \boldsymbol{j}_n + \zeta U_0 \boldsymbol{m} + \nabla \cdot \boldsymbol{\sigma}^{osmo}, \tag{3.23}$$

where the flux is given by $\boldsymbol{j}_n \equiv n\frac{1}{N}\sum_{\alpha=1}^{N} \boldsymbol{U}_\alpha$, the polar order is $\boldsymbol{m} \equiv n\frac{1}{N}\sum_{\alpha=1}^{N} \boldsymbol{q}_\alpha$, and $\boldsymbol{\sigma}^{osmo} = -nk_BT\boldsymbol{I}$ is the osmotic pressure. In the force balance (3.23) $-\zeta \boldsymbol{j}_n$ is the average drag force from the suspending medium (which is assumed to be stationary), $\zeta U_0 \boldsymbol{m}$ is the average propulsive or swim force, and since the average of the Brownian force is zero, its effect appears as the divergence of a stress $\nabla \cdot \boldsymbol{\sigma}^{osmo}$.

The polar order can be written in terms of its flux as $\boldsymbol{m} = -\tau_R \nabla \cdot \boldsymbol{j}_m$, and the expression for polar order flux is given in (3.20). Thus, the momentum balance becomes

$$0 = -\zeta \boldsymbol{j}_n + \nabla \cdot [\boldsymbol{\sigma}^{osmo} - \zeta \ell \boldsymbol{j}_m]. \tag{3.24}$$

At steady state $\nabla \cdot \boldsymbol{j}_n$ can be written as $j_i^n = \dfrac{\partial}{\partial x_j} j_j^n x_i$; thus, the momentum balance becomes

$$\nabla \cdot [\boldsymbol{\sigma}^{osmo} - \zeta \ell \boldsymbol{j}_m - \zeta \boldsymbol{j}_n \boldsymbol{x}] = 0. \tag{3.25}$$

We apply this momentum balance to the control volume (C.V.) illustrated in Fig. 3.1:

$$0 = \oint \boldsymbol{n} \cdot [\boldsymbol{\sigma}^{osmo} - \zeta \ell \boldsymbol{j}_m - \zeta \boldsymbol{j}_n \boldsymbol{x}] dS, \tag{3.26}$$

where $\oint [...] dS$ designates the integral over all surfaces. Integrating the x-component gives

$$\begin{aligned} 0 = H[(-\sigma_{xx}^{osmo} + \zeta \ell j_{xx}^m + \zeta j_x^n x)|_L \\ + (\sigma_{xx}^{osmo} - \zeta \ell j_{xx}^m - \zeta j_x^n x)|_R] + \sum_P \oint \boldsymbol{n} \cdot \boldsymbol{\sigma}^{osmo} dS \cdot \mathbf{1}_x, \end{aligned} \tag{3.27}$$

where subscripts L and R refer to the left and right boundary of $C.V.$, and $\sum_P \oint [...] dS$ is the integral over all obstacles in $C.V.$. For the left and right boundary, we have

$$\begin{aligned} (-\sigma_{xx}^{osmo} + \zeta \ell j_{xx}^m + \zeta j_x^n x)|_L = \\ n_{pore}^0 (k_B T + k_s T_s) + 2 k_s T_s Q_{xx}^{pore}, \end{aligned} \tag{3.28}$$

$$(\sigma_{xx}^{osmo} - \zeta \ell j_{xx}^m - \zeta j_x^n x)|_R = -n^\infty (k_B T + k_s T_s), \tag{3.29}$$

where $k_s T_s = \zeta \ell U_0 / d(d-1)$. Note that the particle flux j_n^x is zero at both boundaries, thus the momentum balance in (3.27) becomes

$$\begin{aligned} (k_B T + k_s T_s)(n_{pore}^0 - n^\infty) + 2 k_s T_s Q_{xx}^{pore} = \\ \frac{1}{H} \sum_P \oint n k_B T \boldsymbol{n} dS \cdot \mathbf{1}_x. \end{aligned} \tag{3.30}$$

For all particles fully inside the porous medium, we know that $\int n k_B T \boldsymbol{n} dS = 0$. Even for the particles at the edge, this could be at most proportional to $n_{pore}^0 - n^\infty$. Therefore, we have that

$$\int n k_B T \boldsymbol{n} dS \cdot \mathbf{1}_x = \alpha (n_{pore}^0 - n^\infty) k_s T_s \pi R, \tag{3.31}$$

where R is the obstacle radius and α is an unknown scaling coefficient. The contribution from the edge will depend on the number of particles at the edge within the control volume, which is $N_{edge} = H/L$, where H is the height of the control volume and L is the length of a unit cell. Thus, the momentum balance becomes

$$(k_BT + k_sT_s)\left[1 + \alpha\frac{\pi R}{L}\right](n^0_{pore} - n^\infty) + 2k_sT_sQ^{pore}_{xx} = 0. \tag{3.32}$$

In the porous medium, the nematic order can be written as $Q^{pore}_{xx} = n_{pore}\overline{Q}^{pore}_{xx}$, such that

$$\left[(k_BT + k_sT_s)\left[1 + \alpha\frac{\pi R}{L}\right] + 2k_sT_s\overline{Q}^{pore}_{xx}\right]n^0_{pore} = (k_BT + k_sT_s)\left[1 + \alpha\frac{\pi R}{L}\right]n^\infty. \tag{3.33}$$

Or,

$$n^0_{pore} = n^\infty\left[1 + \frac{2k_sT_s\overline{Q}^{pore}_{xx}}{(k_BT + k_sT_s)(1 + \alpha\frac{\pi R}{L})}\right]^{-1} \tag{3.34}$$

From Yan & Brady [11] we know that $\overline{Q}_{xx} < 0$ away from the obstacle surface. Hence, $n^0_{pore} > n^\infty$ and becomes increasingly so the higher the area fraction ϕ. Assuming the edge effects are negligible α must be small, and the expression becomes

$$n^0_{pore} = n^\infty\left[1 + \frac{2\overline{Q}^{pore}_{xx}}{1 + k_BT/k_sT_s}\right]^{-1}, \tag{3.35}$$

which for high activity ($k_sT_s \gg k_BT$) is the expression in (3.10).

References

[1] E. Lauga and T. R. Powers, "The hydrodynamics of swimming microorganisms", Reports on Progress in Physics **72**, 096601 (2009).

[2] S. Granick, S. Jiang, and Q. Chen, "Janus particles", Physics Today **62**, 68–69 (2009).

[3] F. Wurm and A. F. M. Kilbinger, "Polymeric Janus particles", Angewandte Chemie-international Edition **48**, 8412–8421 (2009).

[4] S. C. Takatori and J. F. Brady, "Forces, stresses and the (thermo?) dynamics of active matter", Current Opinion in Colloid and Interface Science **21**, 24–33 (2016).

[5] S. A. Mallory, C. Valeriani, and A. Cacciuto, "An active approach to colloidal self-assembly", Annual Review of Physical Chemistry **69**, 59–79 (2018).

[6] C. Maggi, J. Simmchen, F. Saglimbeni, J. Katuri, M. Dipalo, F. De Angelis, S. Sanchez, and R. Di Leonardo, "Self-assembly of micromachining systems powered by Janus micromotors", Small **12**, 446–451 (2016).

[7] C. Bechinger, R. Di Leonardo, H. Löwen, C. Reichhardt, G. Volpe, and G. Volpe, "Active particles in complex and crowded environments", Reviews of Modern Physics **88**, 045006 (2016).

[8] W. Gao, R. Dong, S. Thamphiwatana, J. Li, W. Gao, L. Zhang, and J. Wang, "Artificial micromotors in the mouse's stomach: a step toward in vivo use of...", ACS nano **9**, 117–123 (2014).

[9] R. Di Giacomo, S. Krödel, B. Maresca, P. Benzoni, R. Rusconi, R. Stocker, and C. Daraio, "Deployable micro-traps to sequester motile bacteria", Scientific Reports **7**, 1–8 (2017).

[10] D. A. Beard and T. Schlick, "Unbiased rotational moves for rigid-body dynamics", Biophysical Journal **85**, 2973–2976 (2003).

[11] W. Yan and J. F. Brady, "The force on a boundary in active matter", Journal of Fluid Mechanics **785**, R1 (2015).

[12] W. Yan and J. F. Brady, "The curved kinetic boundary layer of active matter", Soft Matter **14**, 279–290 (2018).

[13] S. C. Takatori, R. De Dier, J. Vermant, and J. F. Brady, "Acoustic trapping of active matter", Nature Communications **7**, 10694 (2016).

[14] R. Alonso-Matilla, B. Chakrabarti, and D. Saintillan, "Transport and dispersion of active particles in periodic porous media", Physical Review Fluids **4**, 1–21 (2019).

[15] M. Brun-Cosme-Bruny, E. Bertin, B. Coasne, P. Peyla, and S. Rafaï, "Effective diffusivity of microswimmers in a crowded environment", Journal of Chemical Physics **150**, 104901 (2019).

[16] A. Dehkharghani, N. Waisbord, J. Dunkel, and J. S. Guasto, "Bacterial scattering in microfluidic crystal flows reveals giant active taylor–aris dispersion", Proceedings of the National Academy of Sciences of the United States of America **166**, 11119–11124 (2019).

[17] Sujit S. Datta, "Confinement and activity regulate bacterial motion in porous media", Soft Matter **64**, 6545–6563 (2019).

[18] A. Chamolly, T. Ishikawa, and E. Lauga, "Active particles in periodic lattices", New Journal of Physics **19**, 115001 (2017).

[19] T. Bhattacharjee, D. B. Amchin, J. A. Ott, F. Kratz, and S. S. Datta, "Chemotactic migration of bacteria in porous media", Biophysical Journal **120**, 3483–3497 (2021).

[20] C. Reichhardt and C. J. Reichhardt, "Directional locking effects for active matter particles coupled to a periodic substrate", Physical Review E **102**, 042616 (2020).

[21] C. Reichhardt and C. J. Reichhardt, "Clogging, dynamics, and reentrant fluid for active matter on periodic substrates", Physical Review E **103**, 062603 (2021).

[22] C. Reichhardt and C. J. Reichhardt, "Active matter commensuration and frustration effects on periodic substrates", Physical Review E **103**, 022602 (2021).

[23] W. Henry, "III. Experiments on the quantity of gases absorbed by water, at different temperatures, and under different pressures", Philosophical Transactions of the Royal Society of London **93**, 29–274 (1803).

[24] R. M. Rosenberg and W. L. Peticolas, "Henry ' s Law : A Retrospective", Journal of Chemical Education **81**, 1647–1652 (2004).

[25] C. M. Kjeldbjerg and J. F. Brady, "Theory for the casimir effect and the partitioning of active matter", Soft Matter **17**, DOI: 10.1039/d0sm01797c, 523–530 (2021),

[26] D. M. Heyes and J. R. Melrose, "Brownian dynamics simulations of model hard-sphere suspensions", Journal of Non-Newtonian Fluid Mechanics **46**, 1–28 (1993).

[27] W. Schaertl and H. Sillescu, "Brownian dynamics simulations of colloidal hard spheres. Effects of sample dimensionality on self-diffusion", Journal of Statistical Physics **74**, 687–703 (1994).

[28] D. R. Foss and J. F. Brady, "Brownian dynamics simulation of hard-sphere colloidal dispersions", Journal of Rheology **44**, 629–651 (2000).

[29] A. R. Dulaney and J. F. Brady, "Waves in active matter: the transition from ballistic to diffusive behavior", Physical Review E **101**, 052609 (2020).

[30] D. Saintillan and M. J. Shelley, “Theory of active suspensions”, in *Complex Fluids in Biological Systems*, edited by S. E. Spagnolie (Springer, 2015) Chap. 9, pp. 319–355.

Chapter 4

HINDERED DIFFUSION OF ACTIVE PARTICLES IN POROUS MEDIA

Understanding the diffusion of active particles in confined environments is essential to utilize and enhance nature's own sustainable processes, e.g., improving bioremediation and optimizing bacteria transport in soil. The hindered diffusivity of passive Brownian particles in porous media depends only on the porosity or solids volume fraction. Contrastingly, active particles' effective diffusivity is also sensitive to the interplay between their run, or persistence, length and the media's pore size. This work investigates the transport behavior of active Brownian particles (ABPs) in a porous medium, where the porosity is achieved by having arrays of obstacles. We find that ABPs' effective diffusivity exhibits a complex non-monotonic behavior with increasing obstacle size for a fixed volume fraction. The behavior relates to three governing parameters; the activity, the area fraction of obstacles, and the degree of confinement (ratio of run length to obstacle size). We explore three regions of different behaviors: weak, medium, and strong confinement. Insight into this complex diffusive behavior will be crucial for optimal deployment of active particles in crowded environments, where it is essential to know how particles diffuse.

4.1 Introduction

The transport of active matter, such as bacteria, in porous media is an important problem in a variety of scientific and technological areas such as the spreading of contaminants in soils and groundwater aquifers, bacterial filtering, biodegradation and bioremediation processes, and the transport of motile cells inside the body [1]. Applications in medical diagnostics and biochemical analysis often hinge upon the manipulation and control of active particle motions through complex and crowded geometries [2, 3].

The diffusivity of active particles is larger than for passive particles, and both solid boundaries and other obstacles change the area available for swimming. Boundaries dramatically obstruct particle motion and shorten the mean free path for the particles. These obstructions lead to particles accumulating at boundaries and diffusivity decreasing [4, 5]. The effective diffusivity of passive particles in crowded environments is non-trivial, and their diffusivity decreases dependent on the area fraction of the obstacles *only* [6–8]. Alonso-Matilla et al. studied Taylor dispersion of active particles in circular arrays [9]. Even without flow, they observed a decrease in diffusivity for low activity particles resembling the behavior observed for passive particles. However, the no-flow case has exciting behaviors that need further exploration. Experimental studies of *Chlamydomonas Reinhardtii* show that the diffusion of bacteria is reduced compared to free space when placed around arrays of pillars [10]. However, there is a lack of knowledge regarding the transport of active particles in porous media at high activity.

The simplest model that captures the physics is the active Brownian particle (ABP) model. ABPs swim with speed U_0 in a direction $\boldsymbol{q}$ for a reorientation time τ_R; the average length they move between reorientations is called the run, or persistence, length $\ell = U_0\tau_R$ [11]. This run length leads to active particles having an effective size much larger than the actual size. Thus, these particles will exhibit effects of geometric confinement on larger scales than passive particles would [4, 5, 12–14]. The persistent motion creates a random walk to which can be assigned a translational diffusivity. This diffusivity is the sum of its thermal diffusivity, $D^T = k_BT/\zeta$ and the swim diffusivity, $D^{swim} = k_sT_s$. Here k_sT_s is the active energy scale analogous to the thermal energy scale k_BT. Further, the particles reorient and therefore have an associated rotational diffusivity, $D_R = 1/\tau_R$. The diffusive step sizes then become $\delta = \sqrt{D_T/D_R}$. The ratio of the run length to this microscopic length gives a measure

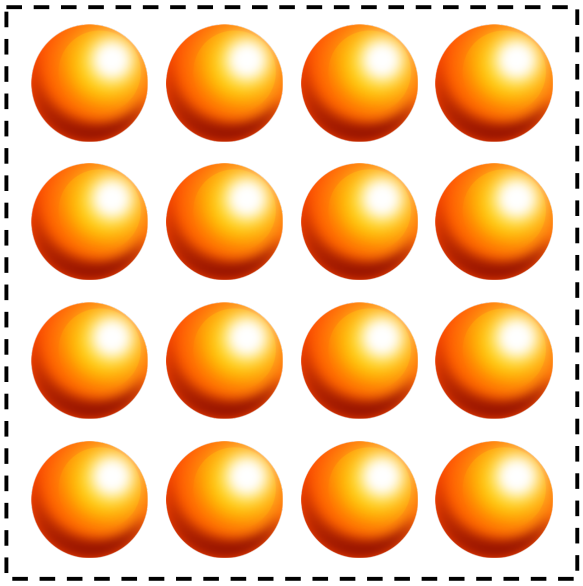

Figure 4.1: Illustration of the two-dimensional porous medium (i.e. disks on an equally spaced lattice). The active particles move around between the obstacles, and experience excluded volume interactions with the solid obstacle boundaries.

of the activity (the active energy compared to the thermal one): $k_s T_s / k_B T = (\ell/\delta)^2/2$ in two dimensions.

This work explores how the active particles diffuse in a periodic system with arrays of circular obstacles, and the system is displayed in Fig 4.1. We show that diffusion depends not only on the obstacle area fraction, but also on the activity and degree of confinement (ratio of run length to size of the obstacles). We observe interesting non-monotonic changes in diffusion as a function of the degree of confinement (i.e., the ratio of the particle run length to obstacle radius). These behaviors fall within three regions that depend on the size of the run length compared to the other geometric length scales. One limit where the run length is much smaller than all other length scales, one where it is much larger, and the intermediate where the run length is similar to other length scales in the system. The exploration of behaviors in these three regions provides a means to understanding diffusive transport for different activity levels and in a range of environments.

4.2 Diffusive transport

In order to understand how active particles diffuse and distribute in complex environments, we investigate their behavior in a model system. We focus on the particles'

behavior in the porous medium in terms of dynamic properties such as diffusivity only. In this work, the porous medium is a two-dimensional lattice of disks, and their separation is regulated through the area fraction of obstacles, ϕ. Fig. 4.1 shows this geometric system, where the orange disks are obstacles, and the dilute active particles can freely swim around the obstacles but not pass through them.

ABPs accumulate at no-flux surfaces due to their persistent motion, and when a particle collides with a wall, it keeps moving in the same orientation until it reorients. This accumulation leads to an increase in concentration in a boundary layer around the surface, which has been described and determined analytically by Yan et al. [4]. As long as the accumulation boundary layers around the obstacles do not overlap, we can expect the distribution in this porous media to be the same as outside a single sphere in a reservoir. Our previous work [15] describes the particle distribution and a model for the partitioning in this porous media connected to a reservoir.

The accumulation arises due to the porous medium obstructing the run length of the active particles significantly. Thus, the active particle diffusivity in the porous media is hindered, and therefore lower than it would be in free space. Bhattacharjee et al. [16] explored the impact on *E. coli*'s diffusivity in a porous medium experimentally. Furthermore, as earlier mentioned, Alonso-Matilla et al. did numerical studies for geometries similar to the one shown in Fig. 4.1 for active particles with low activity [9]. However, in this work, we focus on the behavior of active particles with high activity, such that the active energy scale is much larger than the thermal energy, $k_s T_s \gg k_B T$.

Passive particles in a porous medium will experience a decrease in diffusivity compared to free space as well. This decrease will be a function of the area fraction of obstacles *only*. Thus, the size of the obstacles compared to the passive particle size will not influence the effective diffusivity if the area fraction is the same. For active particles, the run length – or effective size – of the particles causes the particles to experience confinement at larger length scales than the passive ones would [17].

The diffusion will be influenced not only by the area fraction of obstacles, but also the properties of the active particles. From dimensional analysis, we find that the behavior must be governed by three dimensionless parameters; the size of the active step compared to the diffusive one, ℓ/δ, the ratio of the run length to the obstacle size, ℓ/R, and lastly the area fraction of obstacles, ϕ. All three parameters influence the mean free path the particles experience. We define the degree of confinement

as ℓ/R, where ℓ is the particle run length and R is the radius of an obstacle. We designate the effective, or hindered, diffusivity in the porous medium D^{eff}, and D^0 is the diffusivity in free space. For passive particles, the free space diffusivity is just the thermal diffusivity, $D^0 = k_B T/\zeta$, where ζ is the hydrodynamic drag coefficient. For active particles, the free space diffusivity is the sum of the thermal and swim diffusivity, $D^0 = D^T + D^{swim} = (k_B T + k_s T_s)/\zeta$.

We study the diffusive transport behavior of ABPs through Brownian Dynamics (BD) simulations. In the BD simulations, when a particle collides with an obstacle, it will keep exerting a force in its orientation until it reorients. We use a potential-free algorithm [18–20] to resolve the obstacle collisions. This algorithm places a particle that overlaps with an obstacle back to the point of contact by following along the obstacle surface normal vector until the system is free of overlaps. (See Appendix 4.5 for a description of the BD simulations.)

Fig. 4.2 illustrates the impact of degree of confinement on the diffusivity determined from measuring mean square displacement in the BD simulations for ABPs with high activity, $k_s T_s/k_B T = 800$. As expected, the diffusivity decreases when the area fraction of obstacles increases due to less space for ABPs to swim their full run length. Surprisingly, the effective diffusivity changes non-monotonically for an increasing degree of confinement, and this trend becomes more significant for higher area fractions of obstacles. This is different from particles with low activity, where Saintillan et al. observed that the diffusivity decrease is similar to passive particles [9]. At a constant area fraction of obstacles, if the average mean free path available per run length decreases, the active particle experiences a higher confinement. The mean free path is related to the diagonal distance between obstacles, $D^{between} = (\sqrt{2\pi/\phi} - 2)R$, and also the length of a unit cell, L. (The inset of Fig. 4.3 shows the geometric length scales within the porous media.) Thus, one would assume that the effective diffusivity decreases with increasing degree of confinement. However, we observe that this is only true when the degree of confinements are large. The opposite trend occurs when the run length is smaller than the obstacle size. We anticipate that this is because particles leaving the surface of an obstacle are less likely to collide with another obstacle in its first step. The different diffusive behaviors shown in Fig. 4.2 can be separated into the limiting behaviors in three regions of different effective confinement. Weak confinement where the run length is smaller than any other system length scale. Medium confinement where the run length is similar to other length scales in the porous media. Lastly, highly confined particle where the run length is much larger than the geometric lengths in the porous

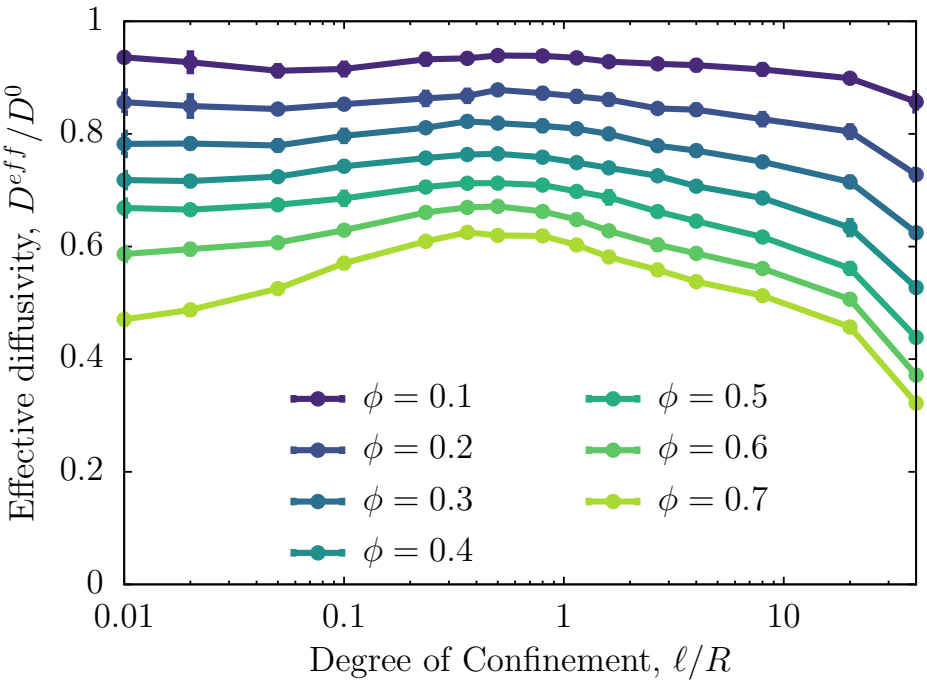

Figure 4.2: The ratio of the effective diffusivity, D^{eff}, to that in free space, D^0, as a function of the degree of confinement, ℓ/R. The results are from Brownian dynamics simulation with $k_sT_s = 800k_BT$ and the area fraction of obstacles between 0.1 and 0.7.

media. Each of these regions is covered in detail individually in the following sections.

4.3 Limiting behaviors

The fundamental rule of active matter

In simple active matter systems, it has been observed that when the run length is smaller than all other geometric lengths, the system behaves similarly to a passive system. An example of this is a single wall in a bath of active particles, where the pressure on the wall in a thermal system is the osmotic pressure. In an active system, the wall pressure is the sum of the contribution from thermal motion and from the swim pressure. [4] This is a fundamental rule of active matter that one can replace the thermal energy k_BT with the sum of the thermal energy and the active energy scale $k_BT + k_sT_s$.

Here, we show that this fundamental rule also applies to the hindered diffusivity of active particles in porous media. The inset of Fig. 4.3 shows the geometric

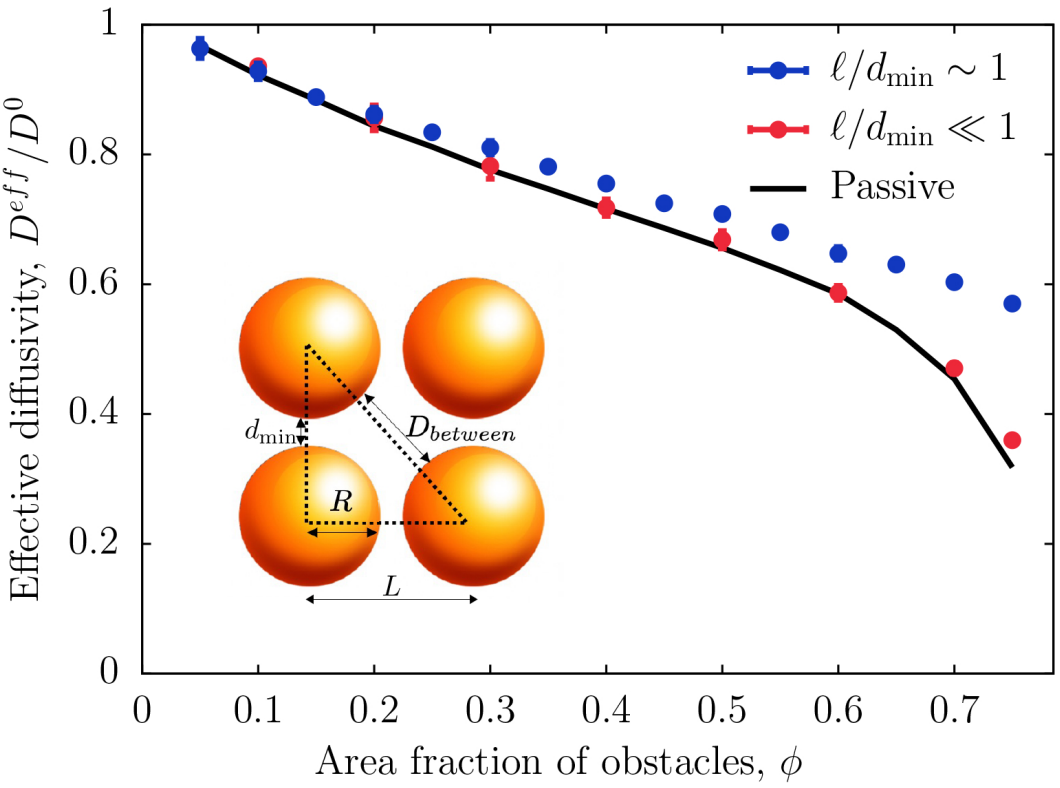

Figure 4.3: Ratio of effective diffusivity, D^{eff} to the free space diffusivity, D^0, as a function of area fraction of obstacles, ϕ. Results are for BD simulations with $k_sT_s/k_BT = 800$, and for $R/\ell = 5$ (blue) and $R/\ell = 100$ (red) for $d_{\min} \sim \ell$ and $d_{\min} \ll \ell$, respectively. The inset shows the length scales within the porous media.

length scales within the porous media. In this limit, the run length, ℓ, must be smaller than the smallest length, $d_{\min}$. For this to occur even with high activity, the obstacle sizes must be much larger than the run length. We obtain $l/d \gg 1$ when $R/\ell = 100$, and the result is shown in Fig. 4.3. The behavior is exactly the same as for passive particles, simply replacing the k_BT in the diffusion term by the summation of active and thermal energy, $k_BT + k_sT_s$. Thus, we show that the fundamental rule of length scales in active matter applies to more complex systems such as porous media. Further, when we depart from very weak confinement into medium confinement, where $\ell \sim d$, the behavior changes significantly. Especially as the obstacle area fraction gets near close packing, $\phi^{max} = \pi/4$, and the diffusion in this region is described in detail in the next section.

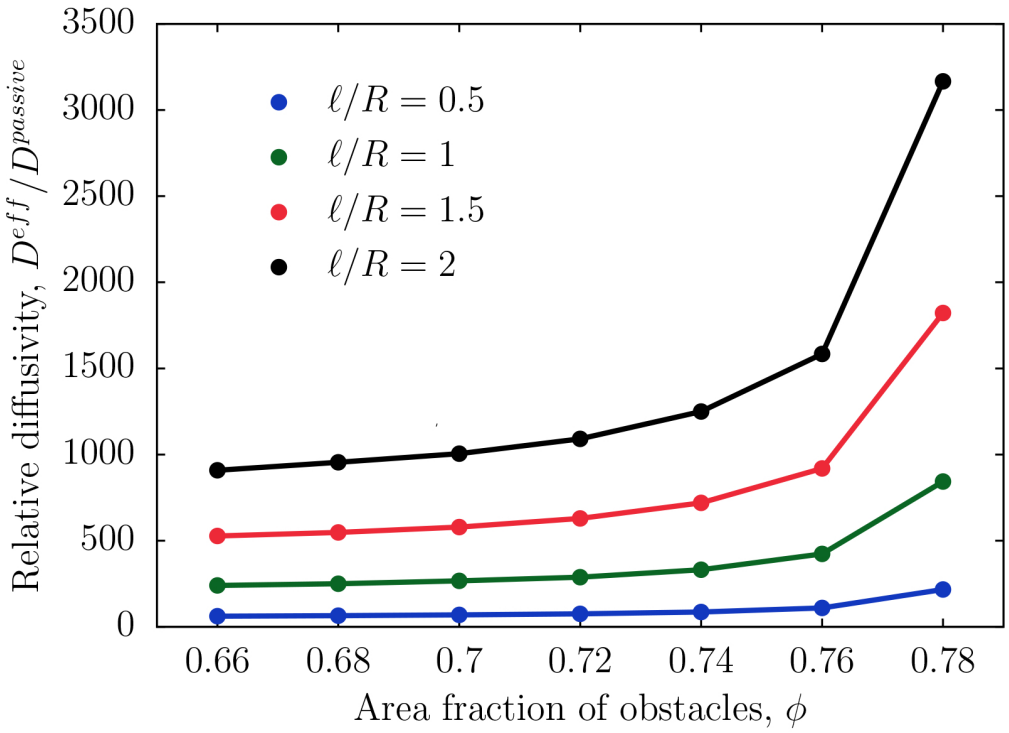

Figure 4.4: The ratio of effective diffusivity, D^{eff}, to that of passive particles, $D^{passive}$, as a function of area fraction of obstacles, ϕ, near close packing. The results are for fixed ratio of obstacle size to the diffusive step size, $R/\delta = 20$.

Near close packing

The diffusive behavior of active particles is radically different when the run length is comparable to the systems' geometric length scales. We observe in Fig 4.3 that the effective diffusivity linearly approaches a constant value rather than going towards zero as the area fraction of obstacles approaches close lattice packing. The behavior is very similar to passive particles for a low area fraction of obstacles. Therefore, we focus on the remarkable change in behavior for active compared to passive particles near close lattice packing, $\phi = \pi/4$, in 2-dimensions through BD simulations. Fig. 4.4 shows the ratio of the active particle diffusivity to the passive particle diffusivity. It is apparent that near the maximum packing fraction, the diffusivity can become more than 3000 times higher for active particles with an activity of $k_s T_s = 800 k_B T$.

We have seen in previous work [17] how changing the degree of confinement can change the behavior of the system drastically. The ratio of the active diffusivity to the passive one can be further normalized by what the ratio would be in free space, where $D^{eff}/D^{passive} = 1 + (\ell/\delta)^2/2$ in two dimensions. Thus, we show in Fig. 4.5

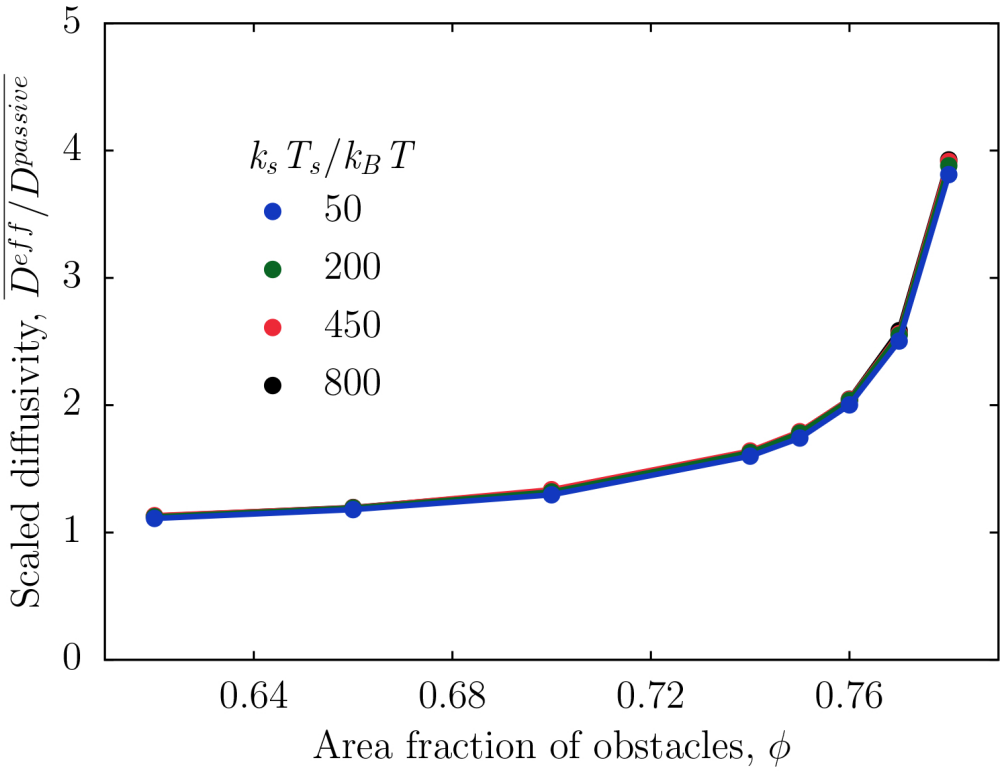

Figure 4.5: Ratio of effective diffusivity to thermal diffusivity as a function of area fraction near close packing scaled by the ratio in free space, where $D^{eff}/D^{passive} = 1 + (\ell/\delta)^2/2$ in two dimensions. Results are for fixed degree of confinement with $\ell/R = 1$, and we see that all the curves collapse perfectly onto one single curve when ℓ/R is fixed.

that when fixing the degree of confinement to be $\ell/R = 1$ and varying the activity, k_sT_s/k_BT, all the curves collapse perfectly for different activities. If the activity were to decrease further than $k_sT_s = 50$, we would expect that the normalized diffusivity will deviate from the master curve and decrease towards one instead.

Effective size as the largest length scale

The effect of confinement will be the strongest when the particle run length is the largest length scale. In this region, the run length will often be reduced due to collisions with obstacles. Therefore, we will also observe the largest decrease in effective diffusivity, especially as the system approaches close packing. Our results from BD simulations are shown in Fig. 4.6. Note that these results are for $R \sim \delta$, and this could impact the effective diffusivity we observe. Later, we show the results without thermal translational motion, $D_T = 0$, such that the system is now governed

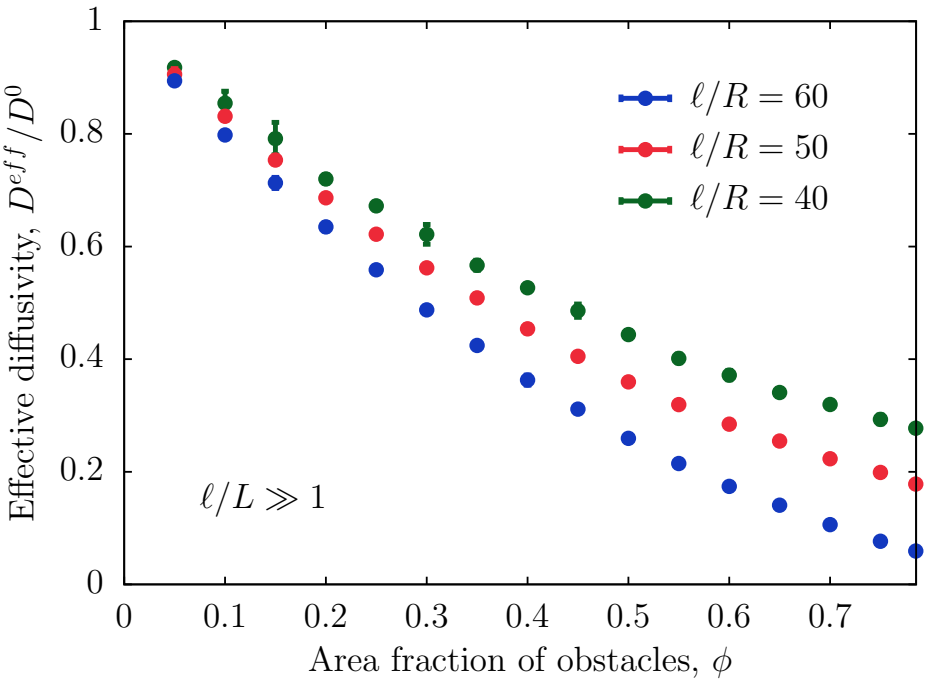

Figure 4.6: Effective diffusivity as a function of area fraction of obstacles, ϕ, in the limit where the run length is much longer than any other length scale in the system, $\ell \ll L$. The results are based on BD simulations with $R/\delta = 1$ and varying run length such that $k_s T_s / k_B T = 800$, 1250, and 1800.

by the degree of confinement and area fraction of obstacles only.

We observe that all diffusivity reaches a non-zero value at close packing, $\phi^{\max}$, and the specific values depend on the degree of confinement, ℓ/R. However, all the curves portray a similar decrease with an increasing area fraction of obstacles. Therefore, we choose an appropriate scaling for the diffusivity, as shown in Figure 4.7. All the curves collapse into one with this scaling, and the scaled diffusivity becomes one both as packing fraction goes to zero and at the maximum packing fraction. This scaling means that for any parameter set, we only need to know that the effective diffusivity at one area fraction within the range to predict the rest of the effective diffusivity for all ϕ,

$$\frac{D(\phi) - D(\phi_{\max})}{D(\phi = 0) - D(\phi_{\max})} = F(\phi), \tag{4.1}$$

where $F(\phi)$ is the functional form of the scaling collapse. In this expression, we know the diffusivity at zero area fraction is the free space diffusivity, $D(\phi = 0) = D^0$. Further, if we know the function form of $F(\phi)$ and the non-scaled diffusivity at one

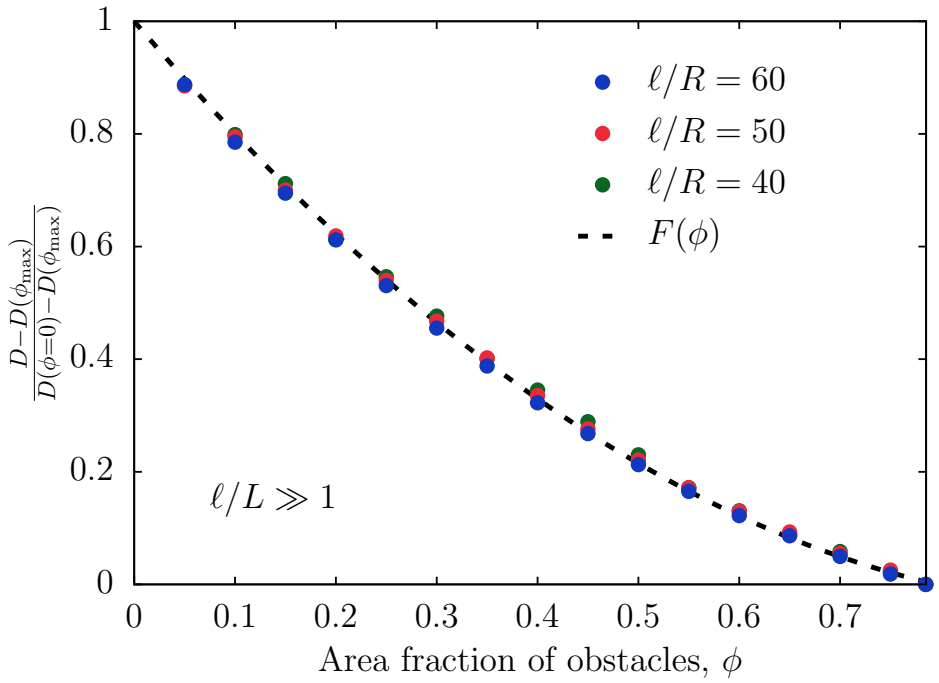

Figure 4.7: Scaled diffusivity, $(D - D(\phi_{\max}))/(D(\phi = 0) - D(\phi_{\max}))$ as a function of the area fraction of obstacles, ϕ. This scaled diffusivity will go to one as $\phi \to 0$, and similarly the diffusivity will always be zero as $\phi \to \phi^{max}$. We see that all the diffusivities collapse independent of activity with this scaling. This confirms that they all show exactly the same decreasing trend with increase in area fraction of obstacles. $F(\phi)$ is a polynomial regression, where $F(\phi) = 1.06 \cdot \phi^2 - 2.10 \cdot \phi + 1$. The results are based on BD simulations with $R/\delta = 1$ and varying run length such that $k_s T_s / k_B T = 800$, 1250, and 1800.

area fraction, ϕ_1, we can compute what we would expect the diffusivity at maximum packing to be

$$D(\phi_{\max}) = \frac{D(\phi_1) - F(\phi_1)D^0}{1 - F(\phi_1)}. \tag{4.2}$$

With the expression for the diffusivity at close packing, we can then find the diffusivity for all area fractions through,

$$D(\phi) = F(\phi)(D^0 - D(\phi_{\max})) + D(\phi_{\max}). \tag{4.3}$$

From Fig. 4.6, we can fit the data to a second order polynomial. Thereby, we obtain the expression for $F(\phi)$.

$$F(\phi) = 1.06 \cdot \phi^2 - 2.10 \cdot \phi + 1. \tag{4.4}$$

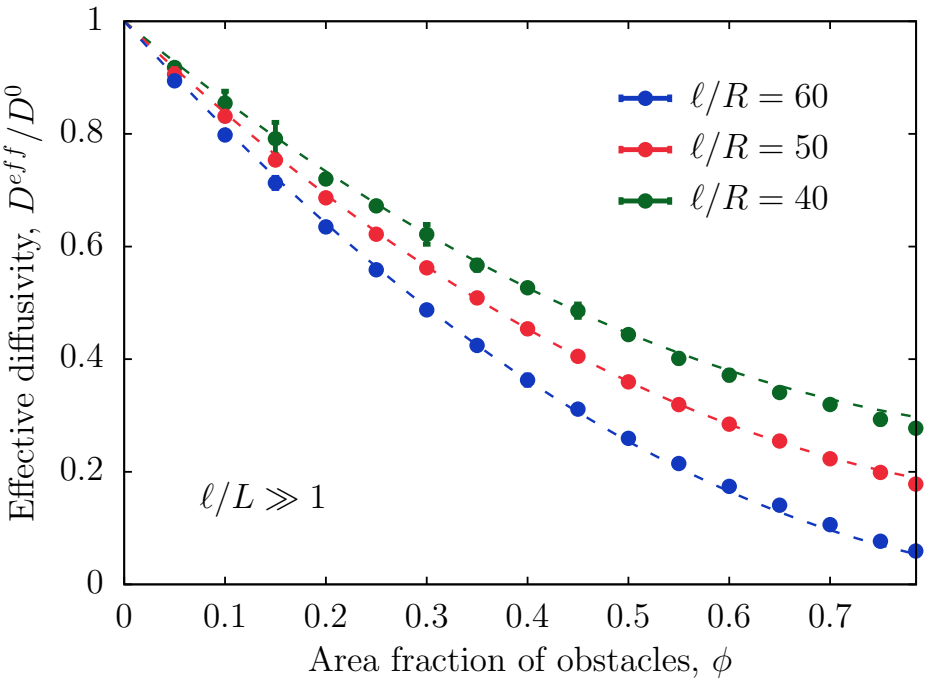

Figure 4.8: Effective diffusivity as a function of area fraction of obstacles. The dashed lines show the prediction when combining (4.2) and (4.3) with the BD results for a single area fraction, $\phi = 0.4$.

Thus, we can now use this expression to determine how the predictions for the domain will look. Combining equations (4.2) and (4.3) and scaling the diffusivity by the free space diffusivity, the expression becomes

$$\frac{D^{eff}}{D^0} = F(\phi) + \frac{1 - F(\phi)}{1 - F(\phi_1)} \cdot \left(\frac{D^{eff}}{D^0} - F(\phi_1) \right). \tag{4.5}$$

In Fig. 4.8, we show these predictions compared to our BD simulation results, when using the expression for $F(\phi)$ in (4.4) and the values for D^{eff}/D^0 when $\phi = 0.4$. There is great agreement between our prediction based on the linear fit and the diffusivity at one volume fraction. This is a great computational advantage, as simulations near close packing are more computationally costly (due to a high number of collisions) and only needs to be done for one volume fraction. Thus, in the limit where $\ell \gg L$, if we know the effective diffusivity for one activity, we can obtain the rest of them by knowing the diffusivity at a single reference point. This reduces the amount of computationally costly simulations while still obtaining an understanding of the behavior.

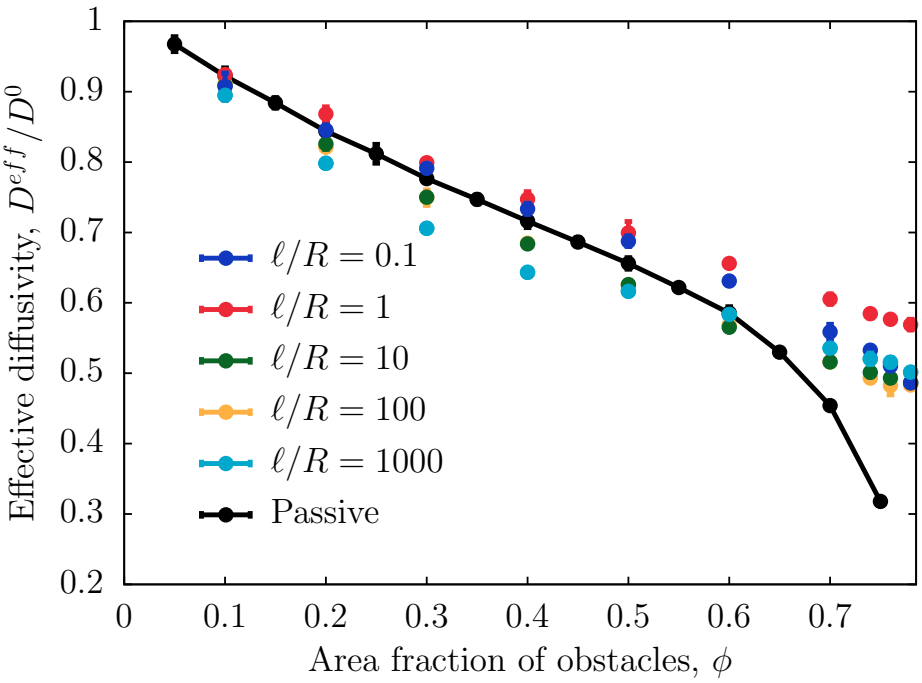

Figure 4.9: The ratio of the effective diffusivity, D^{eff}, to that in free space, $D^0 = U_0^2\tau_R/2$, as a function of the area fraction of obstacles, ϕ. The results are from Brownian dynamics simulation with $D_T = 0$. The diffusivity will only depend on ϕ and the degree of confinement, ℓ/R. (The passive solution is included for comparison.)

No thermal translational diffusivity

In order to understand the influence of the diffusive step size on the hindered diffusion, we investigate the behavior when we have no thermal motion, $D_T = 0$. The particles still undergo reorientation. The number of governing dimensionless groups reduces from three to two, such that the system can be described solely from the degree of confinement, ℓ/R, and the area fraction of obstacles, ϕ.

In Fig. 4.9 we see that the behavior is very similar to what was observed with thermal motion. The effective diffusivity has a non-monotonic dependence on the degree of confinement. For low degrees of confinement, it will resemble the passive hindered diffusion. Furthermore, for intermediate confinement, we see the linear dependence similar to that observed with thermal diffusivity. Fig. 4.10 shows this linear dependence for $\ell/R = 1$, 10, and 100 near close packing. Interestingly, for very high degrees of confinement, we observe a reduction that is less than the observed diffusion when the diffusive step size scales as the obstacle size. When there is no

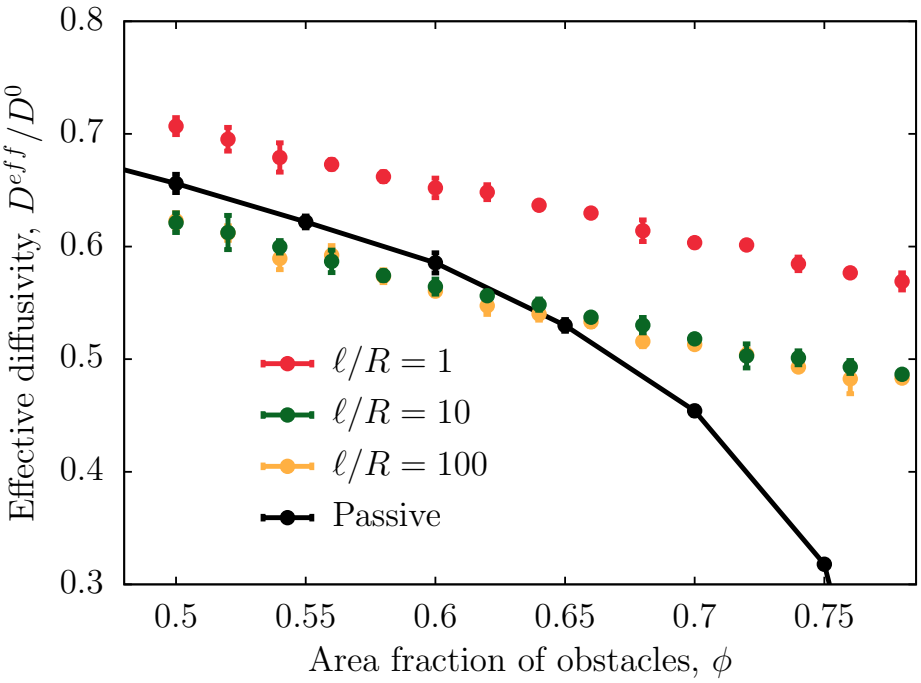

Figure 4.10: The ratio of the effective diffusivity, D^{eff}, to that in free space, D^0, as a function of area fraction of obstacles, ϕ, near close packing. The results are from Brownian dynamics simulation with $D_T = 0$. We observe a larger reduction in effective diffusivity compared to free space for higher degrees of confinement.

thermal diffusion, the particles can slide uninterrupted along the obstacles. Their motion will consist of two parts: moving from one obstacle to the next and sliding along the obstacle surface. If thermal diffusion was present, the particles could deviate from their sliding behavior, translate between obstacles, and be perceived as more trapped. This trapping would lead to a steeper reduction in the diffusivity than when the particles can slide along obstacles without disturbance from thermal noise. Thus, the free sliding explains why the strong confinement is less reduced when $D_T = 0$. The dependence on confinement is also portrayed in Fig. 4.11, where it is apparent that the diffusive behavior changes significantly through the regions of weak, medium, and strong confinement. In the limit of $\ell/R \to 0$, we expect to recover the passive solution for hindered diffusion.

4.4 Conclusions

In this work, we show how diffusivity changes in complex environments such as porous medium. Through Brownian dynamics simulation, we show that the

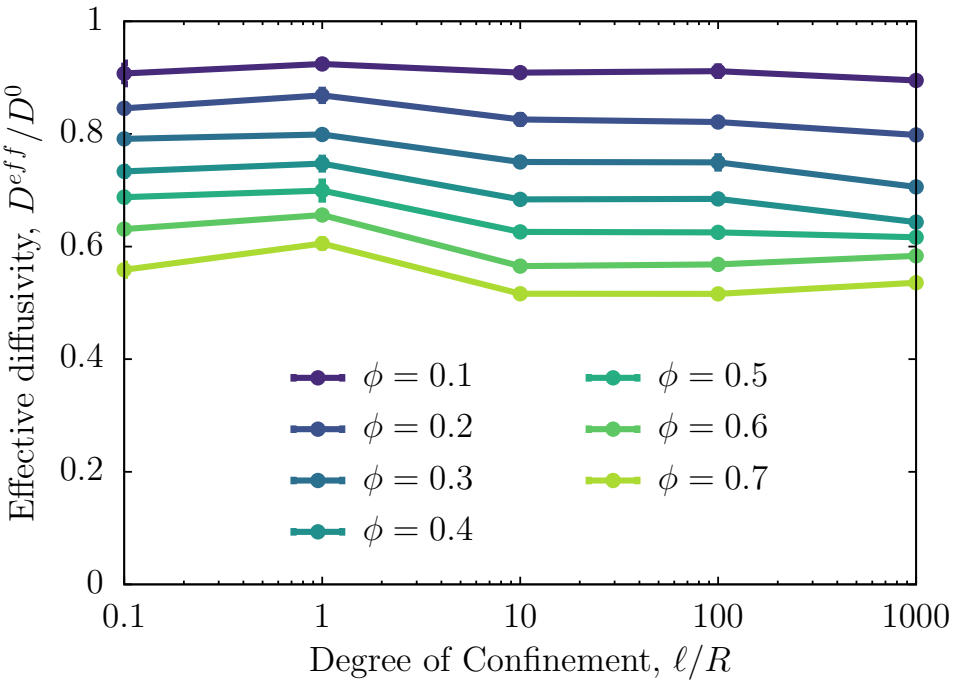

Figure 4.11: The ratio of the effective diffusivity, D^{eff}, to that in free space, D^0, as a function of degree of confinement, ℓ/R. The results are from Brownian dynamics simulation with $D_T = 0$. We observe a non-monotonic change in effective diffusivity with an increasing degree of confinement.

diffusivity of active particles depends not only on the area fraction available for motion but also depends non-trivially on two additional governing groups: the activity and the ratio of run length to obstacle size. We observe non-monotonic changes in effective diffusion with increases in the ratio of particle run length to obstacle size. Three regions of different degrees of confinement explain the behavior; weak, medium, and strong confinement.

Under weak confinement, the active particles in porous media behave similarly to passive particles in porous media, thereby confirming the fundamental rule of active matter that the active energy scale replaces the thermal energy scale, and all trends remain the same as for passive systems. For medium confinement, the diffusion no longer goes towards zero as the area fraction of obstacles approaches the maximum packing fraction. Lastly, for strong confinement, we observe a more substantial reduction in diffusivity compared to passive particles, when obstacle size is comparable to the diffusive step size. In this limit, we present a method for predicting the effective diffusion with fewer computational simulations needed.

Due to these non-trivial diffusion changes, it is increasingly important to know how the active particle run length relates to system size and porosities in porous media. The impact of obstacle size on diffusion will be paramount for designing optimal geometries. Furthermore, it provides a method for tuning effective diffusivity by changing the geometric scales in the system.

4.5 Brownian Dynamics simulations

The Brownian dynamics simulation are based on governing equations of motion: the overdamped Langevin equations [21],

$$\mathbf{0} = -\zeta \boldsymbol{u}_\alpha + \boldsymbol{F}_\alpha^{Swim} + \boldsymbol{F}_\alpha^{B} + \boldsymbol{F}_\alpha^{W}, \tag{4.6}$$

$$\mathbf{0} = -\zeta_R \boldsymbol{\Omega}_\alpha + \boldsymbol{L}_\alpha^{R}, \tag{4.7}$$

where ζ is the translational Stokes drag coefficient, ζ_R is the rotational Stokes drag coefficient, $\boldsymbol{U}_\alpha$ is the translational velocity, $\boldsymbol{\Omega}_\alpha$ is the rotational velocity, and $\boldsymbol{F}_\alpha^{Swim}$ is the swim force defined as $\boldsymbol{F}_\alpha^{Swim} \equiv \zeta U_0 \boldsymbol{q}_\alpha$. $\boldsymbol{F}_\alpha^{B}$ is the random Brownian force with the properties $\overline{\boldsymbol{F}_\alpha^{B}} = \mathbf{0}$ and the $\overline{\boldsymbol{F}_\alpha^{B}(0)\boldsymbol{F}_\alpha^{B}(t)} = 2k_B T\zeta\delta(t)\boldsymbol{I}$, where $\boldsymbol{I}$ is the identity tensor and $\delta(t)$ is the delta-function. $\boldsymbol{L}^R$ is the random reorientation torque, where $\overline{\boldsymbol{L}^R} = \mathbf{0}$ and $\overline{\boldsymbol{L}^R(0)\boldsymbol{L}^R(t)} = 2\zeta_R^2\delta(t)\boldsymbol{I}/\tau_R$. The simulations' length scale is non-dimensionalized by the microscopic length $\delta = \sqrt{D_T/D_R}$, and the time steps are non-dimensionalized by the reorientation time τ_R, where $\tau_R = 1/D_R$ and $D_T = k_B T/\zeta$. It is not necessary to assume that the translational and rotational diffusivity are both thermal, i.e. D_R need not be proportional to $k_B T$. Changes in orientation follow from $d\boldsymbol{q}/dt = \boldsymbol{\Omega}\times\boldsymbol{q}$, with $\boldsymbol{\Omega}$ from the particle angular momentum balance (4.7).

References

[1] C. Bechinger, R. Di Leonardo, H. Löwen, C. Reichhardt, G. Volpe, and G. Volpe, "Active particles in complex and crowded environments", Reviews of Modern Physics **88**, 045006 (2016).

[2] A. Ghosh, W. Xu, N. Gupta, and D. H. Gracias, "Active matter therapeutics", Nano Today **31**, 100836 (2020).

[3] W. Gao, R. Dong, S. Thamphiwatana, J. Li, W. Gao, L. Zhang, and J. Wang, "Artificial micromotors in the mouse's stomach: a step toward in vivo use of...", ACS nano **9**, 117–123 (2014).

[4] W. Yan and J. F. Brady, "The force on a boundary in active matter", Journal of Fluid Mechanics **785**, R1 (2015).

[5] S. C. Takatori, R. De Dier, J. Vermant, and J. F. Brady, "Acoustic trapping of active matter", Nature Communications **7**, 10694 (2016).

[6] P. S. Burada, P. Hänggi, F. Marchesoni, G. Schmid, and P. Talkner, "Diffusion in confined geometries", ChemPhysChem **10**, 45–54 (2009).

[7] P. Malgaretti, I. Pagonabarraga, and J. M. Rubi, "Entropic transport in confined media: A challenge for computational studies in biological and soft-matter systems", Frontiers in Physics **1**, 1–9 (2013).

[8] M. Mangeat, T. Guérin, and D. S. Dean, "Effective diffusivity of Brownian particles in a two dimensional square lattice of hard disks", Journal of Chemical Physics **152**, 10.1063/5.0009095 (2020).

[9] R. Alonso-Matilla, B. Chakrabarti, and D. Saintillan, "Transport and dispersion of active particles in periodic porous media", Physical Review Fluids **4**, 1–21 (2019).

[10] M. Brun-Cosme-Bruny, E. Bertin, B. Coasne, P. Peyla, and S. Rafaï, "Effective diffusivity of microswimmers in a crowded environment", Journal of Chemical Physics **150**, 104901 (2019).

[11] D. A. Beard and T. Schlick, "Unbiased rotational moves for rigid-body dynamics", Biophysical Journal **85**, 2973–2976 (2003).

[12] W. M. Lai, D. Rubin, and E. Krempl, *Introduction to Continuum Mechanics, Revised Edition* (Pergamon, 1978), p. 324.

[13] B. Ezhilan, R. Alonso-Matilla, and D. Saintillan, "On the distribution and swim pressure of run-and-tumble particles in confinement", Journal of Fluid Mechanics **781**, R4 (2015).

[14] X. Yang, L. Manning, and C. Marchetti, "Aggregation and segregation of confined active particles", Soft Matter **10**, 6477–6484 (2014).

[15] C. M. Kjeldbjerg and J. F. Brady, "Partitioning of active particles into porous media", *In preparation* (2021).

[16] Sujit S. Datta, “Confinement and activity regulate bacterial motion in porous media”, Soft Matter **64**, 6545–6563 (2019).

[17] C. M. Kjeldbjerg and J. F. Brady, “Theory for the casimir effect and the partitioning of active matter”, Soft Matter **17**, DOI: 10.1039/d0sm01797c, 523–530 (2021),

[18] D. M. Heyes and J. R. Melrose, “Brownian dynamics simulations of model hard-sphere suspensions”, Journal of Non-Newtonian Fluid Mechanics **46**, 1–28 (1993).

[19] W. Schaertl and H. Sillescu, “Brownian dynamics simulations of colloidal hard spheres. Effects of sample dimensionality on self-diffusion”, Journal of Statistical Physics **74**, 687–703 (1994).

[20] D. R. Foss and J. F. Brady, “Brownian dynamics simulation of hard-sphere colloidal dispersions”, Journal of Rheology **44**, 629–651 (2000).

[21] W. Yan and J. F. Brady, “The swim force as a body force”, Soft Matter **11**, 6235–6244 (2015).

Appendix A

THE MOMENTS METHOD: REVIEW OF ISOTROPIC Q ASSUMPTION

2D: One infinitely long wall

To understand the impact of our assumption that the nematic order is isotropic that we investigate comparisons of the numerical solution to the full Smoluchowski equation and analytical solutions from the moments' expansion of the Smoluchowski equation. The one-dimensional solution to the Smoluchowski near a wall in an active bath is independent of closure. The concentration at the wall is given by

$$n^{wall} = 1 + \frac{1}{2}\left(\frac{\ell}{\delta}\right)^2 = 1 + \frac{k_s T_s}{k_B T}, \tag{A.1}$$

where ell is the run length, δ is the diffusive step size, and $k_s T_s$ is a measure of the activity analogous to the thermal energy $k_B T$. We can compare this to our numerical solution of the Smoluchowski equation, we obtain from expanding into the weak form and implementing into *FREEFEM++*. As expected, we get the same from the numerical solution and the analytical one as is shown in Fig. A.1.

2D: Infinitely long parallel walls

The expression for the concentration between two parallel walls in 2D assuming the nematic order field is isotropic ($\boldsymbol{Q} = 0$) is

$$\frac{n(z)}{n^0} = 1 + \frac{1}{2}\left(\frac{\ell}{\delta}\right)^2 \frac{\sinh(\lambda z) + \sinh(\lambda(H - z))}{\sinh(\lambda H)}, \tag{A.2}$$

where $\lambda = \sqrt{1 + \frac{1}{2}\left(\frac{\ell}{\delta}\right)^2}/\delta$ and H is the separation distance. In the limit of large λH, corresponding to when $\delta \ll \ell$ and $\delta \ll H$, n^0 is the center concentration between the two parallel walls. This is also illustrated in A, where the dark blue color shows when n^0 is equal to the center concentration, such that $n^0 = n(H/2)$.

Thus, from figure A.2, we can assume that for $\ell/\delta > 6$ and a degree of confinement between 0 and 3, n^0 is the center concentration. Thereby, we can now investigate how the assumption of isotropic nematic order deviates from the numerical solution to the full Smoluchowski equation when having confinement.

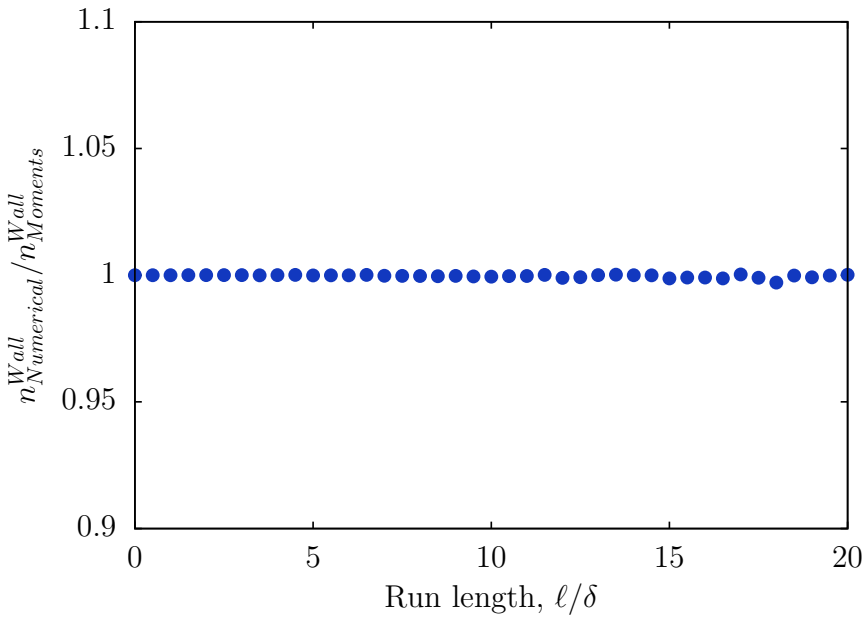

Figure A.1: The wall concentration from finite element solutions of the full Smoluchowski equation compared to the moments' solution assuming $\boldsymbol{Q} = 0$.

The polar order of a system is the highest close to the walls, and therefore it is interesting to investigate how the nematic order assumption affects the wall concentration. The concentration at the wall for the full Smoluchowski equation solved using finite element methods compared to the solution of the moments' expansion when assuming isotropic nematic order is shown in Fig. A.3. For small degrees of confinement, the moment solution predicts the concentration at the wall well. As the degree of confinement increases, the wall concentration from the numerical solution is lower and the moments' expansion no longer captures the behavior accurately.

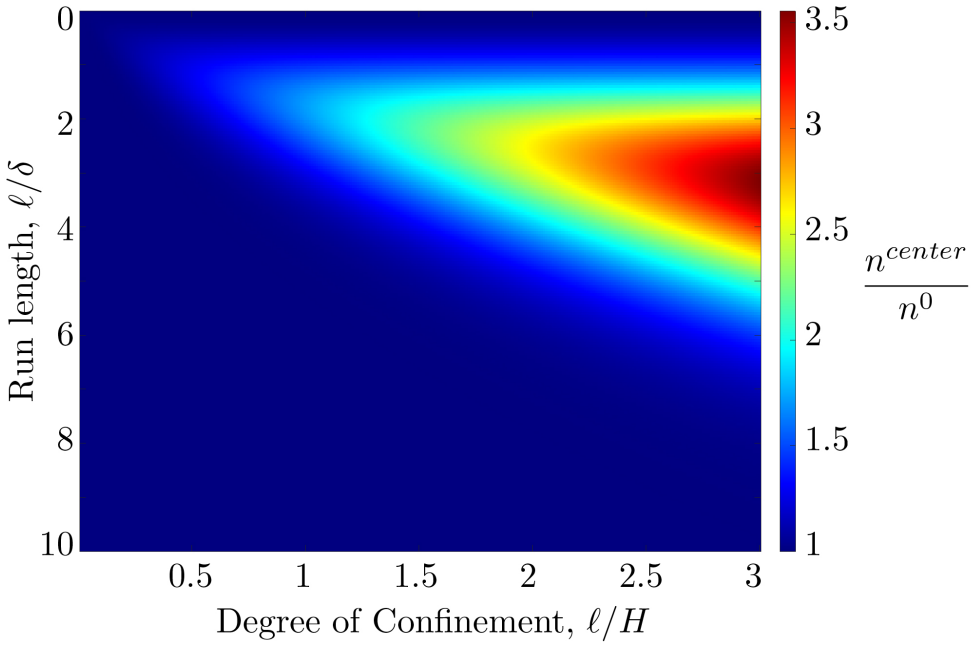

Figure A.2: The value of $n(H/2)/n^0$ as a function of run length and degree of confinement for infinitely long parallel plates. When activity is high, n^0 represents the center concentration such that $n(H/2)/n^0 = 1$. Further, for $\ell/\delta < 6$ and confinement, this is not the case.

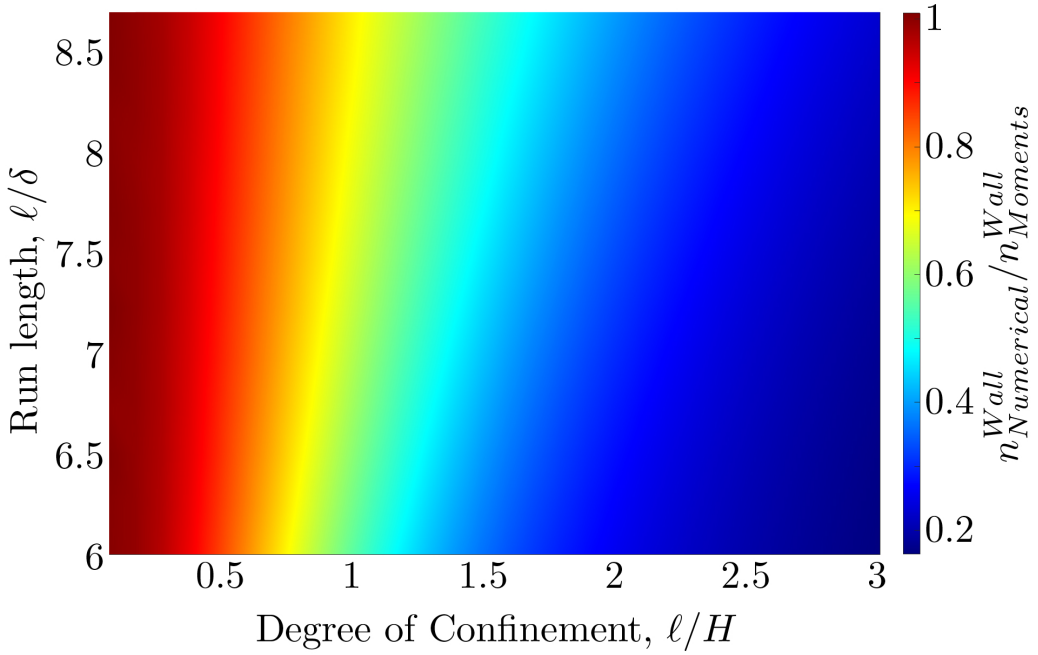

Figure A.3: The wall concentration from finite element solutions of the full Smoluchowski equation compared to the moments' solution of the Smoluchowski equation assuming $\boldsymbol{Q} = 0$.

Appendix B

FINITE ELEMENT CALCULATIONS: THE WEAK FORM

Problem definition

Moments equations:

$$\frac{\mathrm{d}n}{\mathrm{d}t} + \nabla \cdot \boldsymbol{j}_n = 0, \quad \text{where} \quad \boldsymbol{j}_n = U_0 \boldsymbol{m} - D_T \nabla n, \tag{B.1}$$

$$\frac{\mathrm{d}\boldsymbol{m}}{\mathrm{d}t} + \nabla \cdot \boldsymbol{j}_m + (d-1) D_R \boldsymbol{m} = 0, \quad \text{where} \quad \boldsymbol{j}_m = U_0 \boldsymbol{Q} - D_T \nabla \boldsymbol{m}. \tag{B.2}$$

Thereby, in two dimensions:

$$\frac{\mathrm{d}n}{\mathrm{d}t} + \nabla \cdot [U_0 \boldsymbol{m} - D_T \nabla n] = 0, \tag{B.3}$$

$$\frac{\mathrm{d}\boldsymbol{m}}{\mathrm{d}t} + \nabla \cdot [U_0 \boldsymbol{Q} - D_T \nabla \boldsymbol{m}] + D_R \boldsymbol{m} = 0. \tag{B.4}$$

Q closure

Applying the Q closure in two dimensions: $\boldsymbol{Q} = n\boldsymbol{I}/2$ and the equation becomes

$$\frac{\mathrm{d}n}{\mathrm{d}t} + \nabla \cdot [U_0 \boldsymbol{m} - D_T \nabla n] = 0, \tag{B.5}$$

$$\frac{\mathrm{d}\boldsymbol{m}}{\mathrm{d}t} + \nabla \cdot [U_0 n\boldsymbol{I}/2 - D_T \nabla \boldsymbol{m}] + D_R \boldsymbol{m} = 0. \tag{B.6}$$

We can rewrite these into

$$\frac{\mathrm{d}n}{\mathrm{d}t} + U_0 \nabla \cdot \boldsymbol{m} - D_T \nabla^2 n = 0, \tag{B.7}$$

$$\frac{\mathrm{d}\boldsymbol{m}}{\mathrm{d}t} + \frac{U_0}{2} \nabla n - D_T \nabla^2 \boldsymbol{m} + D_R \boldsymbol{m} = 0. \tag{B.8}$$

Applying the scaling $t \approx \tau_R$ and $x, y \approx \delta$, the n-equation becomes

$$\frac{1}{\tau_R} \frac{\mathrm{d}n}{\mathrm{d}t} + \frac{U_0}{\delta} \nabla \cdot \boldsymbol{m} - \frac{D_T}{\delta^2} \nabla^2 n = 0. \tag{B.9}$$

Using that $U_0 \tau_R = \ell$ and $\delta = \sqrt{D_T / D_R}$, we get

$$\frac{\mathrm{d}n}{\mathrm{d}t} + \left(\frac{\ell}{\delta} \right) \nabla \cdot \boldsymbol{m} - \nabla^2 n = 0. \tag{B.10}$$

Applying the scaling $t \sim \tau_R$ and $x, y \sim \delta$, the m-equations become

$$\frac{1}{\tau_R}\frac{\mathrm{d}\boldsymbol{m}}{\mathrm{d}t} + \frac{U_0}{2\delta}\nabla n - \frac{D_T}{\delta^2}\nabla^2\boldsymbol{m} + D_R\boldsymbol{m} = 0. \tag{B.11}$$

Using that $U_0\tau_R = \ell$, $D_R = 1/\tau_R$ and $\delta = \sqrt{D_T/D_R}$, we get

$$\frac{\mathrm{d}\boldsymbol{m}}{\mathrm{d}t} + \frac{1}{2}\left(\frac{\ell}{\delta}\right)\nabla n - \nabla^2\boldsymbol{m} + \boldsymbol{m} = 0. \tag{B.12}$$

Equations (B.10) and (B.12) become the three equations for the system

$$\frac{\mathrm{d}n}{\mathrm{d}t} + \left(\frac{\ell}{\delta}\right)\left(\frac{\mathrm{d}m_x}{\mathrm{d}x} + \frac{\mathrm{d}m_x}{\mathrm{d}y}\right) - \left(\frac{\mathrm{d}^2n}{\mathrm{d}x^2} + \frac{\mathrm{d}^2n}{\mathrm{d}y^2}\right) = 0, \tag{B.13}$$

$$\frac{\mathrm{d}m_x}{\mathrm{d}t} + \frac{1}{2}\left(\frac{\ell}{\delta}\right)\frac{\mathrm{d}n}{\mathrm{d}x} + m_x - \left(\frac{\mathrm{d}^2m_x}{\mathrm{d}x^2} + \frac{\mathrm{d}^2m_x}{\mathrm{d}y^2}\right) = 0. \tag{B.14}$$

$$\frac{\mathrm{d}m_y}{\mathrm{d}t} + \frac{1}{2}\left(\frac{\ell}{\delta}\right)\frac{\mathrm{d}n}{\mathrm{d}y} + m_y - \left(\frac{\mathrm{d}^2m_y}{\mathrm{d}x^2} + \frac{\mathrm{d}^2m_y}{\mathrm{d}y^2}\right) = 0. \tag{B.15}$$

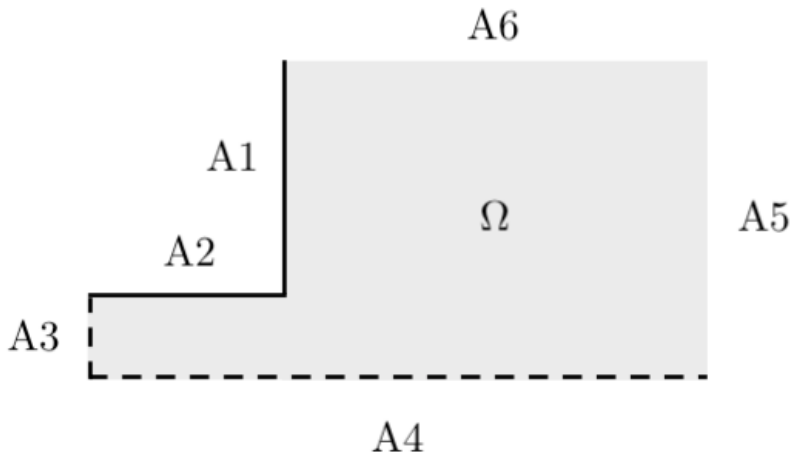

Figure B.1: System geometry with boundary labels. Solid lines are hard walls and dashed lines are boundaries where symmetry applies.

Boundary condition on A1-wall

At the wall, we apply the no flux in n

$$n_x \cdot j_n = 0 \tag{B.16}$$

$$n_x \cdot [U_0\boldsymbol{m} - D_T\nabla n] = 0 \tag{B.17}$$

$$U_0 m_x - D_T\frac{\mathrm{d}n}{\mathrm{d}x} = 0. \tag{B.18}$$

Applying scaling to boundary conditions

$$U_0 m_x - D_T/\delta \frac{\mathrm{d}n}{\mathrm{d}x} = 0 \tag{B.19}$$

$$\Rightarrow U_0/D_R m_x - (D_T/D_R)/\delta \frac{\mathrm{d}n}{\mathrm{d}x} = 0 \tag{B.20}$$

$$\Rightarrow \frac{\mathrm{d}n}{\mathrm{d}x} = \left(\frac{\ell}{\delta}\right) m_x. \tag{B.21}$$

Further, at the wall we apply the no flux in m_x

$$n_x \cdot j_m = 0 \tag{B.22}$$

$$n_x \cdot [U_0 n \boldsymbol{I}/2 - D_T \nabla \boldsymbol{m}] = 0 \tag{B.23}$$

$$1/2 U_0 n - D_T \frac{\mathrm{d}m_x}{\mathrm{d}x} = 0 \tag{B.24}$$

$$\sim \frac{\mathrm{d}m_x}{\mathrm{d}x} = \frac{1}{2}\left(\frac{\ell}{\delta}\right) n \tag{B.25}$$

From the full equation P, we get

$$j_x^T = 0 \Rightarrow U_0 q_x P - D_T \frac{\mathrm{d}P}{\mathrm{d}x} \tag{B.26}$$

$$\Rightarrow j_{xy}^m = -D_T \frac{\mathrm{d}m_y}{\mathrm{d}x} = 0 \tag{B.27}$$

$$\frac{\mathrm{d}m_y}{\mathrm{d}x} = 0. \tag{B.28}$$

In summary

$$\frac{\mathrm{d}n}{\mathrm{d}x} = \left(\frac{\ell}{\delta}\right) m_x, \tag{B.29}$$

$$\frac{\mathrm{d}m_x}{\mathrm{d}x} = \frac{1}{2}\left(\frac{\ell}{\delta}\right) n, \tag{B.30}$$

$$\frac{\mathrm{d}m_y}{\mathrm{d}x} = 0. \tag{B.31}$$

Boundary condition on A2

No translational flux of P in the y-direction:

$$J_y^T = U_0 q_y P - D_T \frac{\mathrm{d}P}{\mathrm{d}y} = 0. \tag{B.32}$$

Thereby, we can get the condition on n multiplying equation (B.32) by q_y

$$J_y^n = U_0 q_y q_y P - D_T \frac{\mathrm{d}q_y P}{\mathrm{d}y} = 0, \tag{B.33}$$

$$\Rightarrow U_0 m_y - D_T \frac{\mathrm{d}n}{\mathrm{d}y} = 0. \tag{B.34}$$

With the correct scaling, the condition becomes

$$\frac{\mathrm{d}n}{\mathrm{d}y} = \left(\frac{\ell}{\delta}\right) m_y. \tag{B.35}$$

For the condition on m_y, we multiply equation (B.32) by $q_y q_y$ and get

$$J_{yy}^n = U_0 q_y q_y q_y P - D_T \frac{\mathrm{d}q_y q_y P}{\mathrm{d}y} = 0, \tag{B.36}$$

$$\Rightarrow U_0 \left(\frac{1}{2} n + Q_{yy}\right) - D_T \frac{\mathrm{d}m_y}{\mathrm{d}y} = 0. \tag{B.37}$$

With the correct scaling and $\boldsymbol{Q}$ closure, the expression becomes

$$\frac{\mathrm{d}m_y}{\mathrm{d}y} = \frac{1}{2}\left(\frac{\ell}{\delta}\right) n. \tag{B.38}$$

For the condition on m_y we multiply eq. (B.32) by $q_y q_x$ and get

$$J_{yy}^n = U_0 q_y q_y q_x P - D_T \frac{\mathrm{d}q_y q_x P}{\mathrm{d}y} = 0, \tag{B.39}$$

$$\Rightarrow U_0 \left(Q_{yx}\right) - D_T \frac{\mathrm{d}m_x}{\mathrm{d}y} = 0, \tag{B.40}$$

with the correct scaling and Q closure the expression becomes

$$\frac{\mathrm{d}m_x}{\mathrm{d}y} = 0. \tag{B.41}$$

Boundary condition on A3

Symmetry in P: $\mathrm{d}P/\mathrm{d}x$=0 and thereby

$$\frac{\mathrm{d}n}{\mathrm{d}x} = 0, \tag{B.42}$$

$$\frac{\mathrm{d}m_x}{\mathrm{d}x} = 0, \tag{B.43}$$

$$\frac{\mathrm{d}m_y}{\mathrm{d}x} = 0. \tag{B.44}$$

Boundary condition on A4

Symmetry in P across the boundary: $\mathrm{d}P/\mathrm{d}y=0$ and thereby

$$\frac{\mathrm{d}n}{\mathrm{d}y} = 0, \tag{B.45}$$

$$\frac{\mathrm{d}m_x}{\mathrm{d}y} = 0, \tag{B.46}$$

$$\frac{\mathrm{d}m_y}{\mathrm{d}y} = 0. \tag{B.47}$$

Boundary condition on A5

P is constant at this boundary, and thereby

$$n \sim n^{\infty} \sim 1, \tag{B.48}$$

$$m_x = 0, \tag{B.49}$$

$$m_y = 0. \tag{B.50}$$

Boundary condition on A6

P (and thereby n) is a function of distance from the wall, and from the force on a boundary paper we have

$$n = n^{\infty}\left(1 + \frac{1}{2}\left(\frac{\ell}{\delta}\right)^2 \exp\left(-\lambda x\right)\right), \tag{B.51}$$

$$\lambda = \sqrt{1 + \frac{1}{2}\left(\frac{\ell}{\delta}\right)^2}/\delta. \tag{B.52}$$

The polar order screening is

$$m_x = -\frac{n^{\infty}}{2}\left(\lambda\ell\right)\exp\left(-\lambda x\right), \tag{B.53}$$

$$m_y = 0. \tag{B.54}$$

In summary, the scaled equations become

$$n = 1 + \frac{1}{2}\left(\frac{\ell}{\delta}\right)^2 \exp\left(-\lambda x\right), \tag{B.55}$$

$$m_x = -\frac{n^\infty}{2}\left(\lambda\ell\right)\exp\left(-\lambda x\right), \tag{B.56}$$

$$m_y = 0, \tag{B.57}$$

$$\lambda = \sqrt{1 + \frac{1}{2}\left(\frac{\ell}{\delta}\right)^2}/\delta. \tag{B.58}$$

The weak form of the equations

We define that $n = u_1, m_x = u_2$, and $my = u_3$. Further, we define a test-function for the n-equation, $v1$, multiply the equation by v_1, and integrate over the domain Ω

$$\int_\Omega v_1 \frac{\mathrm{d}u_1}{\mathrm{d}t} + v_1\left(\frac{\ell}{\delta}\right)\frac{\mathrm{d}u_2}{\mathrm{d}x} + v_1\left(\frac{\ell}{\delta}\right)\frac{\mathrm{d}u_2}{\mathrm{d}y} - v_1\frac{\mathrm{d}^2u_1}{\mathrm{d}x^2} - v_1\frac{\mathrm{d}^2u_1}{\mathrm{d}y^2}\,\mathrm{d}\Omega = 0. \tag{B.59}$$

The equation is simplified via integration by parts

$$\int_\Omega v_1\frac{\mathrm{d}^2u_1}{\mathrm{d}x^2}\,\mathrm{d}\Omega = \int_{A5}\frac{\mathrm{d}u_1}{\mathrm{d}x}v_1\,\mathrm{d}S - \int_{A1}\frac{\mathrm{d}u_1}{\mathrm{d}x}v_1\,\mathrm{d}S - \int_{A3}\frac{\mathrm{d}u_1}{\mathrm{d}x}v_1\,\mathrm{d}S - \int_\Omega \frac{\mathrm{d}u_1}{\mathrm{d}x}\frac{\mathrm{d}v_1}{\mathrm{d}x}\,\mathrm{d}\Omega \tag{B.60}$$

$$= -\int_{A1}\frac{\mathrm{d}u_1}{\mathrm{d}x}v_1\,\mathrm{d}S - \int_\Omega \frac{\mathrm{d}u_1}{\mathrm{d}x}\frac{\mathrm{d}v_1}{\mathrm{d}x}\,\mathrm{d}\Omega \tag{B.61}$$

$$= -\int_\Omega \frac{\mathrm{d}u_1}{\mathrm{d}x}\frac{\mathrm{d}v_1}{\mathrm{d}x}\,\mathrm{d}\Omega - \int_{A1}\left(\frac{\ell}{\delta}\right)u_2\,v_1\,\mathrm{d}S \tag{B.62}$$

$$\int_\Omega v_1\frac{\mathrm{d}^2u_1}{\mathrm{d}y^2}\,\mathrm{d}\Omega = \int_{A6}\frac{\mathrm{d}u_1}{\mathrm{d}y}v_1\,\mathrm{d}S + \int_{A2}\frac{\mathrm{d}u_1}{\mathrm{d}y}v_1\,\mathrm{d}S - \int_{A4}\frac{\mathrm{d}u_1}{\mathrm{d}y}v_1\,\mathrm{d}S - \int_\Omega \frac{\mathrm{d}u_1}{\mathrm{d}y}\frac{\mathrm{d}v_1}{\mathrm{d}y}\,\mathrm{d}\Omega \tag{B.63}$$

$$= -\int_\Omega \frac{\mathrm{d}u_1}{\mathrm{d}y}\frac{\mathrm{d}v_1}{\mathrm{d}y}\,\mathrm{d}\Omega + \int_{A2}\left(\frac{\ell}{\delta}\right)u_3v_1\,\mathrm{d}S. \tag{B.64}$$

Equation (B.59) becomes

$$\int_\Omega v_1\frac{\mathrm{d}u_1}{\mathrm{d}t} + v_1\left(\frac{\ell}{\delta}\right)\frac{\mathrm{d}u_2}{\mathrm{d}x} + v_1\left(\frac{\ell}{\delta}\right)\frac{\mathrm{d}u_2}{\mathrm{d}y} + \frac{\mathrm{d}u_1}{\mathrm{d}x}\frac{\mathrm{d}v_1}{\mathrm{d}x} + \frac{\mathrm{d}u_1}{\mathrm{d}y}\frac{\mathrm{d}v_1}{\mathrm{d}y}\,\mathrm{d}\Omega \tag{B.65}$$

$$+ \int_{A1}\left(\frac{\ell}{\delta}\right)u_2\,v_1\,\mathrm{d}S - \int_{A2}\left(\frac{\ell}{\delta}\right)u_3v_1\,\mathrm{d}S = 0. \tag{B.66}$$

We define the test-function for the m_x-equation, v_2.

$$\int_\Omega v_2\frac{\mathrm{d}u_2}{\mathrm{d}t} + \frac{1}{2}\left(\frac{\ell}{\delta}\right)v_2\frac{\mathrm{d}u_1}{\mathrm{d}x} + v_2u_2 - v_2\frac{\mathrm{d}^2u_2}{\mathrm{d}x^2} - v_2\frac{\mathrm{d}^2u_2}{\mathrm{d}y^2}\,\mathrm{d}\Omega = 0. \tag{B.67}$$

The equation is simplified via integration by parts

$$\int_\Omega v_2 \frac{\mathrm{d}^2 u_2}{\mathrm{d}x^2}\,\mathrm{d}\Omega = \int_{A5} \frac{\mathrm{d}u_2}{\mathrm{d}x} v_2\,\mathrm{d}S - \int_{A1} \frac{\mathrm{d}u_2}{\mathrm{d}x} v_2\,\mathrm{d}S - \int_{A3} \frac{\mathrm{d}u_2}{\mathrm{d}x} v_2\,\mathrm{d}S - \int_\Omega \frac{\mathrm{d}u_2}{\mathrm{d}x}\frac{\mathrm{d}v_2}{\mathrm{d}x}\,\mathrm{d}\Omega \tag{B.68}$$

$$= -\int_{A1} \frac{1}{2}\left(\frac{\ell}{\delta}\right) u_1\, v_2\,\mathrm{d}S - \int_\Omega \frac{\mathrm{d}u_2}{\mathrm{d}x}\frac{\mathrm{d}v_2}{\mathrm{d}x}\,\mathrm{d}\Omega \tag{B.69}$$

$$\int_\Omega v_2 \frac{\mathrm{d}^2 u_2}{\mathrm{d}y^2}\,\mathrm{d}\Omega = \int_{A6} \frac{\mathrm{d}u_2}{\mathrm{d}y} v_2\,\mathrm{d}S + \int_{A2} \frac{\mathrm{d}u_2}{\mathrm{d}y} v_2\,\mathrm{d}S - \int_{A4} \frac{\mathrm{d}u_2}{\mathrm{d}y} v_2\,\mathrm{d}S - \int_\Omega \frac{\mathrm{d}u_2}{\mathrm{d}y}\frac{\mathrm{d}v_2}{\mathrm{d}y}\,\mathrm{d}\Omega \tag{B.70}$$

$$= -\int_\Omega \frac{\mathrm{d}u_2}{\mathrm{d}y}\frac{\mathrm{d}v_2}{\mathrm{d}y}\,\mathrm{d}\Omega. \tag{B.71}$$

Equation (B.67) becomes

$$\int_\Omega v_2 \frac{\mathrm{d}u_2}{\mathrm{d}t} + \frac{1}{2}\left(\frac{\ell}{\delta}\right) v_2 \frac{\mathrm{d}u_1}{\mathrm{d}x} + v_2 u_2 + \frac{\mathrm{d}u_2}{\mathrm{d}x}\frac{\mathrm{d}v_2}{\mathrm{d}x} + \frac{\mathrm{d}u_2}{\mathrm{d}y}\frac{\mathrm{d}v_2}{\mathrm{d}y}\,\mathrm{d}\Omega + \int_{A1} \frac{1}{2}\left(\frac{\ell}{\delta}\right) u_1 v_2\,\mathrm{d}S = 0. \tag{B.72}$$

We define the test-function for the m_x-equation, v_3.

$$\int_\Omega v_3 \frac{\mathrm{d}u_3}{\mathrm{d}t} + \frac{1}{2}\left(\frac{\ell}{\delta}\right)\frac{\mathrm{d}u_1}{\mathrm{d}y} + v_3 u_3 - v_3 \frac{\mathrm{d}^2 u_3}{\mathrm{d}x^2} - v_3 \frac{\mathrm{d}^2 u_3}{\mathrm{d}y^2}\,\mathrm{d}S = 0. \tag{B.73}$$

The equation is simplified via integration by parts

$$\int_\Omega v_3 \frac{\mathrm{d}^2 u_3}{\mathrm{d}x^2}\,\mathrm{d}\Omega = \int_{A5} \frac{\mathrm{d}u_3}{\mathrm{d}x} v_3\,\mathrm{d}S - \int_{A1} \frac{\mathrm{d}u_3}{\mathrm{d}x} v_3\,\mathrm{d}S - \int_{A3} \frac{\mathrm{d}u_3}{\mathrm{d}x} v_3\,\mathrm{d}S - \int_\Omega \frac{\mathrm{d}u_3}{\mathrm{d}x}\frac{\mathrm{d}v_3}{\mathrm{d}x}\,\mathrm{d}\Omega \tag{B.74}$$

$$= -\int_\Omega \frac{\mathrm{d}u_3}{\mathrm{d}x}\frac{\mathrm{d}v_3}{\mathrm{d}x}\,\mathrm{d}\Omega \tag{B.75}$$

$$\int_\Omega v_3 \frac{\mathrm{d}^2 u_3}{\mathrm{d}y^2}\,\mathrm{d}\Omega = \int_{A6} \frac{\mathrm{d}u_3}{\mathrm{d}y} v_3\,\mathrm{d}S + \int_{A2} \frac{\mathrm{d}u_3}{\mathrm{d}y} v_3\,\mathrm{d}S - \int_{A4} \frac{\mathrm{d}u_3}{\mathrm{d}y} v_3\,\mathrm{d}S - \int_\Omega \frac{\mathrm{d}u_3}{\mathrm{d}y}\frac{\mathrm{d}v_3}{\mathrm{d}y}\,\mathrm{d}\Omega \tag{B.76}$$

$$= -\int_\Omega \frac{\mathrm{d}u_3}{\mathrm{d}y}\frac{\mathrm{d}v_3}{\mathrm{d}y}\,\mathrm{d}\Omega + \int_{A2} \frac{1}{2}\left(\frac{\ell}{\delta}\right) u_1 v_3\,\mathrm{d}S. \tag{B.77}$$

Equation (B.73) becomes

$$\int_\Omega v_3 \frac{\mathrm{d}u_3}{\mathrm{d}t} + \frac{1}{2}\left(\frac{\ell}{\delta}\right)\frac{\mathrm{d}u_1}{\mathrm{d}y} + v_3 u_3 + \frac{\mathrm{d}u_3}{\mathrm{d}x}\frac{\mathrm{d}v_3}{\mathrm{d}x} + v_3 \frac{\mathrm{d}^2 u_3}{\mathrm{d}y^2}\,\mathrm{d}\Omega - \int_{A2} \frac{1}{2}\left(\frac{\ell}{\delta}\right) u_1 v_3\,\mathrm{d}S = 0. \tag{B.78}$$

Steady state weak form FEM setup

For the finite element method, we look at steady state, and the coupled weak form equations become

$$\int_\Omega v_1 \left(\frac{\ell}{\delta}\right) \frac{\mathrm{d}u_2}{\mathrm{d}x} + v_1 \left(\frac{\ell}{\delta}\right) \frac{\mathrm{d}u_2}{\mathrm{d}y} + \frac{\mathrm{d}u_1}{\mathrm{d}x}\frac{\mathrm{d}v_1}{\mathrm{d}x} + \frac{\mathrm{d}u_1}{\mathrm{d}y}\frac{\mathrm{d}v_1}{\mathrm{d}y}\,\mathrm{d}\Omega$$
$$+ \int_{A1} \left(\frac{\ell}{\delta}\right) u_2\, v_1\,\mathrm{d}S - \int_{A2} \left(\frac{\ell}{\delta}\right) u_3 v_1\,\mathrm{d}S = 0,$$
$$\int_\Omega \frac{1}{2}\left(\frac{\ell}{\delta}\right) v_2 \frac{\mathrm{d}u_1}{\mathrm{d}x} + v_2 u_2 + \frac{\mathrm{d}u_2}{\mathrm{d}x}\frac{\mathrm{d}v_2}{\mathrm{d}x} + \frac{\mathrm{d}u_2}{\mathrm{d}y}\frac{\mathrm{d}v_2}{\mathrm{d}y}\,\mathrm{d}\Omega + \int_{A1} \frac{1}{2}\left(\frac{\ell}{\delta}\right) u_1 v_2\,\mathrm{d}S = 0,$$
$$\int_\Omega \frac{1}{2}\left(\frac{\ell}{\delta}\right) \frac{\mathrm{d}u_1}{\mathrm{d}y} + v_3 u_3 + \frac{\mathrm{d}u_3}{\mathrm{d}x}\frac{\mathrm{d}v_3}{\mathrm{d}x} + v_3 \frac{\mathrm{d}^2 u_3}{\mathrm{d}y^2}\,\mathrm{d}\Omega - \int_{A2} \frac{1}{2}\left(\frac{\ell}{\delta}\right) u_1 v_3\,\mathrm{d}S = 0.$$

BCs on A5

$$u_1 \sim 1, \tag{B.79}$$
$$u_2 = 0, \tag{B.80}$$
$$u_3 = 0. \tag{B.81}$$

BCs on A6

$$u_1 = 1 + \frac{1}{2}\left(\frac{\ell}{\delta}\right)^2 \exp\left(-\lambda x\right), \tag{B.82}$$
$$u_2 = -\frac{n^\infty}{2}\left(\lambda \ell\right) \exp\left(-\lambda x\right), \tag{B.83}$$
$$u_3 = 0, \tag{B.84}$$
$$\lambda = \sqrt{1 + \frac{1}{2}\left(\frac{\ell}{\delta}\right)^2}/\delta. \tag{B.85}$$

Note that this problem is not standard to solve with *FREEFEM++* as it is solved on a three-dimensional mesh with multiple mesh refinements. Therefore, it quickly becomes very computationally costly, requiring a large amount of memory.